

# Progress and Perspective of Controlling Li Dendrites Growth in All-Solid-State Li Metal Batteries via External Physical Fields

Jianhua Yao, Guoxi Zhu, Kang Dong, Markus Osenberg, André Hilger, Henning Markötter, Jiangwei Ju, Fu Sun,\* Ingo Manke, and Guanglei Cui\*

Li dendrites penetration through solid electrolytes (SEs) challenges the development of solid-state Li batteries (SSLBs). To date, significant efforts are devoted to understand the mechanistic dynamics of Li dendrites nucleation, growth, and propagation in SEs, and various strategies that aim to alleviate and even inhibit Li dendrite formation have been proposed. Nevertheless, most of these conventional strategies require either additional material processing steps or new materials/layers that eventually increase battery cost and complexity. In contrast, using external fields, such as mechanical force, temperature physical field, electric field, pulse current, and even magnetic field to regulate Li dendrites penetration through SEs, seems to be one of the most cost-effective strategies. This review focuses on the current research progress of utilizing external physical fields in regulating Li dendrites growth in SSLBs. For this purpose, the mechanical properties of Li and SEs, as well as the experimental results that visually track Li penetration dynamics, are reviewed. Finally, the review ends with remaining open questions in future studies of Li dendrites growth and penetration in SEs. It is hoped this review can shed some light on understanding the complex Li dendrite issues in SSLBs and potentially guide their rational design for further development.


components, is at the forefront of developing next-generation batteries with enhanced energy density and safety property.<sup>[1–4]</sup> However, the recent and fast research worldwide has led to a much clearer understanding that tremendous challenges exist in successfully developing SSLBs, even though a broad range of fast Li-ion conducting inorganic SEs have been reported such as sulfides,<sup>[5,6]</sup> oxides,<sup>[7]</sup> halides,<sup>[8]</sup> and borohydrides,<sup>[9]</sup> and polymers. It has been widely acknowledged that unique challenges such as solid–solid interfacial issues, cracking of SEs, Li metal penetration through SE, and so on contribute fundamentally to the poor cycle life, limited rate capability, and insufficient capacity retention of the prototype SSLBs, as recently summarized by the excellent works from Shao's group,<sup>[10]</sup> Janek's group,<sup>[11]</sup> McDowell's group,<sup>[12]</sup> Bruce and co-workers,<sup>[13]</sup> Zhang and co-workers,<sup>[14]</sup> Park's group,<sup>[15]</sup> Yang's group,<sup>[16]</sup> Viswanathan's group,<sup>[17]</sup> Meng's group,<sup>[18]</sup> Zhao and co-workers,<sup>[19]</sup> and others.<sup>[20–23]</sup> Among these challenges, the uncontrollable growth of Li electrodeposits in forms of filaments/needles/dendrites (hereafter the “dendrites” will be used) through the SEs, which is the so-called Li penetration, poses severe challenge in developing and

## 1. Introduction

All-solid-state lithium battery (SSLB) technology, which integrates high-capacity transition metal-based cathode, Li metal anode, and the nonflammable solid electrolyte (SE) as battery

J. Yao, G. Zhu, J. Ju, F. Sun, G. Cui  
Qingdao Industrial Energy Storage Research Institute  
Qingdao Institute of Bioenergy and Bioprocess Technology  
Chinese Academy of Sciences  
266101 Qingdao, China  
E-mail: sunfu@qibebt.ac.cn; cuigl@qibebt.ac.cn

J. Yao, G. Zhu, J. Ju, F. Sun, G. Cui  
Shandong Energy Institute  
Qingdao 266101, China

 The ORCID identification number(s) for the author(s) of this article can be found under <https://doi.org/10.1002/aesr.202300165>.

© 2023 The Authors. Advanced Energy and Sustainability Research published by Wiley-VCH GmbH. This is an open access article under the terms of the Creative Commons Attribution License, which permits use, distribution and reproduction in any medium, provided the original work is properly cited.

DOI: 10.1002/aesr.202300165

J. Yao, G. Zhu, J. Ju, F. Sun, G. Cui  
Qingdao New Energy Shandong Laboratory  
Qingdao 266101, China

K. Dong  
Multi-disciplinary Research Division  
Institute of High Energy Physics  
Chinese Academy of Sciences  
Beijing 100049, China

M. Osenberg, A. Hilger, I. Manke  
Institute of Applied Materials  
Helmholtz-Zentrum Berlin für Materialien und Energie  
Hahn-Meitner-Platz 1, 14109 Berlin, Germany

H. Markötter  
Bundesanstalt für Materialforschung und –Prüfung  
Unter den Eichen 87, 12205 Berlin, Germany

manufacturing next-generation SSLBs due to a significant loss of energy efficiency and catastrophic cell failure via short-circuiting. Hence, addressing this Li penetration bottleneck will not only achieve high-safety, energy-dense SSLBs but also accelerate their practical adoptions.

The mechanisms of Li electrodeposits growth and penetration through SE have become an important battery research topic after Monroe and Newman published their seminal work.<sup>[24]</sup> According to their criterion, SEs possessing shear modulus of twice that of Li are expected to be the potential option to block the growth of Li dendrites. With that being said, several experimental investigations using SEs that meet this criterion still report the Li dendrites growth along or through surface defects,<sup>[25]</sup> grain boundaries (GBs),<sup>[26]</sup> and interconnected open voids.<sup>[27]</sup> Furthermore, the short circuit occurring in SSLBs is found frequently to be even faster than that in the conventional lithium-ion battery technology, which is beyond expectation.<sup>[28]</sup> These experimental findings suggest that the mechanical strength seems to be one of the crucial factors that affect Li dendrites growth and penetration. Therefore, a fundamental and thorough understanding of the growing and penetrating mechanisms of Li electrodeposits in the presence of SEs becomes highly desirable.

Various characterization methods using *ex situ*, *in situ*, and/or *in operando* analytical probing tools are developed to probe the growth and penetration dynamics of Li dendrites in SSLBs because the electrochemical measurements alone are insufficient to provide enough insights into the continuously evolving Li dendrites and SEs. Optical microscopy (OM),<sup>[29]</sup> scanning electron microscopy (SEM),<sup>[30]</sup> transmission electron microscopy (TEM),<sup>[31]</sup> and X-ray computed tomography (XCT, also the synchrotron X-ray CT [SXCT])<sup>[32]</sup> provide intuitional morphological/phenomenological information of the Li dendrites, SEs, and the solid–solid interface. X-ray diffraction (XRD),<sup>[33]</sup> X-ray photoelectron spectroscopy,<sup>[34–36]</sup> time-of-flight secondary ion mass spectrometry,<sup>[37]</sup> energy-dispersive spectroscopy,<sup>[11]</sup> nuclear magnetic resonance,<sup>[38]</sup> and neutron depth profiling (NDP)<sup>[39,40]</sup> are able to reveal the direct information related to the Li distribution and/or SE structural/compositional evolution.

These *in-depth* studies provide novel insights into the mechanical origins of Li dendrites growth and penetration through SEs. For example, recent findings have revealed the unusual mechanical properties of Li metal such as its size effects,<sup>[41]</sup> crystallographic orientation-dependent elastic modulus,<sup>[42]</sup> temperature- and strain-rate-dependent stress-strain behavior,<sup>[43]</sup> time-dependent extensive deformation via creep,<sup>[44]</sup> and non-negligible work-hardening behavior,<sup>[45]</sup> highlighting the importance of understanding the effect of Li mechanical properties on Li penetration. Additionally, high electronic conductivity of the SE is proposed as an alternative mechanism that explains the direct nucleation and growth of Li electrodeposits within the SEs,<sup>[46]</sup> besides the conventional understanding that the Li electrodeposition-induced mechanical stress could first fracture the SE and then the generated cracks facilitate the subsequent Li penetration.<sup>[29]</sup> Moreover, experimental results disclose complex interplays between mechanical and electrochemical interactions during the Li electroplating and stripping process, manifesting unique electrochemomechanical coupling during Li dendrites

penetration.<sup>[47–49]</sup> These results contribute to a deep understanding in Li dendrites growth mechanisms in SSLBs.

Many review articles have covered recent research progress and status on studying and controlling Li dendrites growth and penetration in SEs during SSLBs operation. Janek and Zeier suggested that overcoming the Li dendrite challenges is a prerequisite in speeding up SSLBs for full-scale commercialization.<sup>[50]</sup> Foroozan et al. presented an *in-depth* review summarizing the latest works that concentrate on the Li dendrite formation mechanisms using multiple *in situ* and *in operando* imaging techniques.<sup>[51]</sup> McDowell's group reviewed the chemo-mechanical challenges in solid-state batteries with a particular focus on Li dendrites growth through SEs.<sup>[12]</sup> Deng's group summarized the strategies for controlling/regulating Li dendrites growth and penetrations in SEs, e.g., developing novel SE materials, Li anode structure engineering, introducing coating layers, etc.<sup>[52]</sup> However, most of the previous reviews pay less attentions to the tactics exploiting external physical fields in regulating Li dendrites growth in SEs, such as mechanical force, temperature, magnetic field, electric field, and pulse current. As the deployment of the external fields is generally straightforward and cost-effective, it does not require additional material processing steps and new materials that eventually increase battery cost and complexity. A recent review from Amine's group critically summarized the research process of using mechanical force and temperature physical fields in achieving high-performance lithium metal batteries.<sup>[53]</sup> Nevertheless, other strategies utilizing magnetic field, electric field, and pulse current to regulate Li dendrites growth have not yet been surveyed. Hence, an overview summarizing the strategies exploiting external physical fields in regulating Li dendrites penetration through SEs in solid-state Li metal batteries (SSLMBs) is urgent and necessary.

This review aims to summarize the recent research progress of utilizing external physical fields in regulating Li dendrites growth and penetration through inorganic SEs. We will start by introducing briefly the mechanical properties of Li metal and SEs, which are conducive for understanding the experimentally observed Li dendrites penetration phenomena. Then, the experimental results obtained from various imaging techniques, which can provide direct and straightforward information of the Li dendrites nucleation and growth process, are reviewed. Subsequently, the potential mechanistic origins of Li dendrites growth and penetration mechanisms are summarized. Based on these experimental results and the derived mechanisms, strategies exploiting external physical fields in regulating Li dendrites growth in SEs (or liquid electrolytes in some cases) are summarized. Finally, the review concludes with a discussion of the bottleneck in further precisely unravelling the lithium dendrites growth mechanism when matching with SEs as well as remaining open questions in the quest for high-safety, energy-dense SSLMBs.

## 2. Overview of the Mechanical Properties of Li and SEs

The Li penetration phenomenon, which involves the mechanical and/or electrochemical interaction between the continuously growing Li and the stationary SE, is primarily determined by

the mechanical properties of the SE and Li. Therefore, their mechanical properties on Li penetration are of high importance. In addition, the mechanical properties also play important roles in regulating the growth dynamics of Li dendrites as well as the fracture behavior of SEs. For these reasons, a concise overview of the important mechanical properties of Li and SEs, which are crucial for gaining a comprehensive understanding of the Li penetration phenomenon, is provided in this section. Note that for a detailed review of mechanics-related degradation mechanisms of Li and SE, it is referred to other literatures.<sup>[7,54]</sup> For a detailed overview of the coupling among mechanical, (electro-)chemical, and transport properties of Li and SE, the readers are referred to the related reviews.<sup>[11,55–57]</sup>

## 2.1. Mechanical Properties of Li

It has been shown that<sup>[41,57]</sup> the elastic modulus and yield strength of Li range, respectively, from 1.9 to 7.9 GP and 0.41 to 0.89 MPa. Such deviations are usually caused by the inconsistencies in sample preparation methods, unwanted side reactions, and/or characterization error. To provide more reliable datasets of Li mechanics, Masias et al. determined the Young's modulus and shear modulus of Li were 7.82 and 2.83 GPa, respectively, using an acoustic technique.<sup>[58]</sup> Furthermore, a unique load frame inside an inert atmosphere was used to study the mechanical behavior of Li in tension and they found the yield strength of Li was 0.73 MPa. These results agree well with those reported by others.<sup>[56,57]</sup> To complement the unique mechanical properties of Li, LePage et al. conducted a systematic study of Li mechanics under a wide range of strain rates and temperatures by employing the digital-image correlation-assisted tensile testing in inert gas environment.<sup>[59]</sup> They found that Li crept easily, owing to its relatively high homologous temperature and low activation energy for self-diffusion in solid Li. The creep was fitted to a power-law creep model governed by dislocations climbing. **Figure 1a** shows the true stress  $\sigma_{\text{true}}$  against true strain  $\epsilon_{\text{true}}$  of Li in tension with the true-strain rates spanning from  $4 \times 10^{-5}$  to  $2 \times 10^{-2} \text{ s}^{-1}$ . One can also note the considerable strain hardening at the fastest strain rate ( $2 \times 10^{-2} \text{ s}^{-1}$ ). To determine the temperature-dependent creep rate, the authors conducted further uniaxial tensile tests between 198 and 398 K at  $3 \times 10^{-2} \text{ s}^{-1}$  strain rate and up to 1% strains, with the results shown in **Figure 1b**. These plots suggest the existence of strain hardening at low temperature (198 K) and a steady creep stress (plateaus) for temperatures  $\geq 248$  K. Utilizing the obtained creep stress versus the reciprocal temperature, the activation energy for dislocation climb was determined to be  $37 \pm 6 \text{ kJ mol}^{-1}$ . These findings led to the development of a constitutive model of bulk Li deformation as elastic–viscoplastic at strain rates below approximately  $10^{-3} \text{ s}^{-1}$ , as shown in **Figure 1c**.

To further study its viscoplastic behavior at room temperature, Wang et al. conducted nanoindentation tests on pure Li metal.<sup>[60]</sup> The load–displacement (L–D) curves of Li shown in **Figure 1d** exhibit obvious rate-dependent characteristics. Considering that the elastic recovery during the unloading is just several nanometers, they concluded that the indentation deformation was primarily the rate-dependent plasticity, i.e., viscoplasticity. Moreover, by considering Li as a Perzyna elastic–viscoplastic

material with work hardening and using an interactive finite element (FE) model, they discovered that the elastic modulus of Li, which is on the order of GPa, had little effect on the indentation results of Li, as shown in **Figure 1e**. This finding implies that the viscoplastic deformation of Li is more important to consider than its elastic deformation when designing SSLBs that are primarily used at room temperature conditions.

Campbell et al. investigated the mechanical and wear characteristics of Li using atomic force microscopy (AFM), finding that the hardness of highly deformed Li was  $164 \pm 33 \text{ MPa}$ , approximately a fivefold increase when compared with the unworked Li of  $29.1 \pm 4.74 \text{ MPa}$  (**Figure 1f**).<sup>[45]</sup> This finding suggests that Li can bear a significant degree of residual stress due to the non-negligible work-hardening feature. Based on these findings, they argued that the significant residual stress born by Li could reduce the dendrite formation rate and forestall dendrite propagation.

Considering that Li metal undergoes mostly mechanical compression in SSLBs, compression tests instead of tension tests could more reliably capture the pressured scenario of Li. Masias et al. studied the mechanical behavior of Li in compression and they identified the sensitivity of Li metal's compression flow stress in response to the aspect ratio (height/diameter), strain rate, and temperature.<sup>[43]</sup> It has to be noted that they referred to the stress that delineates region I from region II in the obtained stress–strain curve of Li in compression as flow stress, which is the stress needed for maintaining a tremendous plastic deformation without work hardening, as schematically shown in **Figure 1g**. They found that the defined flow stress increased with a decreasing aspect ratio and increasing strain rate at room temperature. Furthermore, they ascribed the increase in the yield strength of Li with decreasing the aspect ratio to the amplified frictional effects at the interface between the platen and Li. This barreling phenomenon, as schematically shown in **Figure 1h**, is consistent with their previous result<sup>[58]</sup> and can be attributed to the hydrostatic pinning.<sup>[61]</sup> Ding et al. conducted similar experiments using glass platen and the obtained results are in good agreement with Masias et al.<sup>[62]</sup>

Very recently, Haslam et al. critically examined the compression creep behavior of Li facing on the one side the  $\text{Li}_{6.5}\text{La}_3\text{Ta}_{0.5}\text{Zr}_{1.5}\text{O}_{12}$  SE and on the other side the Ni current collector (CC) under different conditions of stresses (1–10 MPa) and Li foil thickness (100–700  $\mu\text{m}$ ).<sup>[63]</sup> The adopted Ni–Li| $\text{Li}_7\text{La}_3\text{Zr}_2\text{O}_{12}$  (LLZO)|Li–Ni symmetrical cell during the compression creep experiments is schematically shown in **Figure 1i**. During the investigations, the authors conducted a 3 h hold of the stress so a steady-state strain rate region was expected. **Figure 1j** shows the strain curves as a function of time using 1, 5, and 10 MPa applied stresses and 100 and 700  $\mu\text{m}$  Li foil thickness. One can note that for the 700  $\mu\text{m}$  Li foil at 5 and 10 MPa, the stage I (primary) and stage II (steady-state) creep are distinguishable and the overall deformation behavior is similar to the results reported by Ding et al. in compression tests.<sup>[62]</sup> In contrast, the 100  $\mu\text{m}$  Li foil displays only plastic deformation at 5 and 10 MPa in the initial 2000 s, which is not followed by a steady-state creep behavior as the 700  $\mu\text{m}$  Li foil dose. Moreover, the results also demonstrate that 1 MPa applied stress causes <2% creep strain for both the characterized Li thickness (100 and 700  $\mu\text{m}$  thickness Li foils). Based on these results, they suggested that there exists a critical stress, which is highly

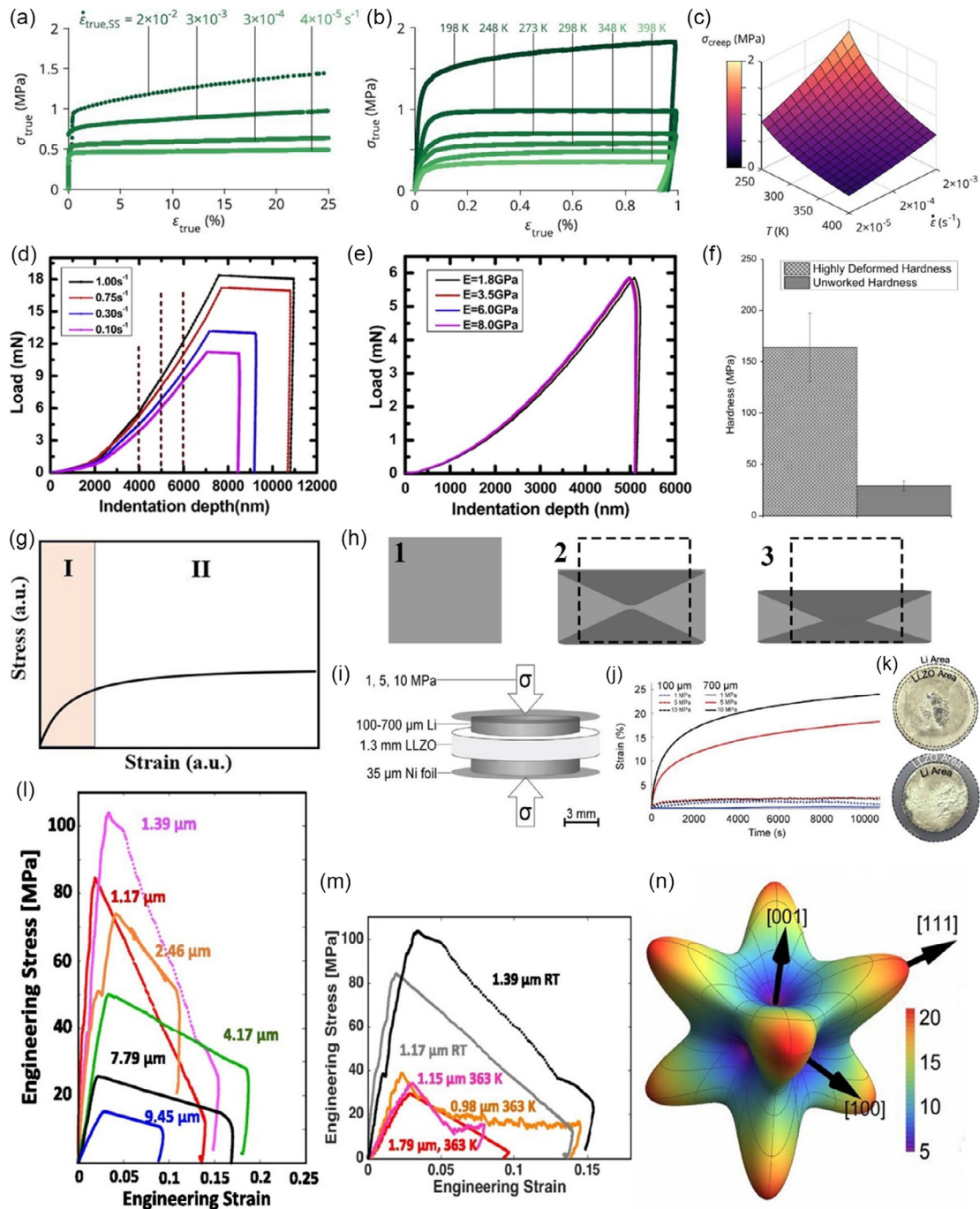


**Figure 1.** a) The true stress  $\sigma_{\text{true}}$  against true strain  $\epsilon_{\text{true}}$  of Li foil measured at 298 K and steady-state true-strain rates between  $4 \times 10^{-5}$  and  $2 \times 10^{-2} \text{ s}^{-1}$ . b) The temperature-dependent response of the Li foil between 198 and 398 K at  $3 \times 10^{-5} \text{ s}^{-1}$  strain rate. c) The creep stress for the power-law model that is valid from 248 to 398 K and  $2 \times 10^{-5}$  to  $2 \times 10^{-3} \text{ s}^{-1}$ . Reproduced under the terms of the CC BY license.<sup>[59]</sup> Copyright 2019, The Authors, Published by ECS. d) Typical L–D curves of Li foil at different strain rates. e) The effect of elastic modulus on the L–D curves, showing the curves almost overlapping with each other. Reproduced with permission.<sup>[60]</sup> Copyright 2017, Elsevier. f) A comparison of the hardness values measured under highly deformed condition and the unworked condition. Reproduced under the terms of the CC BY license.<sup>[45]</sup> Copyright 2018, The Authors, Published by Spring Nature. g) Schematic illustration of the stress–strain curve of Li in compression showing different regions of deformation behaviors. h) Schematic illustrations of the barreling phenomenon during Li compression. The darker gray shadows imply the part of Li where limited deformation occurs due to friction. i) Schematic of Ni–Li|LLZO|Li–Ni cell used in compression creep test. j) Strain versus time at 1, 5, and 10 MPa for 100 (dashed line) and 700  $\mu\text{m}$  (solid line) thick Li foil. k) Images of 100  $\mu\text{m}$  (bottom panel) and 700  $\mu\text{m}$  (top panel) thick Li foil on LLZO surface after 10 MPa creep test with Ni foil removed after testing. i–k) Reproduced with permission.<sup>[63]</sup> Copyright 2021, Elsevier. l) Engineering stress–strain curves for Li pillars with different diameters under room temperature and 363 K uniaxial compression experiments. m) Engineering stress–strain curves for  $\approx 1 \mu\text{m}$  diameter Li pillars under room temperature and 363 K uniaxial compression experiments. n) Directional dependence of the elastic modulus (in gigapascals) of Li using elastic constants obtained via DFT calculations. Reproduced with permission.<sup>[41]</sup> Copyright 2017, National Academy of Sciences.

dependent on the Li thickness and the adhesion degree between Li and SE (or CC), that causes a sustained creep deformation. Afterward, they removed the Ni foil subjected to the creep test at 10 MPa and they found that the 100  $\mu\text{m}$  Li foil retained its initial diameter, while the 700  $\mu\text{m}$  Li foil had significantly expanded in diameter and fully covered the LLZO SE (Figure 1k). They argued that the smaller strain for thinner Li foils was attributed to an amplified friction at the Li|LLZO and Li|Ni interface, where hydrostatic stress dominated the deviatoric (shape-changing) stresses as a result of friction.

The reported Li creep deformation behavior has important implications for SSLBs. First, the findings suggest that the externally applied higher pressure may not necessarily enhance the overall battery performance if the employed Li anode is thin and in a hydrostatic stress state. Second, in contrast with the conventional wisdom that Li creeping under high stack pressure could occur around the SE in a SSLB and results in external short circuits, the dominantly hydrostatic stress experienced by Li of low aspect ratios should largely prevent Li creep under stack pressure, which is favorable for decreasing the likelihood of battery short circuits. Third, the results also suggest that different mechanical properties of Li may appear during the course of battery cycling because the battery cycling could change the aspect ratio of Li significantly, which, in turn, alters tremendously the creep behavior of Li. Fourth, the proposed hydrostatic stress state of thin Li metal induced by the frictional forces from the CC or SE is not advantageous for the void rehabilitation due to the decreased creep rates. Last but not least, the hydrostatic component of stress experienced by Li metal in a SE flaw under external pressure could dominate the deviatoric component stress that facilitates Li deformation and thus the pressure relieve, resulting in the buildup of sufficient pressure to further cause SE fractures.

Besides the above-shown Li bulk mechanical research, the characterization of nanomechanics of Li provides more interesting and unexpected results at nanometer scale. Recently, Xu et al. conducted a detailed nanomechanical experiments of micrometer-sized Li pillars in an in situ SEM.<sup>[41]</sup> Figure 1l indicates that the yield stresses at room temperature increase significantly as the diameter of the Li pillar decreases. Then they performed another series of microcompression experiments at different temperature conditions and the results shown in Figure 1m reveal that the yield strength of  $\approx 1 \mu\text{m}$  diameter sample decreases from  $\approx 95 \text{ MPa}$  (at 298 K) to  $\approx 35 \text{ MPa}$  (at 363 K). Moreover, the authors used density functional theory (DFT) to calculate the elastic moduli of Li and the results confirmed that the mechanical properties of Li varied significantly with crystallographic orientations, as displayed in Figure 1n, showing spherical plots of the directional dependence of elastic modulus of Li. Similar size effect and the elastic anisotropy of Li have also been reported by others.<sup>[42,44]</sup>

These findings have significant implications for the penetration of Li dendrites. On the one hand, the yield strength of  $\approx 1 \mu\text{m}$ -sized Li found to be 105 MPa at room temperature is twice as much as the previously believed bulk strength of Li, which is between 0.41 and 0.89 MPa. This indicates that the electrochemical deposition and growth of Li into small-scale defects at the Li|SE interface can result in a much higher stress intensification than expected based on the yield strength of bulk,

polycrystalline Li. And the increased strength of Li at microscale levels can help explain how soft Li is able to penetrate hard inorganic SE ceramics in SSLBs.<sup>[42]</sup> On the other hand, the observed reduction in yield strength by a factor of three at 363 K is significant when compared to the minor decrease in shear modulus, suggesting that suppressing dendrites by inducing plastic deformation will be much more efficient at high temperatures. Last but not least, these findings suggest that the high elastic anisotropy of Li requires further research to design and fabricate engineered Li anodes with specific crystallographic orientations.

## 2.2. Mechanical Properties of SEs

The mechanical properties of the inorganic SE, in addition to Li, also play a significant role in Li penetration through the SEs. This section summarizes the recent experimental findings of the mechanical properties of SEs that may be responsible for the widely observed Li penetration phenomena.

Ni et al. conducted the first study of the room temperature values of Young's modulus, shear modulus, bulk modulus, and hardness values of LLZO garnet SE fabricated by hot pressing using resonant ultrasound spectroscopy and Vickers indentation.<sup>[64]</sup> They found that for LLZO SEs possessing volume fraction porosity of 0.03 and 0.06, the Young's moduli were, respectively,  $149.8 \pm 0.4$  and  $132.6 \pm 0.2 \text{ GPa}$ . The trend of decreasing elastic moduli with increasing porosity was consistent with the general trend observed for bulk polycrystalline specimens.<sup>[65]</sup> Yu et al. later determined the elastic constants and moduli for Al- and Ta-doped LLZO by combining first-principle calculations, acoustic impulse excitation measurements, and nanoindentation experiments.<sup>[66]</sup> They found that the Young's moduli and shear moduli for the Al/Ta-doped LLZO were, respectively, 140–150 GPa and approximately 60 GPa, which were one order of magnitude greater than those for Li metal. Jackman et al. determined the Young's modulus of lithium aluminum titanium phosphate (LATP) to be 81–115 GPa and they found that the Young's modulus and the ionic conductivity of LATP were closely correlated with the grain size and microcracking.<sup>[67]</sup> Cho et al. studied<sup>[68]</sup> the mechanical properties of the perovskite ( $\text{Li}_{0.33}\text{La}_{0.57}\text{TiO}_3$ , LLTO) SE that was manufactured utilizing either a solid-state or sol-gel process and they found that the Young's moduli for sol-gel LLTO and solid-state LLTO were, respectively,  $186 \pm 4$  and  $200 \pm 3 \text{ GPa}$ . These values were higher than other SEs such as LLZO and LATP. Recently, Herbert et al. characterized<sup>[69]</sup> the elastic modulus and hardness of lithium phosphorous oxynitride (LiPON) films ranging from 1 to 10  $\mu\text{m}$  in thickness and they found that the modulus of LiPON was approximately 77 GPa and the hardness was approximately 3.9 GPa. The L–D data also revealed that LiPON exhibited some time-dependent deformation behavior, suggesting that creep may play a crucial role in reducing large stresses.

Considering that inorganic SEs contain various sizes of flaws/defects, the fracture toughness ( $K_{IC}$ ), which is a quantitative measure of a material's ability to resist brittle fracture when a crack is present, becomes important in predicting the capability of the SE containing a crack to resist further fracture during Li penetration.<sup>[70]</sup> Cho et al. determined the  $K_{IC}$  of the hot-pressed (HP) LLTO samples using the indentation technique aided by the

optically microscopy to be  $1 \text{ MPa m}^{1/2}$ . Considering that the  $K_{IC}$  values for an ideal brittle material, e.g., glass, are close to  $1 \text{ MPa m}^{1/2}$ , they concluded that the LLTO SE was brittle and its fracture toughness needed to be improved.<sup>[68]</sup> Jackman et al. determined the  $K_{IC}$  of L ATP to be  $1.1 \pm 0.3 \text{ MPa m}^{1/2}$  using a single-edged precracked beam fracture toughness measurement.<sup>[67]</sup> Wolfenstine et al. conducted the first investigation of fracture toughness of LLZO using an indentation technique together with the subsurface crack propagation analyzed using focused ion beam-scanning electron microscopy (FIB-SEM).<sup>[71]</sup> **Figure 2a** shows a typical Vickers indent in the LLZO specimen, featuring clear cracks that originate from the corners of the indent. The area of LLZO removed for FIB-SEM analysis is outlined in black box and the dashed lines indicate three salient points along the crack trajectory, which are shown in **Figure 2b** in detail. One can note that at points C1 and C2, the crack length approximately follows an elliptical path. However, at point C3, the crack length diverges from the elliptical path, which is thought to be caused by the lateral cracks that appear in the inset at C3. Overall, **Figure 2b** shows that the subsurface crack trajectory appears elliptical and suggests a half-penny crack. The  $K_{IC}$  values of LLZO were calculated to be  $0.86\text{--}1.63 \text{ MPa m}^{1/2}$ , which is within the typical range

for polycrystalline ceramics ( $1\text{--}5 \text{ MPa m}^{1/2}$ ) and is in close agreement with those of LLTO and L ATP.

The mechanical properties of sulfide-based SEs are extremely difficult to characterize due to their high sensitivity to moisture. For this reason, the sulfide SEs were usually measured in glove box filled with inert gases or immersed in protective mineral oil. Sakuda et al. studied the mechanical properties of  $\text{Li}_2\text{S-P}_2\text{S}_5$  (LPS) sulfide SE using the ultrasonic pulse method and determined its Young's modulus of  $18\text{--}25 \text{ GPa}$  for HP pellets and  $14\text{--}17 \text{ GP}$  for cold-pressed pellets.<sup>[72]</sup> Baranowski et al. conducted the first nanoindentation of  $\beta\text{-Li}_3\text{PS}_4$  SE and they found that the bulk modulus of 80% dense LPS was  $10\text{--}12 \text{ GPa}$  and predicted a value of  $16 \text{ GPa}$  for the 100% dense material.<sup>[73]</sup> McGrogan et al. used instrumented indentation to quantify the mechanical properties of amorphous LPS SE prepared by melt-quenching and they found that<sup>[74]</sup> the elastic modulus and hardness were, respectively,  $18.5 \pm 0.9$  and  $1.9 \pm 0.2 \text{ GPa}$ . In addition, the fracture toughness  $K_{IC}$  was calculated to be  $0.23 \pm 0.04 \text{ MPa m}^{1/2}$  using the optically measured crack length. The calculated  $K_{IC}$  is more than a factor of two lower than the oxide SEs exhibiting  $K_{IC}$  range of  $0.86\text{--}1.63 \text{ MPa m}^{1/2}$ . The findings indicate that the LPS SE exhibits low resistance to reversible deformation and is

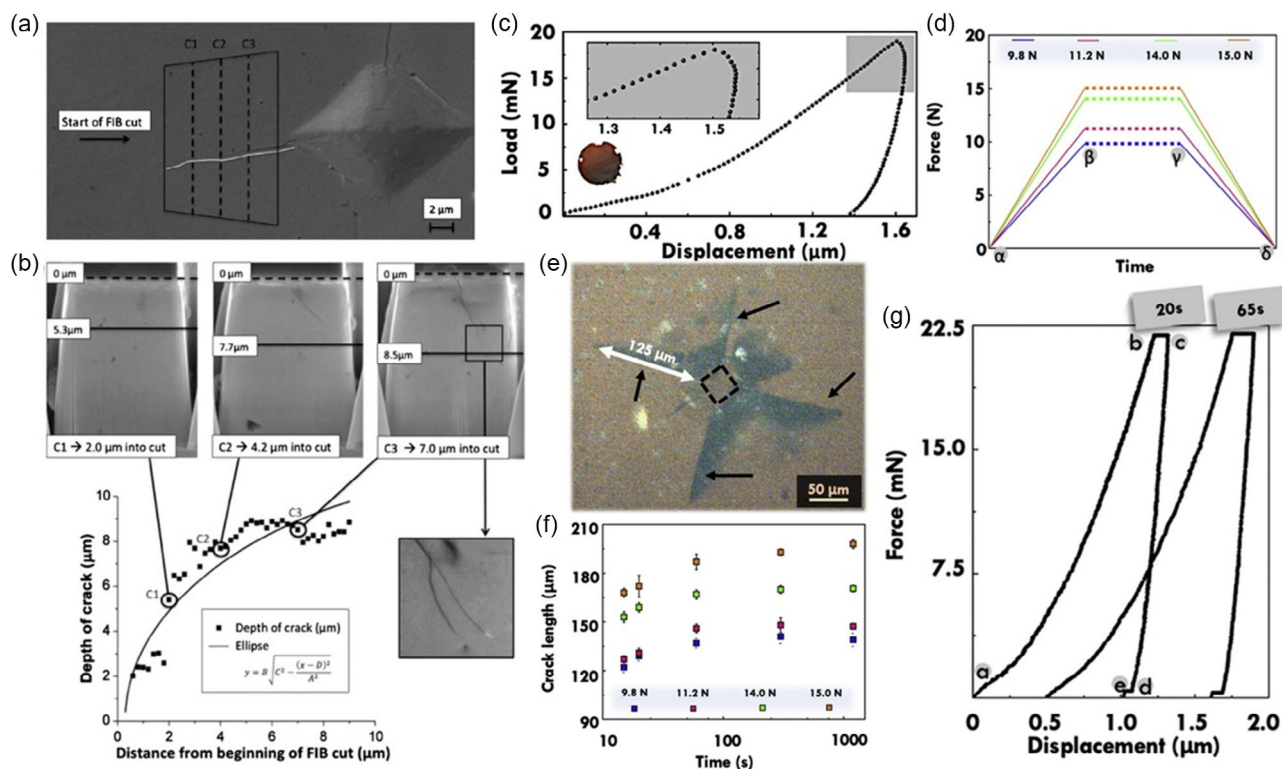


**Figure 2.** a) SEM image demonstrating a typical Vickers indent and the area where FIB excavation was executed. The LLZO removal initiates on the left and proceeds toward the indentation. The white line located beneath the crack indicates the trajectory of the crack. The dashed lines C1–C3 demarcate the locations of the images displayed in (b). b) The top panels display FIB SEM images in relation to the proximity to the indentation. The lower figure presents a graph of crack depth versus the distance from the start of the FIB cut, with a solid curve representing an elliptical fit. Reproduced with permission.<sup>[71]</sup> Copyright 2013, Elsevier. c) Representative L–D curve of the measured sulfide SE exhibiting a bow-shaped unloading segment (zoomed-in in the inset figure). d) The loading patterns for the Vickers indentation tests. e) The OM image of the sample after indentation-induced cracking. f) The crack lengths for different indentation depths are obtained by changing the holding durations and loads. g) The L–D curves in the modified loading pattern. The measurements were performed with a loading rate of  $1 \text{ mN s}^{-1}$  (segment a–b) and an unloading rate of  $-1 \text{ mN s}^{-1}$  (segment c–d). Reproduced under the terms of the CC BY license.<sup>[81]</sup> Copyright 2022, The Authors, Published by Elsevier.

compliant in nature, while also being brittle and having low resistance to fracture. Recently, Hikima et al. studied the mechanical properties of 75Li<sub>2</sub>S–25P<sub>2</sub>S<sub>3</sub> sulfide SE using indentation methods and they found that its mechanical properties such as Young's modulus and hardness varied depending on the fabrication methods (mechanical milling vs liquid phase shaking) and the pressing temperature (cold pressing vs hot pressing).<sup>[75]</sup>

The majority of previous studies concentrated on the mechanical properties of sulfide SEs under static loading conditions, rather than the dynamic loading conditions that are more relevant to actual battery operating conditions.<sup>[76–80]</sup> Hence, Athanasiou et al. conducted an in-depth study of the rate-dependent deformation of amorphous sulfide SEs for SSLBs.<sup>[81]</sup> Figure 2c shows the typical indentation L–D curves for the SE measured using an instrumented indentation equipped with a Berkovich cell tip. The curve displays a bow shape during the initial stage of unloading, which is an indication of creep deformation. Subsequently, they used Vickers indentation to study the fracture characteristics of the sulfide SEs, with the applied loading pattern depicted in Figure 2d. A typical radial crack caused by the indentation of the indenter tip in a load-controlled manner is shown in Figure 2e. By analyzing the radial crack length generated under different applied loads, it is observed from Figure 2f that the radial crack length exhibits a strong dependence on the indentation holding time, which is indicative of the rate-dependent mechanical behavior. To delve deeper into the viscoelastic and viscoplastic influences on the materials response, they executed a series of loading, holding, unloading, and holding with varied rates to differentiate recoverable and nonrecoverable deformation. Figure 2g displays the L–D curves in the scenario of modified loading patterns with holding times of 20 and 65 s. Both curves were measured with loading rate 1 mN s<sup>−1</sup> (segment a–b). During the holding stage (segment b–c), creep deformation occurred as the maximum load was maintained for 20 or 65 s. The total increase in nanoindentation displacement during the holding period was the sum of the viscoelastic and viscoplastic displacements. During the unloading segment (−1 mN s<sup>−1</sup> unloading rate, segment c–d), all the inviscid elastic deformation was recovered. And during the second holding step for 35 s at less than 5% of the maximum load (segment d–e), the displacement change was dominated by the recovery of viscoelastic deformation. Comparing segments b–c and d–e, which are, respectively, large and small, suggests that the viscous behavior of sulfide SE is governed by viscoplasticity rather than viscoelasticity.

The findings regarding the viscoplastic deformation of sulfide SEs in this study have significant implications for their use in SSLBs. First, the unusual viscoplastic behavior of sulfide SEs will cause these materials to react differently to mechanical forces. The low yield stress of the sulfide SEs introduces additional complexity to predict and/or describe their deformation behavior because they might deform plastically when interacting with Li dendrites during battery operation. Second, the results of these experiments highlight the difficulties involved in accurately measuring and describing the fracture toughness of sulfide SEs due to their rate-dependent behavior. It is suggested that the fracture toughness values measured using standard indentation methods for sulfide SEs may not be representative of the material's general fracture resistance. Despite this, the viscoplastic deformation

of sulfide SEs may provide a promising solution for reducing stress-driven Li penetration, as the local inelastic deformation of the SEs can help to alleviate local stress concentrations near the filament tip.

Recently, Papakyriakou et al. conducted a comprehensive and in-depth investigation of temperature-dependent mechanical behavior of several inorganic sulfide (Li<sub>10</sub>SnP<sub>2</sub>S<sub>12</sub>, LSPS and Li<sub>6</sub>PS<sub>5</sub>Cl, LPSCl) and LLZTO type oxide (Li<sub>1.5</sub>Al<sub>0.5</sub>Ge<sub>1.5</sub>P<sub>3</sub>O<sub>12</sub>, LAGP and Li<sub>6.4</sub>La<sub>3</sub>Zr<sub>1.4</sub>Ta<sub>0.6</sub>O<sub>12</sub>) SEs using the environmentally controlled, variable-temperature nanoindentation method.<sup>[82]</sup> In addition, two types of LLZTO were used in this study, which were derived from different synthesis routes. The first type is the cold-pressed and subsequently sintered LLZTO, while the second type is the HP LLZTO. Figure 3a shows the representative indentation L–D curves for all the SEs as well as the fused quartz (FQ) reference material at 25 °C, showing that the sulfide materials exhibit significantly higher indentation displacements than the oxide and reference materials. This result indicates that the former is much softer than the latter ones. The hardness values of the tested materials as a function of temperature are shown in Figure 3b, demonstrating the general trend that increased temperature causes the softening and higher compliance of all the materials. Moreover, the authors examined the temperature dependence of the reduced modulus of the tested materials, revealing that the oxides and FQ possess a significantly higher reduced modulus than the sulfides. Additionally, the sulfides exhibited a greater temperature dependence than the oxide materials. These temperature-dependent properties of SEs suggest that SSLBs using SEs may not be effectively designed and modeled with the assumption of temperature-independent elastic and plastic properties. The authors also investigated the viscoelastic properties of these SEs at different temperatures and found that both the sulfide and oxide SEs exhibited a similarly low level of viscoelastic damping.

Figure 3c–f summarizes the viscoplastic creep results of these SEs. Figure 3c shows the typical creep displacement for each material when subjected to a constant indentation load of 2000 μN at 25 °C, indicating that creep deformation takes place gradually in all tests. Using the power-law creep model given by Equation (1),

$$\dot{\epsilon}_{\text{eff}} = B \left( \frac{\sigma_{\text{eff}}}{\sigma_0} \right)^n \quad (1)$$

in which

$$\sigma_{\text{eff}} = \frac{P}{A_p} \quad (2)$$

is the effective compressive stress beneath the indenter,  $P$  is the indentation load,  $A_p$  is the projected contact area,  $\sigma_0$  is a normalizing reference stress,  $n$  is the stress exponent, and  $B$  is the creep rate coefficient. The  $\dot{\epsilon}_{\text{eff}}-\sigma_{\text{eff}}$  relationship shown in Figure 3d is found to be linear on the log–log scale, validating this power-law creep model. As the stress exponent  $n$  reflects the sensitivity of creep rate to an applied stress and can be used to imply underlying creep mechanisms, they reorganized the creep data into the Arrhenius-like plots shown in Figure 3e–f, where the stress exponent is plotted against  $1/T$  (K<sup>−1</sup>). Assuming creep occurs through

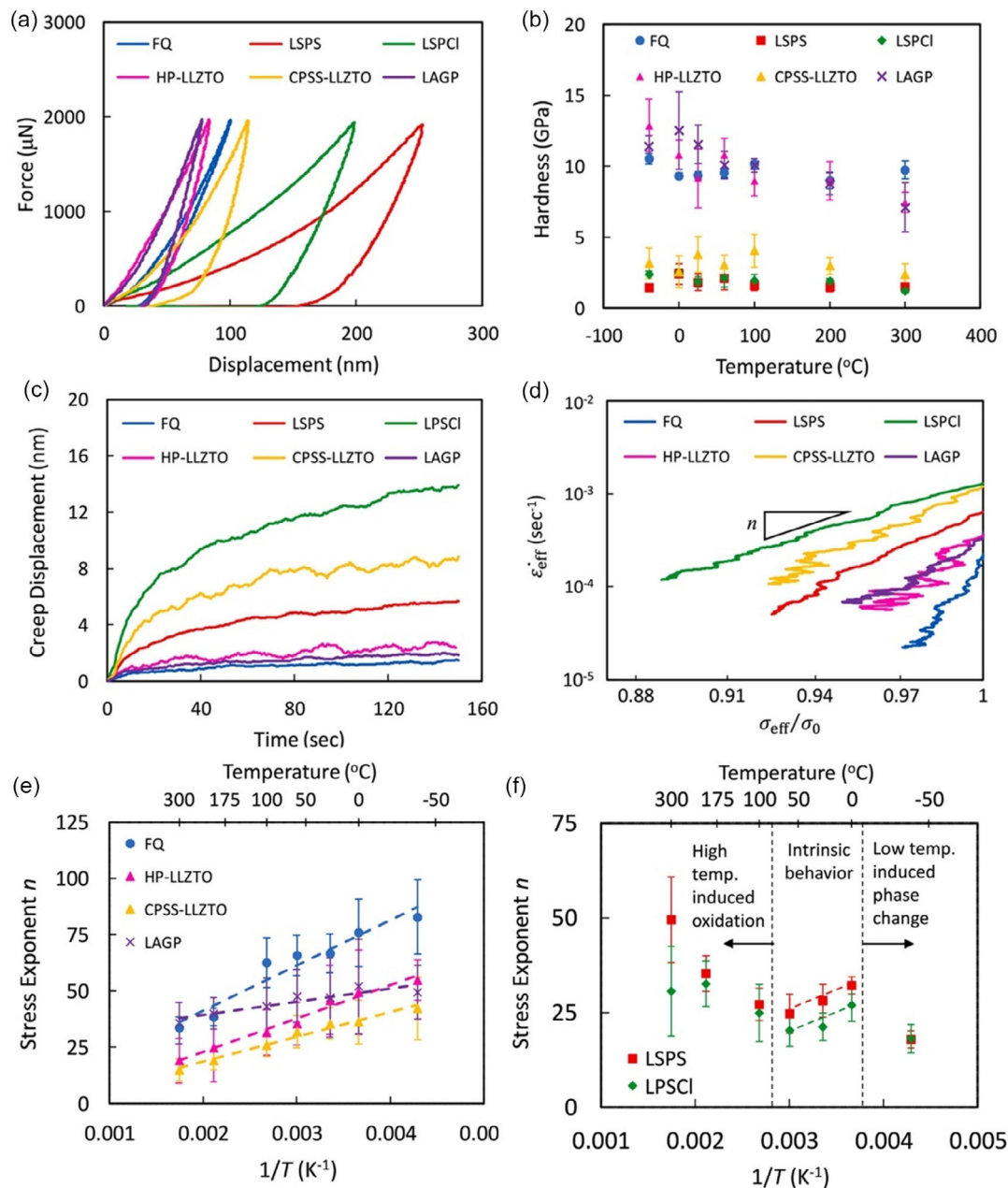


**Figure 3.** a) Representative quasistatic nanoindentation curves of the tested samples at 25 °C. b) The measured temperature dependence of hardness of the tested samples. c) Representative creep displacement versus time of the tested samples at 25 °C. d) The effective strain rate versus effective stress curves relating to (c). The slope of each curve in (d) gives the value of the stress exponent term  $n$  in Equation (3). The Arrhenius-like plots of stress exponent  $n$  versus  $1/T$  [K<sup>-1</sup>] for e) oxides SEs and FQ, and f) sulfide SEs. Reproduced with permission.<sup>[82]</sup> Copyright 2021, Elsevier.

a stress-driven, thermally activated process and considering the relation between the stress exponent and temperature can be expressed by Equation (3),

$$n = \frac{HV}{3\sqrt{3}k_B} \frac{1}{T} \quad (3)$$

where  $H$  is the indentation hardness,  $V$  is the activation volume,  $k_B$  is the Boltzmann constant, and  $T$  is the temperature. One can

note that the oxide SEs, as shown in Figure 3e, are seen to experience a linear increase in stress exponent with increasing  $1/T$ , which agrees with Equation (3). By fitting the stress exponent data using this equation, they concluded that dislocation movement was the dominant viscoplastic creep mechanism in the oxide SEs. On the other hand, the sulfide SEs exhibit a more complicated, nonmonotonic trend with changing temperature, as shown in Figure 3f. Hence, they studied the stress exponent of sulfide SEs in three different temperature ranges:



temperatures between 0 and 80 °C and temperatures  $\leq 0$  °C and  $\geq 80$  °C. It is noted in Figure 3f that the stress exponent of sulfide SEs exhibits the same linear dependence on  $1/T$  between 0 and 80 °C, hence it is suggested that the sulfide SE within this temperature range is governed by the same dislocation-controlled viscoplastic creep to that of oxide SEs. Beyond this temperature range, there are deviations from this behavior and they attributed these deviations to the composition/phase changes of the sulfide SE, e.g., decompositions of sulfide SE at high temperature and phase changes at low temperature.

It must be noted that SEs may also possess strong size effect regarding their fracture behavior. Zhao et al. revealed size-dependent chemomechanical failure of  $\text{Li}_{10}\text{GeP}_2\text{S}_{12}$  (LGPS) SE using in situ FIB-SEM imaging.<sup>[83]</sup> They observed that LGPS particles with a size greater than 3  $\mu\text{m}$  always resulted in fracture and pulverization, while particles with a size less than 3  $\mu\text{m}$  but greater than 1  $\mu\text{m}$  experienced cracking. When the particle size was less than 1  $\mu\text{m}$ , no cracks or fractures were observed. They attributed this strong size effect to the balance between the elastic energy release caused by Li reaction with LGPS and the surface energy release caused by fracture or pulverization of the particles. These results provide novel insights into the fracture behavior of SEs.

### 3. Experimental Observations of Li Penetration through SEs

After understanding the mechanics of Li and SE, one may wonder how this knowledge be translated to understand Li penetration phenomena in SSLBs. To fundamentally answer this question, a fundamental understanding of the origins of Li dendrites growth and propagation in SEs must be obtained. Although it is well known that the electrochemical deposition of Li on the working electrode is typically carried out under a constant electrical potential, which leads to the oxidation of Li metal on the counter electrode and the diffusion of  $\text{Li}^+$  ions through the SE, it is still difficult to directly observe the process of Li metal formation and growth at the Li anode. One of the reasons is attributed to the lack of suitable and reliable diagnostic tools. Therefore, researchers have developed advanced techniques that can track Li dendrites evolution during Li electrodeposition. In this section, several efficient techniques that have been developed and used to observe the dendrite evolution are summarized. Visualization characterization tools such as OM, SXCT, SEM, and TEM that are used to reveal the mechanisms of Li dendrites growth and penetration through SEs are summarized. For a detailed overview of summarizing Li dendrites using other techniques, the reader is referred to previous publications.<sup>[19,20,84]</sup>

#### 3.1. Characterizations Using OM

OM can provide a broad view of the microstructural changes in the studied electrode during battery cycling through combination with electrochemical devices. Chiang's group studied the Li penetration through four types of inorganic SEs including glass LPS,  $\beta\text{-L}_3\text{PS}_4$ , polycrystalline, and single-crystal  $\text{Li}_6\text{La}_3\text{ZrTaO}_{12}$  (LLZTO) using galvanostatic electrodeposition experiments

coupled with in situ OM.<sup>[29]</sup> Figure 4a shows the experimental apparatus used in this work, housed in an argon-filled glove box. OM images recorded during galvanostatic Li plating at 1) defect-free locations and 2) defect-containing locations using LPS SE are shown in Figure 4b. Figure 4b1–b4 shows that the Li metal deposited first on the surface of defect-free LPS and then propagated laterally from the electrode contact region, during which process no cracking was observed. In contrast, Figure 4b5–b8 shows that cracks formed and extended into the sample as Li electrodeposition progressed. The progressive crack opening was believed to be caused by the electroplating of Li metal into one or more sharp flaws (Griffith flaws) on the surface of the LPS SE. The phenomena of crack formation/propagation and Li penetration were observed using in situ OM in both LLZTO and  $\beta\text{-L}_3\text{PS}_4$  SEs. The discoveries suggest a Li penetration mechanism that involves the growth of surface flaws, indicating that the electrodeposition of metal within a surface crack can cause the crack to open and advance, even though Li has a low shear modulus and yield strength (see Section 2.1).

They proposed a suitable electrochemomechanical model to explain the observed Li penetration in the present SEs containing microscopic pores as well as GBs. According to the simplified geometries as shown in Figure 4c, they determined the extent of stress buildup using an analytical model and it gave

$$\sigma_{xx} = \sigma_0 e^{-\frac{2\nu}{h}x} \quad (4)$$

where  $\sigma_{xx}$  is the stress in the  $x$ -direction,  $\sigma_0$  is the stress at the dendrite tip, that is to say, the maximum value of  $\sigma_{xx}$ ,  $h$  is the dendrite thickness,  $\mu$  is the friction coefficient between Li and the SE, and  $\nu$  is the Poisson ratio. Then they determined the maximum value of the hydrostatic stress, which is thermodynamically determined by the applied overpotential, at which Li metal is plating

$$\sigma_{0,\text{max}} \cong -\frac{F}{V_m^{\text{Li}}} \times \Delta\Phi \quad (5)$$

$F$  is the Faraday's constant,  $V_m^{\text{Li}}$  is the molar volume of Li metal ( $13 \text{ cm}^3 \text{ mol}^{-1}$ ), and  $\Delta\Phi$  is the overpotential. This correlation implies that even a small overpotential can cause significant stress levels. If the internal stress within the flaw is assumed to be uniform, linear elastic fracture mechanics suggest that the following criterion must be met for crack propagation:

$$\sigma \geq \frac{K_{\text{IC}}}{\gamma\sqrt{\pi a}} \quad (6)$$

Here,  $K_{\text{IC}}$  is the fracture toughness,  $\gamma$  is the geometric factor, and  $a$  is the flaw size. Setting  $\sigma = \sigma_{0,\text{max}}$  yields the limiting case where the uniform internal stress is equal to the maximum hydrostatic stress expressed in Equation (5). For this limiting case, they calculated the corresponding minimum overpotential  $\Delta\Phi$ , as a function of the flaw size,  $a$ , for LPS and LLZTO. The detailed analysis provides a clear explanation as to why even small overpotentials can generate Li plating stresses that are sufficient to cause the propagation of Li dendrites through brittle SEs through Griffith-like crack extension.

Later on, Chiang's group studied the Li electrodeposition on single-crystal  $\text{Li}_6\text{La}_3\text{ZrTaO}_{12}$  (LLZTO) using in operando OM to

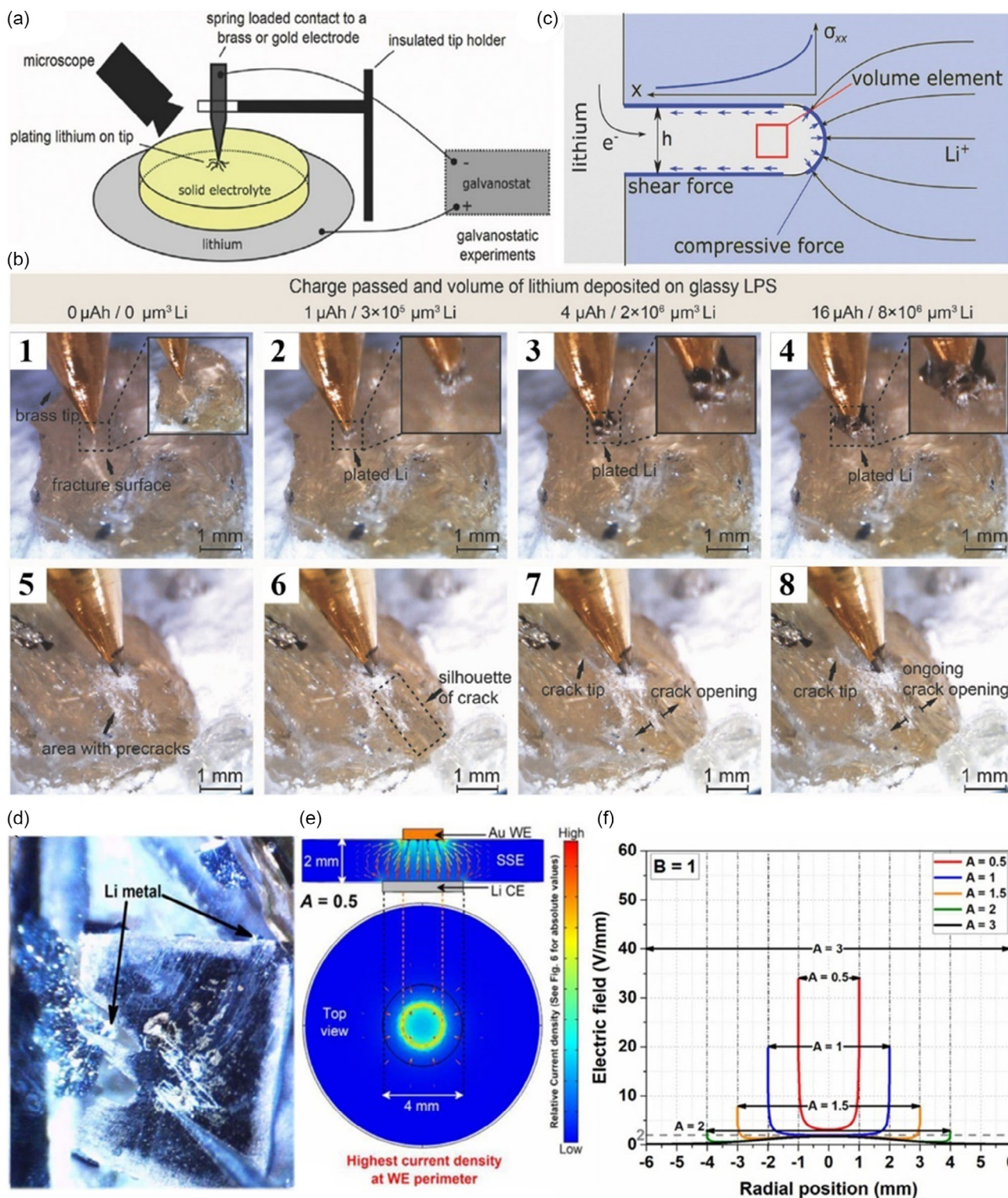


**Figure 4.** a) Schematic of the setup for Li plating. b) OM images showing Li plating. The numbers indicating the total charge passed and corresponding volume of Li metal deposited are labeled at top. Panels 1–4 show Li deposition at a pristine as-fracture surface without crack formation or propagation. Panels 5–8 demonstrate the Li deposition at a region precracked using a diamond-tipped tool and crack growth from the initially damaged region is observed. Reproduced with permission.<sup>[29]</sup> Copyright 2017, Wiley-VCH. d) Plan-view OM image of LLZTO after short-circuiting. e) The current density contour plot for an Au|SSE|Li cell with a working electrode/counter electrode diameter ratio (A) of 0.5. f) The spatial distribution of electric field for working electrode/counter electrode ratio (A) of 0.5, 1, 2, and 3 as well as for electrolyte thickness/counter electrode radius ratio (B) of 1. Reproduced under the terms of the CC BY license.<sup>[85]</sup> Copyright 2018, The Authors, Published by ECS.

investigate factors governing Li penetration behavior.<sup>[85]</sup> Figure 4d shows the plan view of the in situ OM images of the studied samples after short circuit. It was noted that Li electrodeposition took place at the edge of the gold electrode, and that there was no Li penetration from the large Vickers indentations (serving as flaws/defects) located in the center of the gold electrode. Together with the ex situ OM results, they argued that the Vickers indents did not dominate the Li electrodeposition behavior, other factors such as local electric field intensification might be. To support this assumption, they conducted FE modeling to determine the spatial distribution of electric field intensification at the edge of the gold working electrode. As depicted in Figure 4e, the Li electrodeposition current density was not uniform and was focused at the edge when the CC surface area was smaller than that of the separator and the Li source. Furthermore, as shown in Figure 4f, the electric field was about 5 times higher at a point that was 10  $\mu\text{m}$  from the edge. Based on these findings, they suggested that the amplification of the electric field drives Li penetration from areas on the SE surface with critical flaws. This accounts for the observation that crack initiation sites align with locations of maximum electric field at the CC edges, rather than the presence of larger defects in other areas.

Kazyak et al. comprehensively and systematically studied the coupled electrochemical–morphological–mechanical evolution of Li|LLZO interface using in operando OM, revealing new insights into the nature of Li penetration and propagations in SEs.<sup>[28]</sup> Figure 5 shows four groups of different types (morphologies) of Li dendrites, i.e., straight, spalling, branching, and diffuse, observed during battery cycling. The straight type of Li penetration involves a single, approximately linear path of growth. The branching type exhibits a dendritic, branching pattern. The spalling type is named for its resemblance to a piece of glass detaching from a larger sheet. The diffuse type is characterized by its tendency to occur along GBs and form a network of thin structures. These observations highlight the diversity of Li penetration types that can occur in a single cell, underscoring the inadequacy of a single explanation or mechanism to account for the complexity of the observed phenomena.

They also studied the dynamic evolution of Li dendrites during cycling using the in-plane operando OM. It was found that, although the Li dendrites appeared fully reversible during the first cycle, dead Li appeared after the second cycle, as shown in Figure 6. Dead Li was found to form by removing the electrical connection to the rest of the electrode by stripping the base of Li dendrites. However, when Li was plated back into the base, the dead Li could be reconnected to the bulk electrode and grow larger. Nevertheless, the base remained a hotspot for Li stripping, resulting in the reformation of dead Li during each subsequent stripping half-cycle. As the Li dendrites gradually propagated further with each cycle, they eventually met, causing a short circuit. By analyzing the data quantitatively, they discovered that the rate of Li dendrite propagation was directly proportional to the applied current, with a higher rate of change in Li dendrite length observed for higher currents. These results provide new insights into the underlying mechanisms of Li penetration through SEs.

Similarly, Dai et al. studied the Li penetration through LLZTO using in situ OM and also observed that when the Li dendrites emerging from both electrodes in the SE came into contact, a short circuit occurred within the cell.<sup>[86]</sup> Recently, Guo et al.

conducted a similar study using different current densities and cycling temperatures.<sup>[87]</sup> They found that at 25 °C, when the current was 100  $\mu\text{A}$ , the Li dendrites grew fast and some branches were observed, as shown in Figure 7a. The cell short-circuited after 130 s. When the current was increased to 500  $\mu\text{A}$ , Figure 7b shows that the branch-shaped Li dendrites consisting of more small branches were generated. The cell short-circuited after 26 s. They concluded that higher current densities induced more branches in Li dendrites and accelerated Li deposition rate. In addition, by comparing the morphology of Li dendrites formed at 500  $\mu\text{A}$  at 65 °C with those formed at 500  $\mu\text{A}$  at 25 °C, they found that the dendrites formed at higher temperature possessed fewer small branches. The main difference of these dendrites formed at two working temperatures was ascribed to the different ion conductivities at different temperatures. At higher temperatures, the increased conductivity of the SE allowed for more  $\text{Li}^+$  ions to accumulate near the tip of existing Li dendrites, which hindered the formation of additional branches in other areas.

Sun et al. conducted an in situ OM characterization using a Li|LPS|NCM ( $\text{LiNi}_{0.6}\text{Co}_{0.2}\text{Mn}_{0.2}\text{O}_2$ ) cell to study the Li dendrites formation mechanisms within SEs.<sup>[88]</sup> During the battery charging process, Figure 7c records the Li deposition inside LPS SE by a series of cross-sectional snapshots taken at different charging times. Panel 2 in Figure 7c shows local Li deposition appeared in the LPS SE after 3 h charging. The detachment of the LPS SE from the Li metal anode was an indication that Li dendrites were beginning to grow and cause volume expansion of the LPS SE. As the charging process continued, the area of Li deposition increased, and the gap between Li and the LPS SE also widened (panels 2–3 in Figure 7c). The growth of metallic Li within the LPS SE enhanced its electronic conductivity, resulting in preferential deposition of Li around the already-deposited Li metal, forming a silver-like Li area (panels 4–6 in Figure 7c). The visual evidence of the dynamic process of Li dendrite formation and growth within the LPS SE suggests that Li can directly nucleate and propagate within the SE due to significant electron conduction, leading to structural cracking.

It has to be noted that certain amorphous SEs, such as LiPON film that is synthesized using radio frequency magnetron sputtering, do not possess GBs or pores.<sup>[89]</sup> This unique feature of LiPON was accounted for the suppression of possible Li dendrite growth and the obtained outstanding 10 000 cycles of a thin film cell built with LiPON,  $\text{LiNi}_{0.5}\text{Mn}_{1.5}\text{O}_4$ , and Li.<sup>[90]</sup> To test this hypothesis, Westover et al. studied the Li deposition behavior using a modified thick film battery configuration with an artificial 2D LiPON–LiPON interface parallel to the cathode.<sup>[89]</sup> They found that a great deal of Li deposits were generated at the edge of Cu CC and they expanded along the confined 2D interfacial layer, forming branched tree-like structures, as shown in Figure 7d–e. This finding highlights the effectiveness of a uniform LiPON film in completely preventing the penetration of Li deposits through the SE. Very recently, Sastre et al. also demonstrated experimentally that the amorphous LLZO SE can block the Li dendrite growth in solid-state batteries.<sup>[91]</sup> They deposited a layer of  $\approx 70$  nm thick amorphous LLZO (aLLZO) on the crystallized LLZO films and the aLLZO-coated SE was obtained. The successful blockage of Li dendrite growth using the aLLZO coated SE was demonstrated by the in situ OM test, as shown

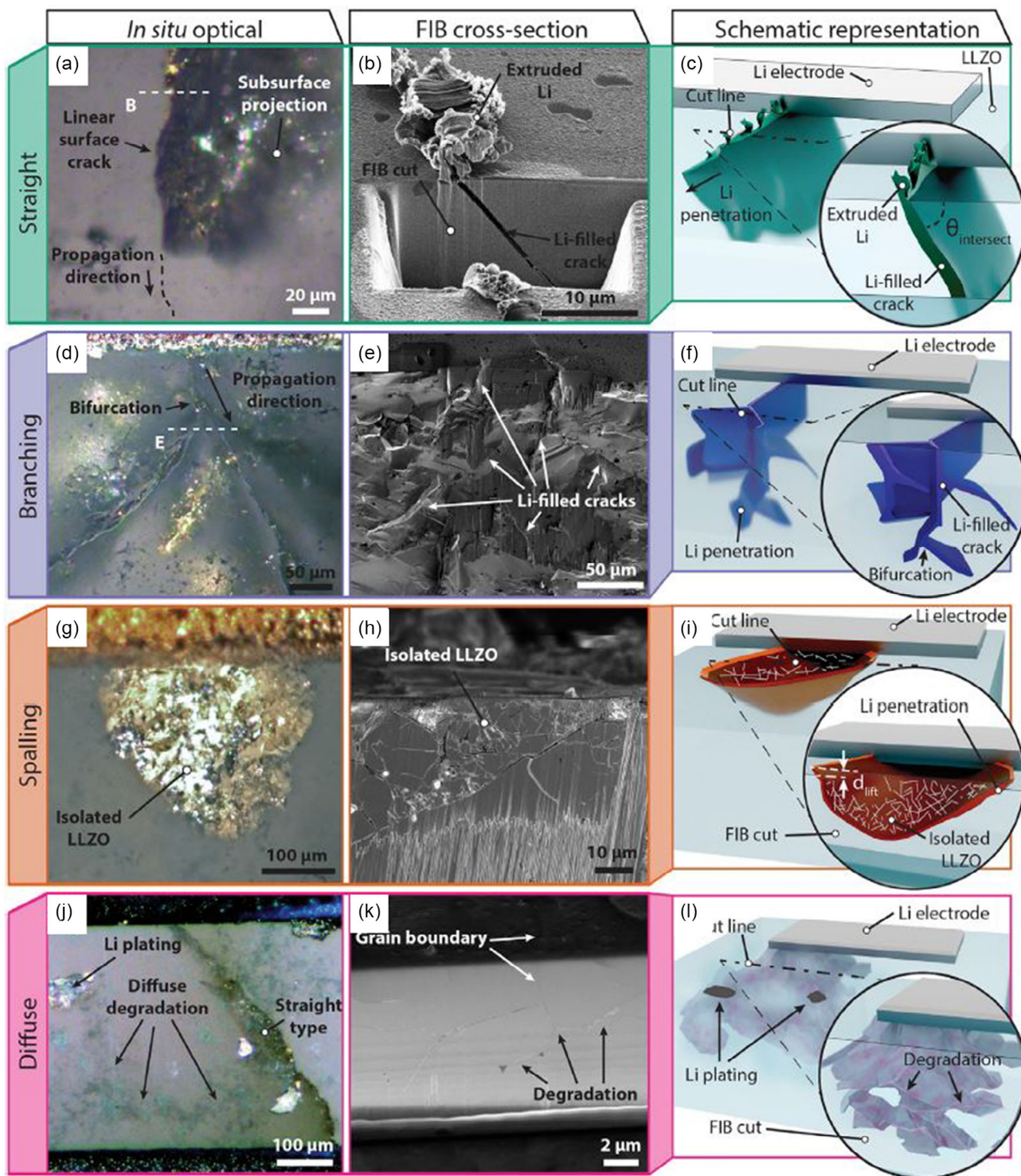


**Figure 5.** Optimal images of different types or morphologies of Li dendrites. a,d,g) Optical images and b,e,h) SEM images and c,f,l) schematics of straight Li dendrites type (a–c), branching type (d–f), spalling type (g–i) and diffuse type (j–l). Reproduced under the terms of the CC BY license.<sup>[28]</sup> Copyright 2020, The Authors, Published by Elsevier.

in Figure 7f. In contrast, the similar test using the uncoated SE displayed an internal short circuit that is caused by the Li dendrites growth connecting the two electrodes (Figure 7g).

These results highlight that synthesizing SEs of homogeneous and defect-free surface seems to be one of the most promising routes to prevent the Li penetration.

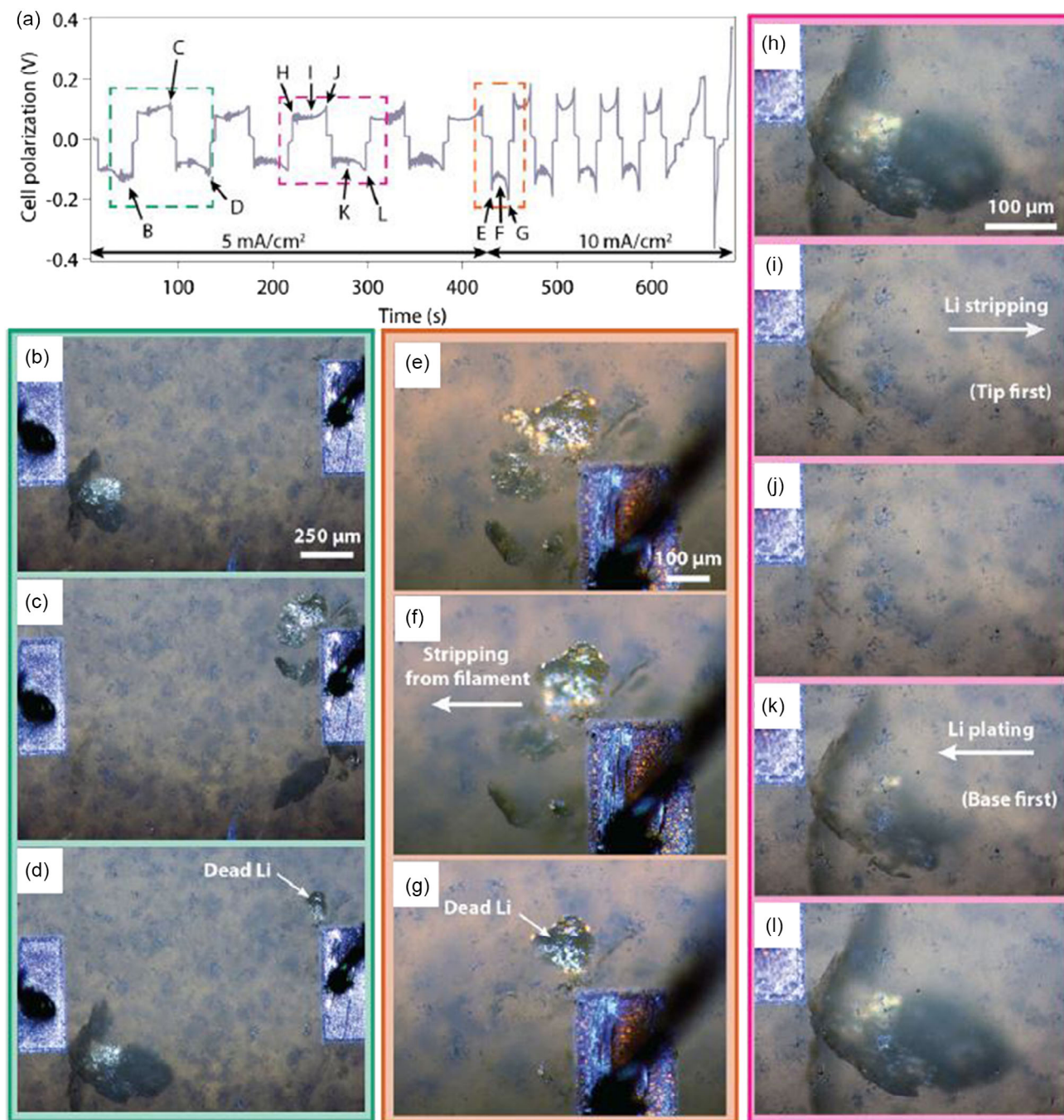


**Figure 6.** a) Voltage profile of in-plane Li symmetrical cell using LLZO SE during galvanostatic cycling at 5 and 10 mA cm<sup>-2</sup>. The labeled points correspond to the operando image in (b) to (l). Reproduced under the terms of the CC BY license.<sup>[28]</sup> Copyright 2020, The Authors, Published by Elsevier.

The in situ OM turns out to be the most widely and frequently used method to characterize Li dendrites penetration through SEs due to its easy access and simplicity. However, it has to be noted that the OM usually has a low resolution and therefore limits significantly the detection of structural evolution at nanometer scale. Characterization tools with higher spatial resolution are highly desirable for detecting the Li nucleation and SE cracking at nanometer scales.

### 3.2. Characterizations using SEM

SEM has a higher level of resolution compared to OM, making it commonly used to study the topography, dendrite nucleation, and plating/stripping process in SSLBs. Similar to optical methods, (in situ) SEM can also observe cross-sectional images of batteries with higher resolution. Additionally, the design and configuration of batteries compatible with (in situ) SEM

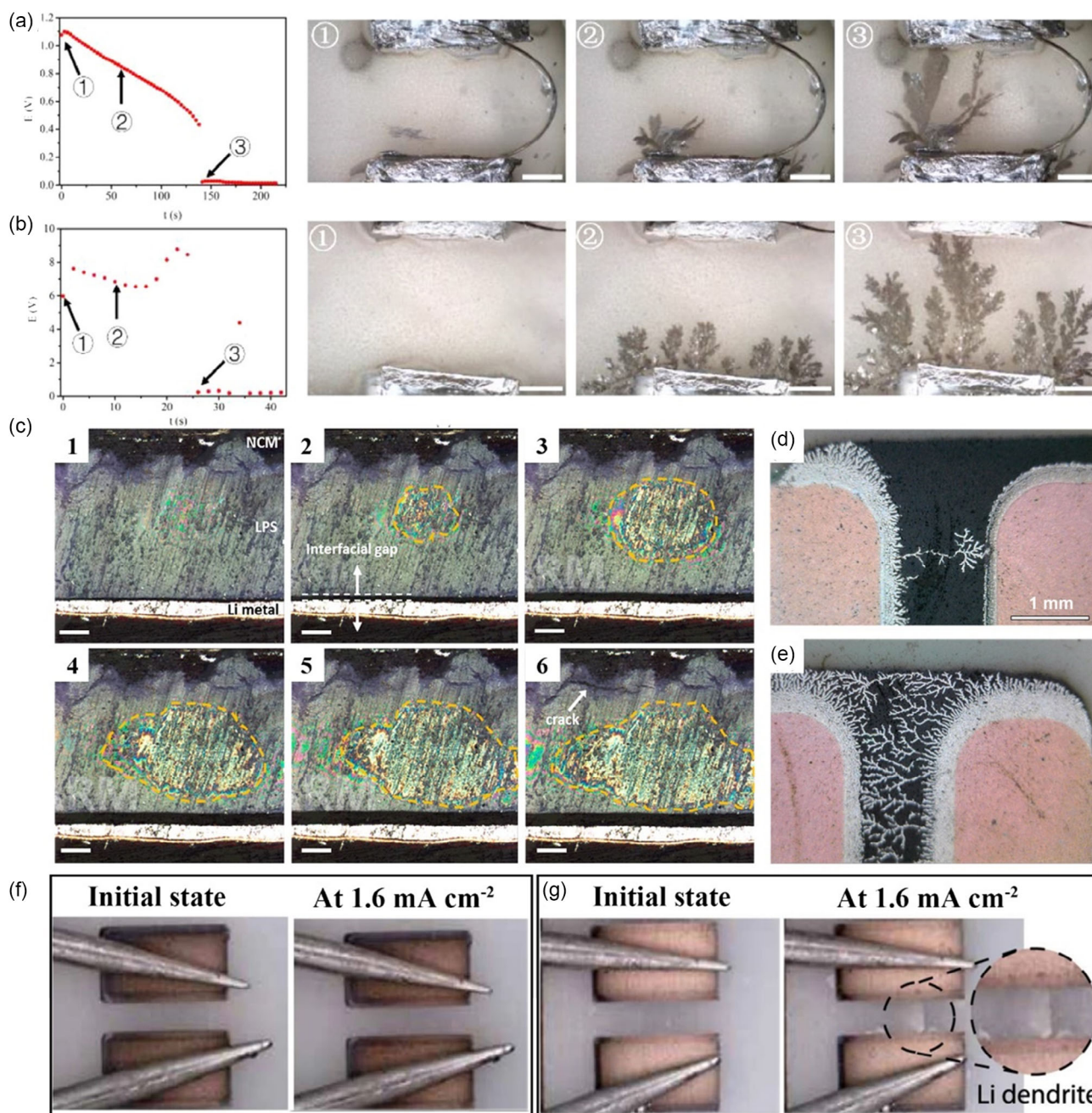


**Figure 7.** Voltage profiles and the corresponding OM images of Li|LLZTO|Li cell at a)  $100\ \mu\text{A}$  and b)  $500\ \mu\text{A}$ . The scale bar is 1 mm. Reproduced with permission.<sup>[87]</sup> Copyright 2021, Elsevier. c) The cross-sectional snapshots of the Li|LPS|NCM cell taken at 0 h (panel 1), 3 h (panel 2), 6 h (panel 3), 9 h (panel 4), 12 h (panel 5), and 18 h (panel 6) of the charging process. Scale bars are  $100\ \mu\text{m}$ . Reproduced with permission.<sup>[88]</sup> Copyright 2021, American Chemical Society. d–e) The optical micrograph of the Cu current collectors and Li tree structures grown through an artificial 2D LiPON–LiPON interface. Reproduced under the terms of the CC BY license.<sup>[89]</sup> Copyright 2021, The Authors, Published by American Chemical Society. Optical images of the tested Li symmetrical cells using either the amorphous LLZO-coated SE (f) or the uncoated SE (g). During this plating–stripping test, the current density was increased stepwise from 50 to  $3.2\ \text{mA cm}^{-2}$ . In both (f) and (g), the first panel shows the initial state and the second one shows the result after reaching a current density of  $1.6\ \text{mA cm}^{-2}$ . Reproduced under the terms of the CC BY license.<sup>[91]</sup> Copyright 2021, The Authors, Published by Springer Nature.

characterization are more similar to real batteries than those used in TEM. Therefore, (in situ) SEM is an effective method for studying the evolution of Li dendrites and visualizing Li penetration.

Cheng et al. directly observed the Li dendrites penetration through LLZO SE using SEM and FIB–SEM.<sup>[26]</sup> Figure 8a shows the collected LLZO SE that was harvested from the short-circuited Li|LLZO|Li cell, on which dark macroscopic features

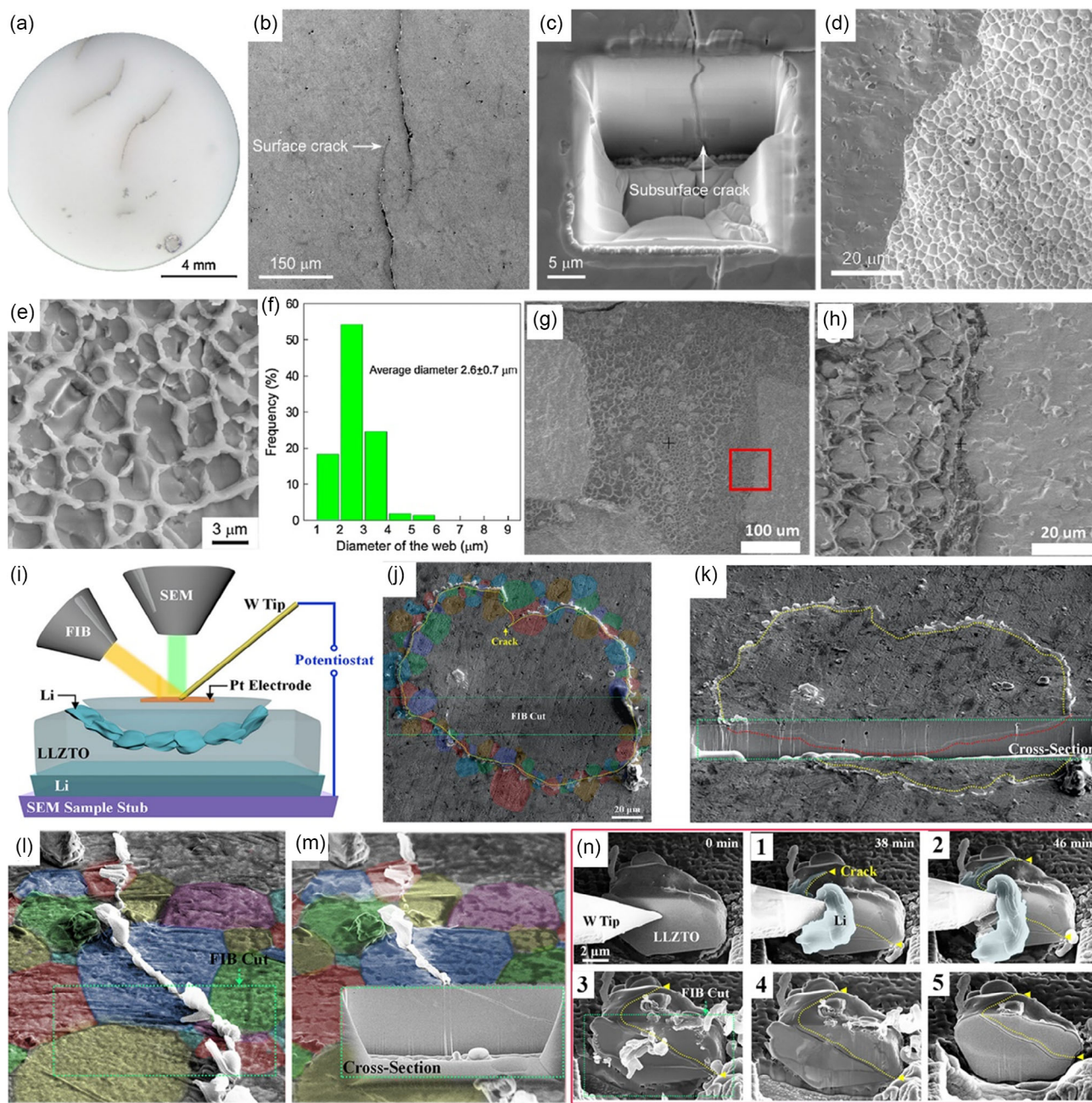


**Figure 8.** a) The cycled LLZO pellet is shown in an optical image with black line features. b) The polished surface of the LLZO pellet is shown in an SEM image with fissures on the surface in contact with Li. c) SEM image of a subsurface fissure excavated by FIB. d) SEM micrograph of a fractured LLZO surface. e) The enlarged SEM micrograph of the web structure in (d). f) The distribution of the average diameter of hexagonal-like features in the web structure. Reproduced with permission.<sup>[26]</sup> Copyright 2017, Elsevier. g) SEM images of Li dendrites grown along the LLZO GBs. h) The enlarged SEM images of the red rectangle in (g). Reproduced with permission.<sup>[94]</sup> Copyright 2021, Elsevier. i) A diagram illustrating the in situ battery testing process, leading to the formation of a bowl-shaped crack. A Pt electrode is placed on the top surface of the LLZTO SE. j) SEM images showing the development of a bowl-shaped crack in the LLZTO SE, with colored grains surrounding the crack line on the LLZTO surface. k) A cross-sectional view of the bowl-shaped crack, where yellow and red dotted lines mark the outline of the crack on the top surface and cross section, respectively. l) SEM image showing the surface cracks and the extruded Li electrodeposits. m) The image taken with FIB-SEM that shows that the transgranular surface crack reached the interior of the LLZTO disk. n) Time-lapse SEM images that demonstrate the initiation and growth of a crack in a single LLZTO grain (panels 1–2), as well as the subsequent slicing of the grain using FIB, which revealed that the crack extended from the top to the bottom of the entire grain. Reproduced with permission.<sup>[96]</sup> Copyright 2021, Wiley-VCH.

were evident. This result was consistent with previous reports.<sup>[92,93]</sup> SEM images clearly showing the geometry and scale of the fissures are depicted in Figure 8b. To determine if the crack features extended below the SE pellet surface, FIB milling was used and the results shown in Figure 8c indicate that the crack feature propagated well below the LLZO pellet surface. The authors then analyzed the cross section of the LLZO pellet using SEM (Figure 8d). A web-like structure was observed on certain regions of the fracture surface, which was further characterized in higher magnification SEM images. Figure 8e displays that the web structure appeared to have hexagonal-like features. The LLZO mainly exhibited transgranular fracture, consistent with the fracture toughness analysis (Section 2.2). Figure 8f shows the diameter distribution statistics of the web structure, with an average diameter of  $\approx 2.6 \pm 0.7 \mu\text{m}$ , similar to the grain size of LLZO ( $\approx 2.8 \pm 0.8 \mu\text{m}$ ). The formation of the web structure seems to be superimposed on the GBs, suggesting that the web structure was formed intergranularly. Based on these results, the authors concluded that Li was plated intergranularly through the LLZO SE GBs. These web- or honeycomb-structured Li dendrites growing along GBs have been also detected recently by Heo et al. using SEM,<sup>[94]</sup> as shown in Figure 8g–h.

Other groups also demonstrated that transgranular growth of Li along the transgranular cracks could occur during Li electro-deposition. After studying the cross section of the short-circuited Li symmetrical cell using  $\text{Li}_{6.55}\text{La}_{2.95}\text{Ca}_{0.05}\text{Ta}_{0.5}\text{O}_{12}$  SE using SEM, Zhang et al. provided direct visual evidence that Li electro-deposition occurred not only along GBs but also along the transgranular crack within the fractured single SE grain.<sup>[95]</sup> In addition, Zhao et al. presented real-time observation of Li deposition in LLZTO SEs at nanometer resolution using FIB–SEM system.<sup>[96]</sup> Figure 8i displays the schematic illustration of the used in situ battery testing system. Figure 8j shows that a closed-loop crack occurred on the LLZTO disk surface after a negative potential was applied to the Pt electrode. Meanwhile, by observing the GB contours, it was noticed that the cracks were primarily transgranular, passing through the grains, rather than intergranular, along the GBs. Additionally, it was observed that Li metal had emerged along the crack line and was extruded out at the surface of LLZTO. To determine the depth of the surface crack, a trench was cut perpendicular to the LLZTO top surface using FIB, and Figure 8k shows that a “bowl-shaped” crack was formed underneath the Pt electrode. Higher magnification cross sections of transgranular cracks are also shown in Figure 8l–m.

The authors further confirmed that cracks can also form and propagate within single-crystal LLZTO grains. In Figure 8n, a single-crystal grain was sliced using FIB milling to expose a flat side surface. When a negative potential was applied to the tungsten (W) tip, a Li dendrite initially grew out under the W tip (panel 1 in Figure 8n). With continued dendrite growth, a slanted crack emerged in the center of the particle and then propagated toward the upper-right direction until the grain broke into two parts (panel 2 in Figure 8n). Consecutive FIB slicing along the side surface showed that the crack crossed through the entire grain (panels 3–5 in Figure 8n). The authors also demonstrated that a crack can cross through two neighboring grains continuously in a multigrained LLZTO particle.

Summarizing the results, the authors suggested that the internal defects, such as voids or GBs, served as the favored hotspots for Li nucleation and the needed electrons were accessible because of the electrical conductivity of LLZTO. Once nucleated, Li electrodeposition was enhanced by the elevated electric field near the Pt electrode, promoting electron flow and causing Li deposition to self-amplify due to the increased electronic conductivity at these sites. Mechanical confinement from the surrounding LLZTO caused continued Li deposition to build up internal pressure, triggering the nucleation of an internal crack through the expansion of a Li-filled defect. The conclusion is in good agreement with a recent study.<sup>[97]</sup> In this study, McConohy et al. statistically investigated the effect of locally applied stress on Li penetration in LLZO via operando SEM. The statistical analysis showed that the probability of Li penetration as a function of Li dendrite diameter followed a Weibull distribution. This suggests that the size dependence is caused by defects that are randomly distributed throughout the sample, providing strong evidence that Li penetration is driven by defects.

The frequently observed scenarios of Li penetration through the GBs have been interpreted in the context of the high electronic conductivity at the GBs. Via using time-resolved operando NDP to monitor the dynamic evolution of Li concentration, Han et al. argued that the high electronic conductivity of the SEs is mostly responsible for Li dendrite formation within the SEs.<sup>[40]</sup> Song et al. found that independently and randomly dispersed Li dendrites were detected in the cycled SE collected from the short-circuited cell, indicating that Li deposition occurs within the SE.<sup>[46]</sup> In contrast, after coating a thin  $\text{LiAlO}_2$  layer on the grain surface of the SE, no short circuits of the cell and no Li dendrites within SE were observed, suggesting that the  $\text{LiAlO}_2$  coating could reduce the electronic conductivity at the GB. Similar studies were also reported by Mo et al., who found that by introducing low electronic conductive  $\text{LiF}$  into the interstitial regions of GBs, Li dendrite growth within the SE is suppressed.<sup>[9]</sup> These results suggest that lowering the GB electronic conductivity seems to be an important avenue to suppress the Li dendrites growth in SEs.

Janek’s group also conducted several in-depth studies of Li dendrites growth on LLZO SE.<sup>[98,99]</sup> Figure 9a shows the in situ SEM experimental setup. They observed vertically grown Li dendrites, as shown in Figure 9b,c. The vertical growth of Li dendrites were also detected by Golozar et al., as shown in Figure 9d–f.<sup>[100]</sup> Consistent with the results from Golozar et al., Janek’s group found that the Li dendrites appeared to form readily on surface heterogeneities. To further study the Li dendrites growth mechanisms, in situ SEM galvanostatic plating experiments using micromanipulators were conducted and the results are shown in Figure 9g–i. It can be noted that at small current density the Li dendrites grew laterally while at high current density, the Li dendrite grew vertically. They therefore concluded that the surface morphology and homogeneity of the SE substrate significantly influenced the nucleation process and, along with the external applied current, determined whether lateral or vertical Li dendrite growth occurred.

Later on, Janek’s group studied the Li electro-deposition kinetics at LLZO surface under different overpotential conditions using both single-crystalline (SC) and polycrystalline LLZO SE.<sup>[99]</sup> Figure 10a shows that lateral Li dendrites grew along



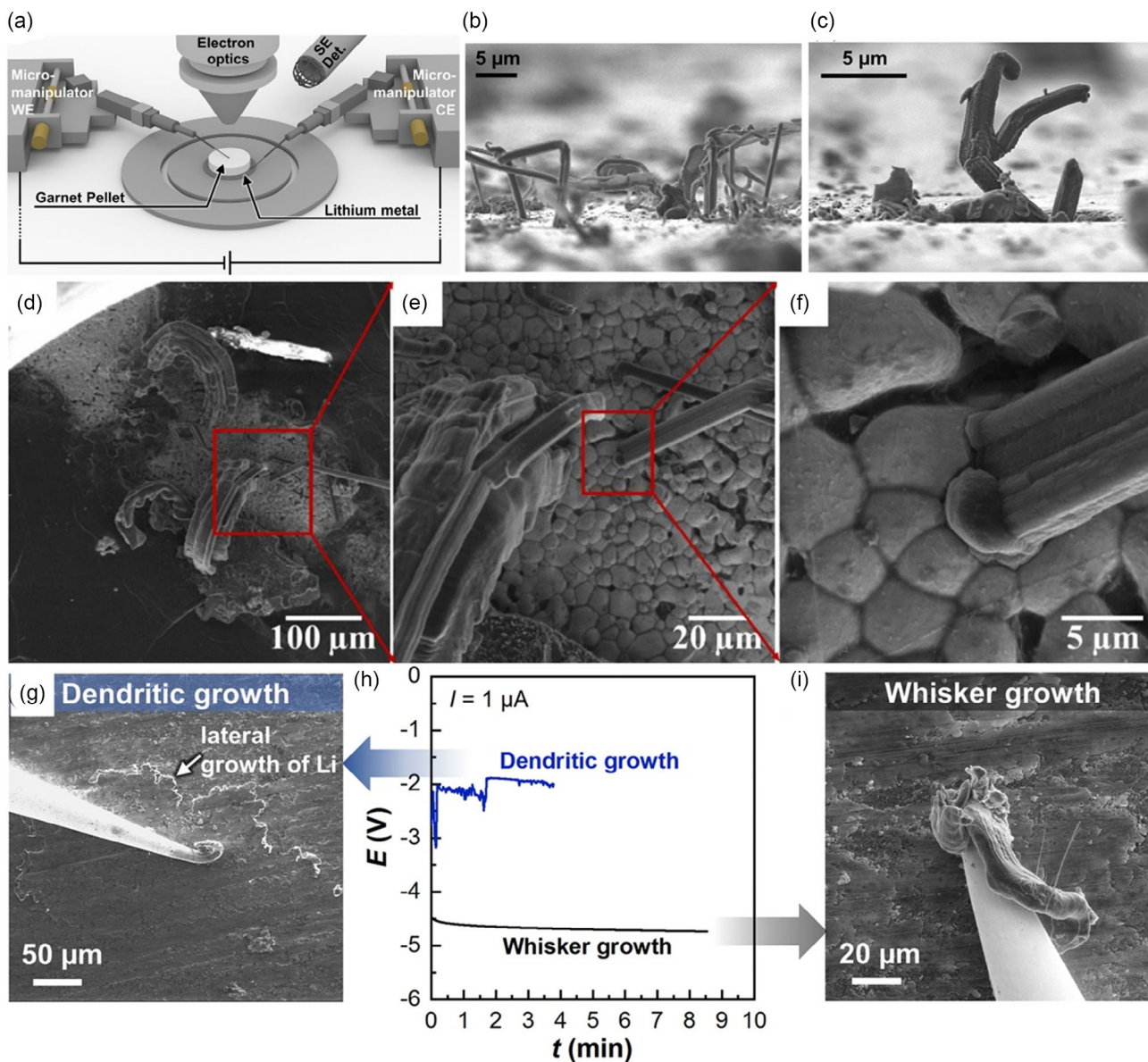


**Figure 9.** a) The diagram of the experimental setup for in situ Li deposition experiments using the microelectrode prober module inside the SEM chamber, with the micromanipulator WE on the LLZO surface and the counter micromanipulator electrode connected to the Li metal. Whisker-like deposits were observed on the SE underneath the copper current collector with b) a diameter of 2  $\mu\text{m}$  and c) a diameter of about 10  $\mu\text{m}$ . d–f) SEM images of the Li surface after cycling, showing dendrite growth initiation from the LLZO surface. Reproduced under the terms of the CC BY license.<sup>[100]</sup> Copyright 2020, The Authors, Published by Springer Nature. g,i) SEM images taken after galvanostatic experiments are shown in (h). h) Potential profile for a galvanostatic dendritic-like and whisker-like Li deposits. (a–c and g–i) Reproduced with permission.<sup>[98]</sup> Copyright 2019, Elsevier.

the SC LLZO surface under high overpotential condition. And the laterally grown Li dendrites could reach the counter electrode, resulting in short-circuit failure. The observed fractal growth pattern suggested a limitation in  $\text{Li}^+$  ion transport within the SE. For fully dense single-grain SE, lateral growth toward the counter electrode appeared to be the primary failure mode leading to short circuits. However, in polycrystalline SE, intergranular and intragranular crack formation close to the micromanipulator tip and crack propagation toward the counter electrode were the dominant failure mode. These results showed that defect

concentration and geometry of polycrystalline pellet surfaces were critical for crack initiation. Additionally, the significant difference in fracture susceptibility between SC and polycrystalline SE further demonstrated the strong influence of microstructure on short-circuiting susceptibility.

Recently, Janek, Dasgupta, Sakamoto, and others conducted an in-depth study of how the physical properties of Li affect the LLZO fracture and Li penetration.<sup>[101]</sup> They conducted complementary studies using both the optical in-plane cell and the in situ SEM cell setup. They first conducted linear sweep

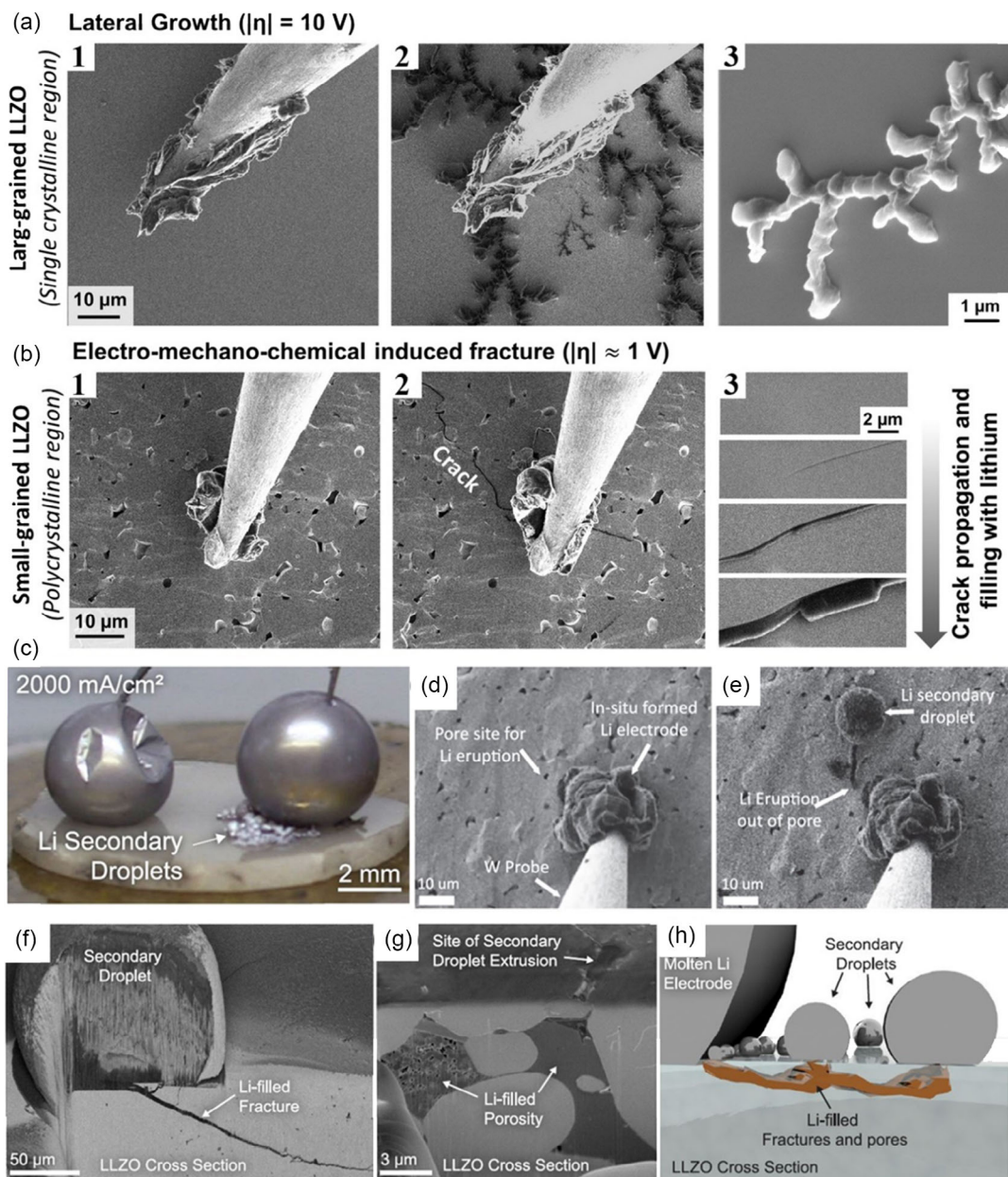


**Figure 10.** a) SEM images of lateral dendritic growth along the SE surface before and after plating at high overpotentials, with an enlarged SEM image shown in panel 3. b) SEM images of electrochemically induced fracture of a polycrystalline LLZO SE, as well as high-resolution images showing immediate filling of the crack with Li shown in panel 3. Reproduced with permission.<sup>[99]</sup> Copyright 2020, Wiley-VCH. c) Optical image of the secondary Li droplets grown during linear sweep amperometry experiment. d) A plating electrode before the appearance of Li secondary droplets, indicating the pore site for eruption. e) The LLZO surface after Li eruption, showing the formation of Li secondary droplets. f) FIB-SEM image showing the site of Li secondary droplet extrusion. g) FIB-SEM etched area showing Li filling pre-existing porosity leading to a Li secondary droplet surface eruption. h) A schematic of the proposed mechanism for Li filament propagation and secondary droplet formation. Reproduced with permission.<sup>[101]</sup> Copyright 2021, Elsevier.

amperometry using in-plane molten Li symmetrical cell. Figure 10c displays secondary Li droplets extruding from the LLZO surface close to the plating electrode. Postmortem FIB-SEM was utilized to study these droplets. Cross-sectional imaging in Figure 10f shows that the source of the secondary droplets was a crack in the underlying LLZO, through which molten Li was extruded. Additionally, cracks observed on the LLZO

top surface indicated the locations of the secondary Li droplets (Figure 10g). The Li dendrites propagation and secondary droplet formation mechanism were proposed in Figure 10h.

To complement the OM results, the authors conducted in operando SEM using porous Al-doped LLZO (Figure 10d–e). Figure 10e clearly displays that Li secondary droplet could be formed from the pore highlighted in Figure 10d during the

galvanostatic plating using molten Li|LLZO cell. Although the Li secondary droplet was present, there was no visible evidence of significant surface cracking, as seen in the optical results. This suggests that molten Li can flow stably through micrometer-wide or smaller open channels without or with minimal cracking if the porosity is high. It is noteworthy that the formation of the Li secondary droplets of the preferred spherical form was attributed to the reduced surface energy. Aiming to understand how propagation of molten and solid Li differed, they conducted another test using solid Li. The study found that unlike molten Li, solid Li dendrites were observed to emerge from the LLZO surface, rather than droplets. Additionally, cracks in multiple directions were observed, differing from the results obtained using molten Li. These results suggest that due to the higher viscosity of solid Li, solid Li cells were less able to relieve pressure within cracks by surface extrusion and therefore had a higher degree of vertical Li dendrites growth than molten Li cells. This study indicates that the mechanical properties of Li, such as viscosity, play an important role in determining the propagation of Li dendrites and that switching from molten to solid Li has a significant impact on the failure mode of the cell.

Very recently, Zhu et al. reported an in-depth investigation of the Li dendrites nucleation and growth behaviors at LLZO GBs using in operando microscopy technique.<sup>[102]</sup> First, they conducted Kelvin probe force microscopy measurements at the Li|SE interface and a decrease in the contact potential difference at GBs during Li plating was observed. They attributed this decrease to the different electron transport properties in GBs compared to the grain bulk. Second, they conducted in operando microscopy study using the electron beam-induced alkali metal growth method. As schematically shown in **Figure 11a**, the accumulation of electrons in/on the irradiated SE would cause sufficient overpotential to induce  $\text{Li}^+$  ions reduction. The results shown in **Figure 11b** clearly demonstrate that Li expulsions grow with increasing electron-beam irradiation time. These results also display that the expulsions possess larger diameter at GBs than the ones inside the grains. To exclude the potential effects from locally different chemical compositions, the authors also studied a larger scale region containing 20–30 different grains, as shown in **Figure 11c**. Similar results were observed after electron-beam irradiation, as shown in **Figure 11d**. **Figure 11e–f** shows the images taken using the backscattered electron signals, distinguishing the dark Li expulsions from the white LLZO SE.

The authors proposed a model to explain the formation and growth mechanisms of Li metal at GBs on LLZO surface under a biased electric field condition, as shown in **Figure 11g**. During the electron irradiation, the emitted electrons preferentially accumulate at the GBs due to their different electrochemical properties compared to the in-grain areas. The higher electron concentration at GBs then leads to a higher electron concentration gradient from GBs to their adjacent regions, generating an electric field that attracts  $\text{Li}^+$  ions. With continued electron irradiation, the gathered  $\text{Li}^+$  ions are easily reduced to Li metal once a sufficient negative potential is reached. With an increasing amount of reduced Li, mechanical strain builds up at GBs, causing the extrusion of Li from the LLZO surface. These results clearly indicate that GBs play an important role in Li nucleation and growth.

SEM was also used to study the Li penetration behavior in sulfide SEs. Nago et al. conducted in situ SEM observation of Li deposition using the LSP SE.<sup>[103]</sup> **Figure 12a** shows the schematic of the used cell with the tilt of the stage at 30 degrees for better observation. **Figure 12b–d** shows the recorded SEM images during battery operation. **Figure 12b** shows that the SE layer possessed a very flat surface before Li deposition. **Figure 12c** displays the occurrence of several cracks locally, as indicated by the dotted circles, prior to the short circuit of the cell. The Li that grew from the SE layer toward the stainless steel (SS) was observed after the short circuit (**Figure 12d**). Following this, electrochemical tests were performed at a very high current density after the short circuit of the cell, and the results are presented in **Figure 12e–f**. **Figure 12e** displays Li pillars that were observed in the large cracks on the surface of the SE layer. **Figure 12f** shows that Li pillars grew slightly during Li deposition at  $5 \text{ mA cm}^{-2}$  for 10 min, indicating that Li extends from the interior of the SE layer. Kim et al. also conducted in situ SEM observation of Li deposition in sulfide SE and Li dendrites were observed at the Li|SE interface.<sup>[35]</sup>

Chiang's group<sup>[29]</sup> used SEM to record images of Li penetrated  $\beta\text{-L}_3\text{PS}_4$  SE using secondary electrons (**Figure 12g,h,j**) and backscattered electrons (**Figure 12i**). It has to be noted that the samples in **Figure 12g–i** experienced air exposure while the sample in **Figure 12j** did not. The elongated filaments that had a narrowed tip where they had separated from the opposing surface had the fracture characteristic of a ductile phase, which is the Li metal phase. This conclusion was supported by a comparison between the secondary electron images and the backscattered electron image, which showed that the phase corresponding to the ductile fracture had very low backscattered electron contrast, consistent with Li metal. These findings suggest that the electrodeposited Li propagated in a cellular manner, along pore channels, GBs, or both, similar to Li penetration through Al-doped LLZO.<sup>[26]</sup>

### 3.3. Characterizations Using (Synchrotron) XCT

To gain a comprehensive understanding of the formation and growth mechanisms of Li dendrites, it would be beneficial to evaluate their 3D morphology. However, previous studies have primarily provided 1D or 2D information about Li dendrites buried inside SEs, making it difficult to fully comprehend their complex 3D structure. Furthermore, in order to expose the internal cross sections of the SE, it is often necessary to break the SE, which can alter the Li dendrites at the testing surfaces. In this regard, nondestructive 3D visualization using X-CT is suited for battery research that can detect the internal structure evolution of electrodes.<sup>[80,104–109]</sup> Due to its nondestructive nature, X-ray imaging offers unparalleled capabilities for exploring the evolution of Li dendrites in response to various cycling conditions. In this section, the application of XCT to understand Li penetration through SEs is detailed.

Seitzman et al. conducted 3D visualization of Li migration in LPS SE using nondestructive SXCT as well as the FIB–SEM.<sup>[110]</sup> **Figure 13a** shows the specialized sample holder for this study and **Figure 13b** shows the in operando characterization results of the Li|LPS|Li symmetrical cells during battery cycling. In **Figure 13b**, panel 0 cycles represents the battery's uncycled state,

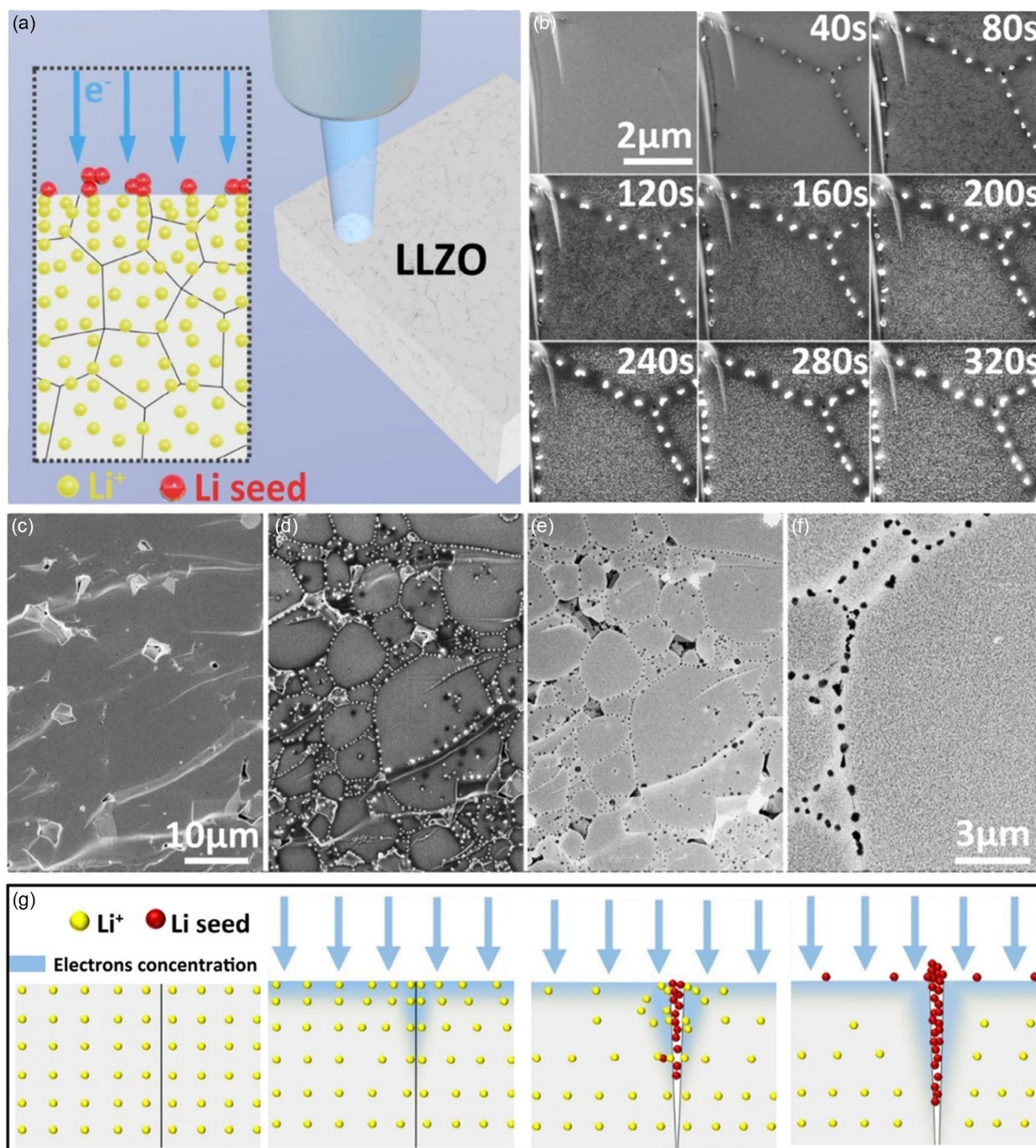


**Figure 11.** a) Schematic showing the electron injection causing a reduction of  $\text{Li}^+$  ions in LLZO to Li metal. b) Morphological evolution of Li particles during the in operando electron-beam irradiation. The LLZO morphology reordered on a large scale that is c) before and d) after electron-beam irradiation for 400 s. This region is measured using either c,d) a secondary electron detection mode or e) a backscattering electron detection mode. f) The enlarged view of (e). g) The schematic illustration of the formation of Li metal on LLZO surface during electron-beam irradiation. Reproduced under the terms of the CC BY license.<sup>[102]</sup> Copyright 2023, The Authors, Published by Springer Nature.

where dark (poorly X-ray absorbing) lines indicate the boundaries between adjacent LPS grains. After one cycle, most of the line features widened (panel 1 cycle in Figure 13b). With more cycles,

the dark line features widened significantly and multiple LPS grain structures were disrupted with dark features (indicated by the marked lines in the images). This suggests that the

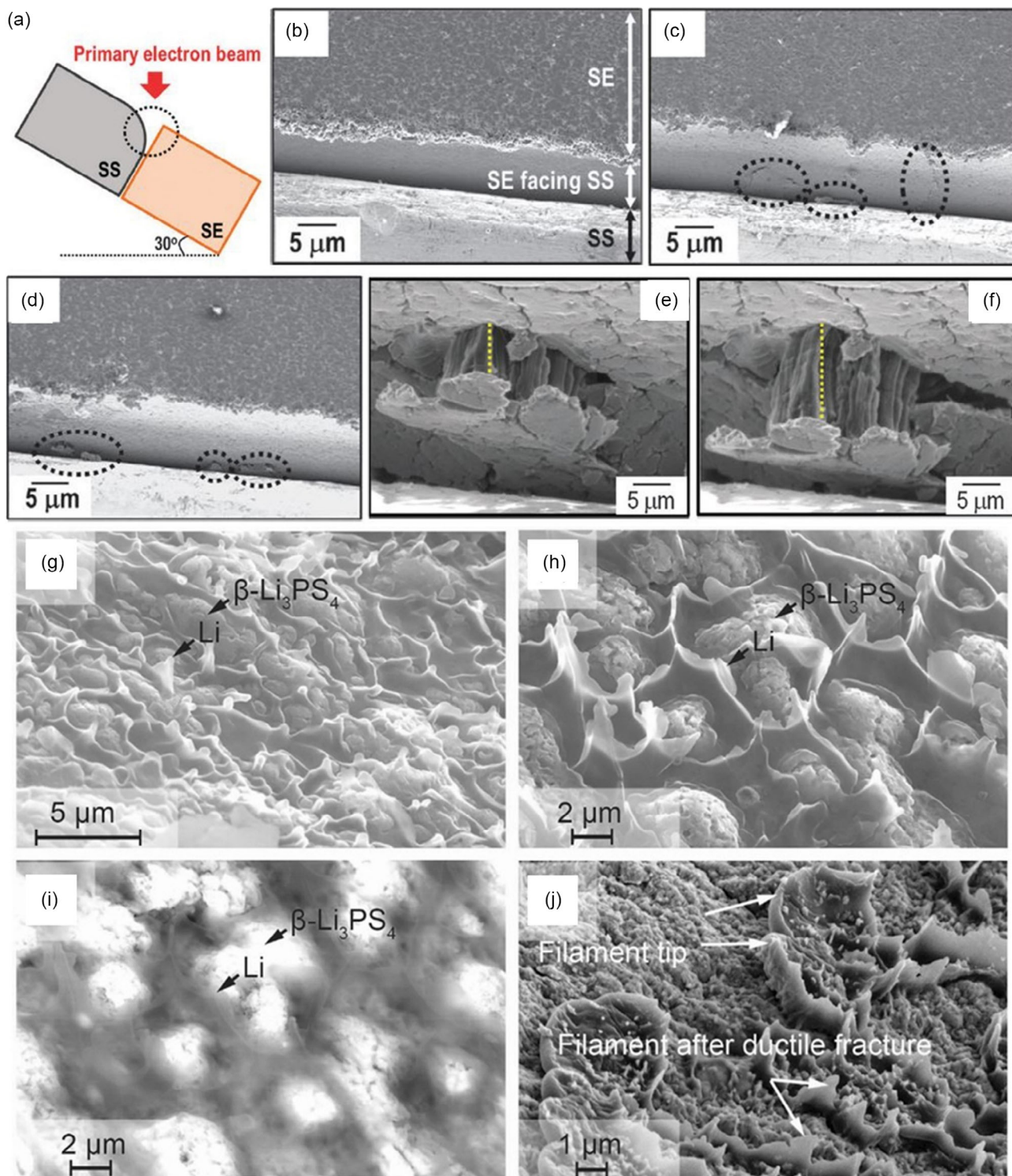


**Figure 12.** a) A schematic of the SSLB cell used for in situ SEM observation with a tilt of the stage at 30 degrees. SEM images of the interface between the SE layer and SS at different positions of the same cell b) before and c) after Li deposition for 600 s and d) 1920 s during Li deposition. SEM images of the interface between the SE and SS at the same position in the same cell e) immediately after the short circuit of the cell and f) Li deposition at  $5 \text{ mA cm}^{-2}$  for 10 min after the short circuit. Reproduced with permission.<sup>[103]</sup> Copyright 2013, Royal Society of Chemistry. SEM images of the fractured polycrystalline  $\beta\text{-Li}_3\text{PS}_4$  SE into which Li has been electrodeposited: g,h,i) show secondary electron images of the fracture surface, while i) shows backscattered electron images of the same surface. The samples in (g) and (h) were exposed to air for less than 1 min, while the sample in (j) was transported in a vacuum-operated transfer box. Reproduced with permission.<sup>[29]</sup> Copyright 2017, Wiley-VCH.

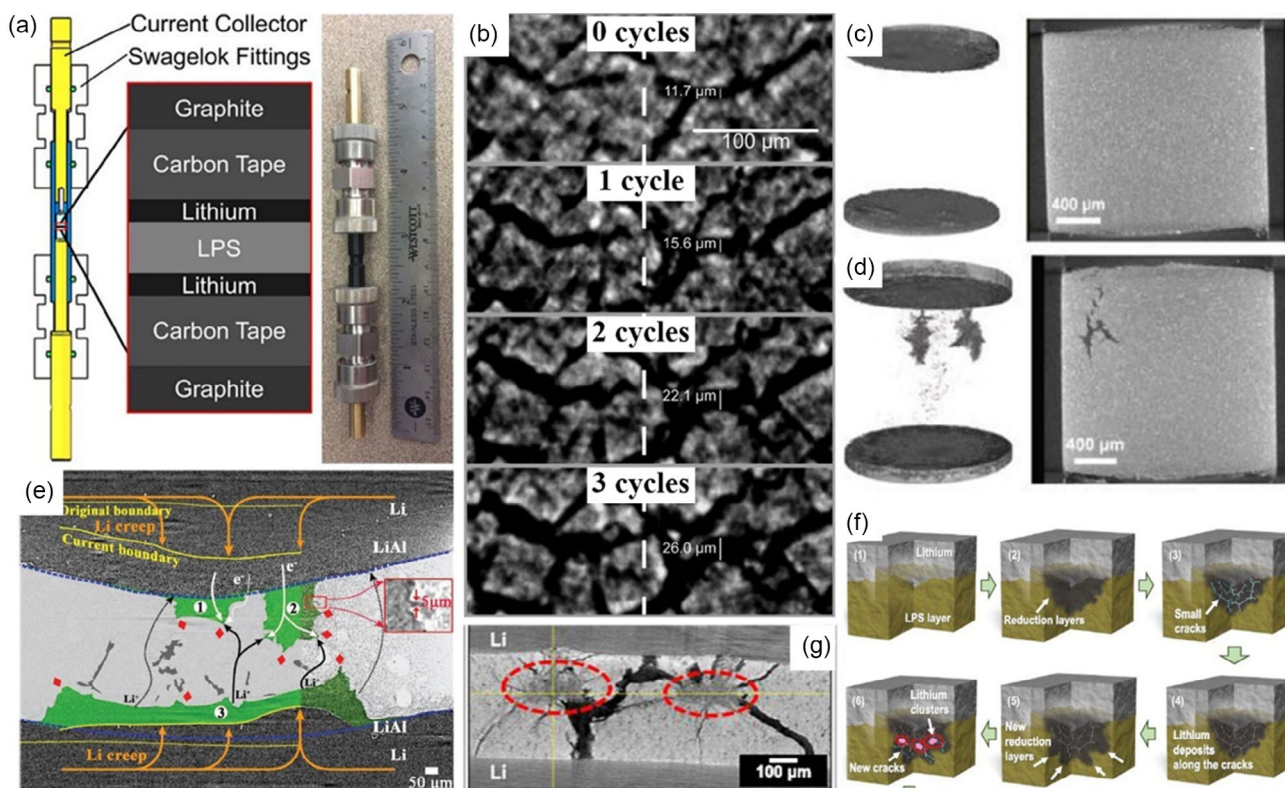


**Figure 13.** a) Schematic and image of the used in situ Li|LPS|Li cell for SXCT. b) Reconstructed and threshold images of the same region of the cell after successive cycles during tomography analysis. Reproduced with permission.<sup>[110]</sup> Copyright 2018, IOP Publishing. 3D rendering and 2D image of the studied Li|LPS|Li cell c) before and d) after shorting. The tomography images confirm that no Li is present in the electrolyte before the cell shorts. After shorting, several additional phases are detected inside the SE. Tomography results show that a large quantity of low-density dendrites has been formed in the SE. Reproduced with permission.<sup>[111]</sup> Copyright 2020, Wiley-VCH. e) The cross section of the studied Li symmetrical cell using LPS SE after cell shorting. This image shows clearly the deformation of the SE as well as the Li creep after cell shorting. Reproduced with permission.<sup>[48]</sup> Copyright 2022, Wiley-VCH. f) Proposed crack formation mechanisms initiated at Li|LPS interface during Li plating. g) Selected tomogram of the Li|LPS|Li cell after short-circuiting, where red circles indicate low density areas, e.g., Li clusters. Reproduced with permission.<sup>[114]</sup> Copyright 2021, American Chemical Society.

increase in line feature width with increasing number of cycles was likely due to highly mobile Li atoms being forced into the LPS region. Once the void space was occupied, continued Li growth could damage the LPS grain. Besides, Doux et al. also observed using the XCT that a great deal of Li dendrite structures were formed in the short-circuited Li|LPS|Li cell, as shown in Figure 13c–d.<sup>[111]</sup> They concluded that the ductility of Li (low stress yield) allowed it to creep through the SE's pores, GBs, etc. to trigger potential short circuit during battery cycling.

The crack formation and propagation inside SEs can be triggered by the (electro)chemical side reactions between Li and SEs. Using in situ 3D SXCT technique, McDowell's group first demonstrated that the growth of an interphase at the Li|Li<sub>1+x</sub>Al<sub>x</sub>G<sub>2-x</sub>(PO<sub>4</sub>)<sub>3</sub> (LAGP) interface drove fracture of the LAGP SE, and the degree of fracture that occurred during cycling was discovered to be the main reason for the rise in impedance and eventual failure of the battery.<sup>[112]</sup> Later on, the same group conducted an in-depth study of the Li|LPS interface during battery cycling using SXCT and they revealed that the cell behavior was determined by the complex interaction between void

formation, interphase growth, and volumetric changes.<sup>[113]</sup> Sun et al. also demonstrated that the complicated (electro)chemical reactions at Li|LPS interface could not only mechanically degrade the SE materials but also affect the direction of SE strain and Li creep, as clearly shown in Figure 13e.<sup>[48]</sup> Very recently, Otoyama et al. summarized the (electro)chemically induced crack formation in LPS SE at the Li|LPS interface, as shown in Figure 13f.<sup>[114]</sup> From panel 1 to panel 2 in Figure 13f, LPS initially decomposed to Li<sub>2</sub>S and Li<sub>3</sub>P, forming an interphase layer that is shaded darker gray in panel 2. Further battery cycling accelerated the (electro)chemical reaction, causing continuous accumulation of the interphase at Li|LPS interface. As a result of this (electro)chemical decomposition reaction, small cracks, which are highlighted in blue, formed in the reduction layer due to volume expansion. Li was then deposited along these cracks in the interphase layer, as depicted in panel 4. Subsequently, as shown in panel 5, new reduction layers and new small cracks were generated within the LPS layer. Li clusters, which are shaded pink, formed in the cracks. The continuous Li deposition along the large cracks led to short-circuiting of the cells. Figure 13g is a representative cross section of the

short-circuited Li|LPS|Li cell with red circles indicating Li electrodeposits.

For the electrochemically stable SEs, Hatzell's group argued that the microstructure of the SE, e.g., the pore connectivity, pore distribution, and SE tortuosity, played an important role in Li penetration phenomenon. The authors tracked structural changes in LLZO SE processed at three different temperatures (1050, 1100, and 1150 °C) using SXCT before and after short-circuiting.<sup>[27]</sup> Material characterizations revealed that as the sintering temperature increased, the relative density and the ionic conductivity of the SE also increased. However, the interconnected pathway between pores also increased, as shown in **Figure 14a–c**. After analyzing the results after short-circuiting, as depicted in Figure 14a–c, they inferred that the increased pore connectivity and higher ionic conductivity facilitated Li transport and dendrite growth within the SE sintered at 1150 °C. Additionally, they discovered that the tortuosity and the tortuosity directional anisotropy, both of which increased with sintering temperature, were also crucial factors impacting the battery performance.<sup>[115]</sup> As shown in Figure 14d, the SE samples sintered at 1150 °C exhibited a significant anisotropic Li<sup>+</sup> ions flux distribution. The higher tortuosity of this SE material led to a tremendous change in the local concentration of Li<sup>+</sup> ions, resulting in

significant concentration and polarization gradients at the edges of the pore structures. Combined with the presence of excess electrons on pore surfaces,<sup>[116]</sup> these results suggest that the strong Li<sup>+</sup> ions concentration gradients arising from nonuniform mass transport can initiate Li deposition into the pores.

Indeed, the direct Li deposition inside SEs was also reported by others using SXCT. In a recent study, Seitzman et al. utilized in operando SXCT to visually study the behavior of Li in response to stack pressure, porosity effect, and different operating temperatures.<sup>[117]</sup> The illustration in Figure 14e suggests that cells with different particle sizes undergo a competition between the previously observed Griffith flaw mechanism and other behaviors, such as the reduction of Li<sup>+</sup> into Li metal due to imperfect electronic insulation. This is because an increase in temperature enhances both electronic and ionic conductivity, accelerating the likelihood of Li<sup>+</sup> ions encountering electrons and depositing as Li metal within the SE rather than at the anode. Thus, a shift from the Griffith flaw mechanism describing Li migration through defects in a Li symmetrical cell to a mechanism in which Li deposits within the bulk of the SE is proposed. Zheng et al. also observed the Li deposition within the SE after full-cell cycling using SXCT.<sup>[118]</sup> Figure 14f–g compares the sectional views of the SXCT data of the uncycled NCM|Li-0 cell and the

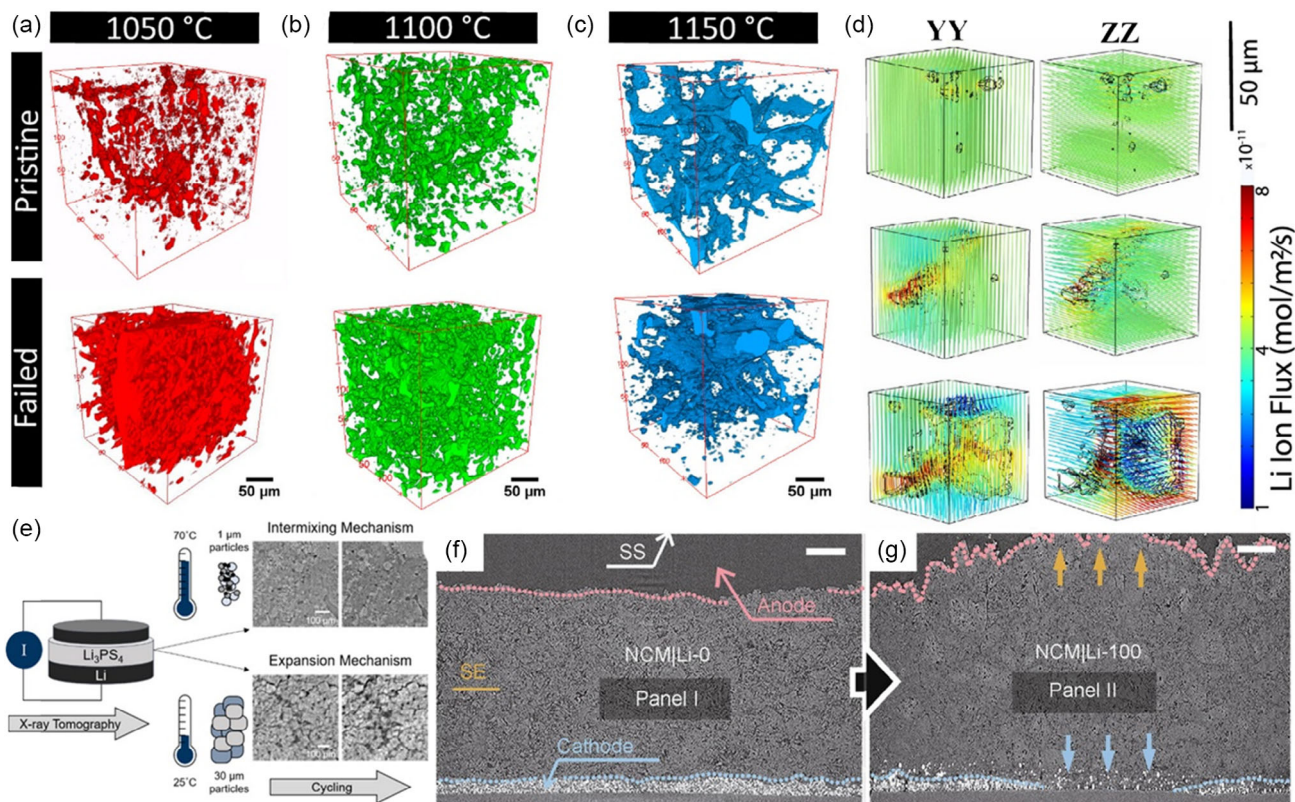


**Figure 14.** Images of the void phase within the interior of LLZO SEs sintered at a) 1050, b) 1100, and c) 1150 °C obtained from the X-ray tomographic reconstructions. Reproduced with permission.<sup>[27]</sup> Copyright 2018, American Chemical Society. d) Li<sup>+</sup> ions flux streamlines along the YY and ZZ axes for microstructural domains of real LLZO SE sintered at 1050 (first arrow), 1100 (second arrow), and 1150 °C (third arrow). Reproduced with permission.<sup>[115]</sup> Copyright 2019, American Chemical Society. e) SXCT results of the response behavior of Li under different conditions of stack pressure, temperature, and SE particle size. Reproduced with permission.<sup>[117]</sup> Copyright 2021, American Chemical Society. SXCT characterization results of f) the uncycled and g) the 100-cycles cycled NCM|Li cells. The yellow and blue arrows in panel II point out the changes that occurred at the anode and cathode sides, respectively. All scale bars are 200 μm. Reproduced with permission.<sup>[118]</sup> Copyright 2023, Elsevier.

100-cycled NCM|Li-100 cell. One can obviously note that some part of Li was disappeared and the LPSCl SE was found to reach the SS collector (yellow arrow in Figure 14g), in addition to the decreased thickness of Li anode. In-depth investigation of the grayscale value changes inside the selected four regions near Li|SE interface suggested that the SE region became low X-ray absorbing compared with the uncycled state. Together with the line profile analysis in other regions, the authors concluded that during Li plating, Li was preferentially deposited within the SE (e.g., along the SE GBs) near Li anode. This scenario can perfectly explain the diminished Li bulk at Li anode as well as the swelled SE.

Recently, Hatzell's group studied the fracture behaviors in LPS SEs using SXCT as well as TEM.<sup>[119]</sup> They found that, despite differences in microstructure and interphase properties, all the LPS samples (amorphous sulfide SE, A-LPS; a mixture of amorphous LPS and LiI salt, LPS:0.5LiI, mechanical milling of the LPS:0.5LiI, LiI-AT, annealing the LiI-AT, LiI-AN) showed the same fracture initiation and propagation mechanisms, as shown in Figure 15. Figure 15a displays the pristine state of the sample. After an initial edge-chipping at the Li|SE interface (Figure 15b), a lateral crack developed and grew through the thickness of the sample (Figure 15c). As a result, two failure modes were identified: 1) edge-chipping failure at the electrode|electrolyte interface and 2) vertical crack growth through sample thickness originating from the edge-chip. The authors argued that, due to the

potential stress concentration, surface irregularities were the preferential regions through which fracture can initiate. The metal flow through this surface-driven crack propagated the fracture through the thickness of the electrolyte leading to ultimate failure by shorting. This is schematically shown in Figure 15d.

The authors also investigated the influence of SE microstructure heterogeneity on crack initiation and propagation behavior. They found that crack growth was determined by the mechanics of the bulk electrolyte and would tend to occur in regions with higher porosity due to lower local yield and fracture strength. Higher porosity also increased local tortuosity, resulting in increased current density and electric field in the area, leading to crack formation in regions with high microstructural heterogeneity. The authors concluded that controlling porosity and pore distribution within the SE pellet is crucial for optimizing SSLB performance.

Shearing's group conducted a study on the Li penetration phenomenon inside short-circuited LLZO SE using nano-CT, and they concluded that the pre-existing pores in the SE, which are a result of the fabrication process, do not significantly influence the growth path of cracks.<sup>[120]</sup> Figure 16a shows a virtual slice extracted from a plane showing long cracks growing through the pillar sample, along with a pore at the juncture of several GBs. Figure 16c displays a line profile of the grayscale corresponding to the red line shown in Figure 16b. It is based on the difference in grayscale values, Li, voids and LLZTO were

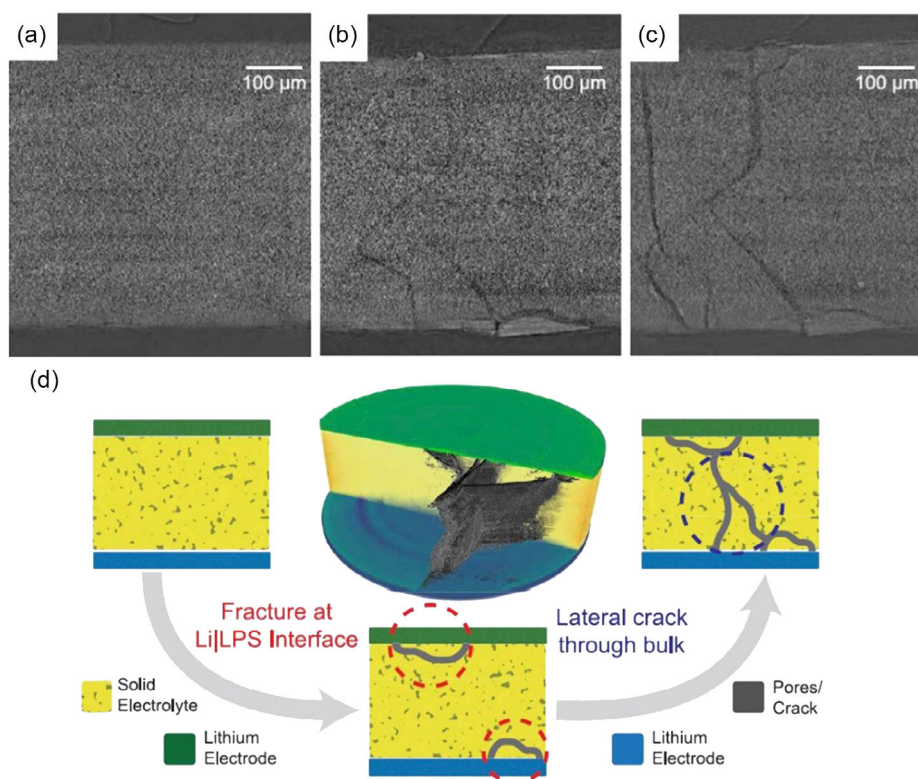


**Figure 15.** Sectional images of the Li symmetrical cell using the thiophosphate LPS SE showing different phenomenological fracture mechanisms: a) pristine, b) chipping failure, and c) lateral crack growth. d) The diagram shows the failure onset and growth mechanisms in LPS SE. Reproduced with permission.<sup>[119]</sup> Copyright 2020, Elsevier.



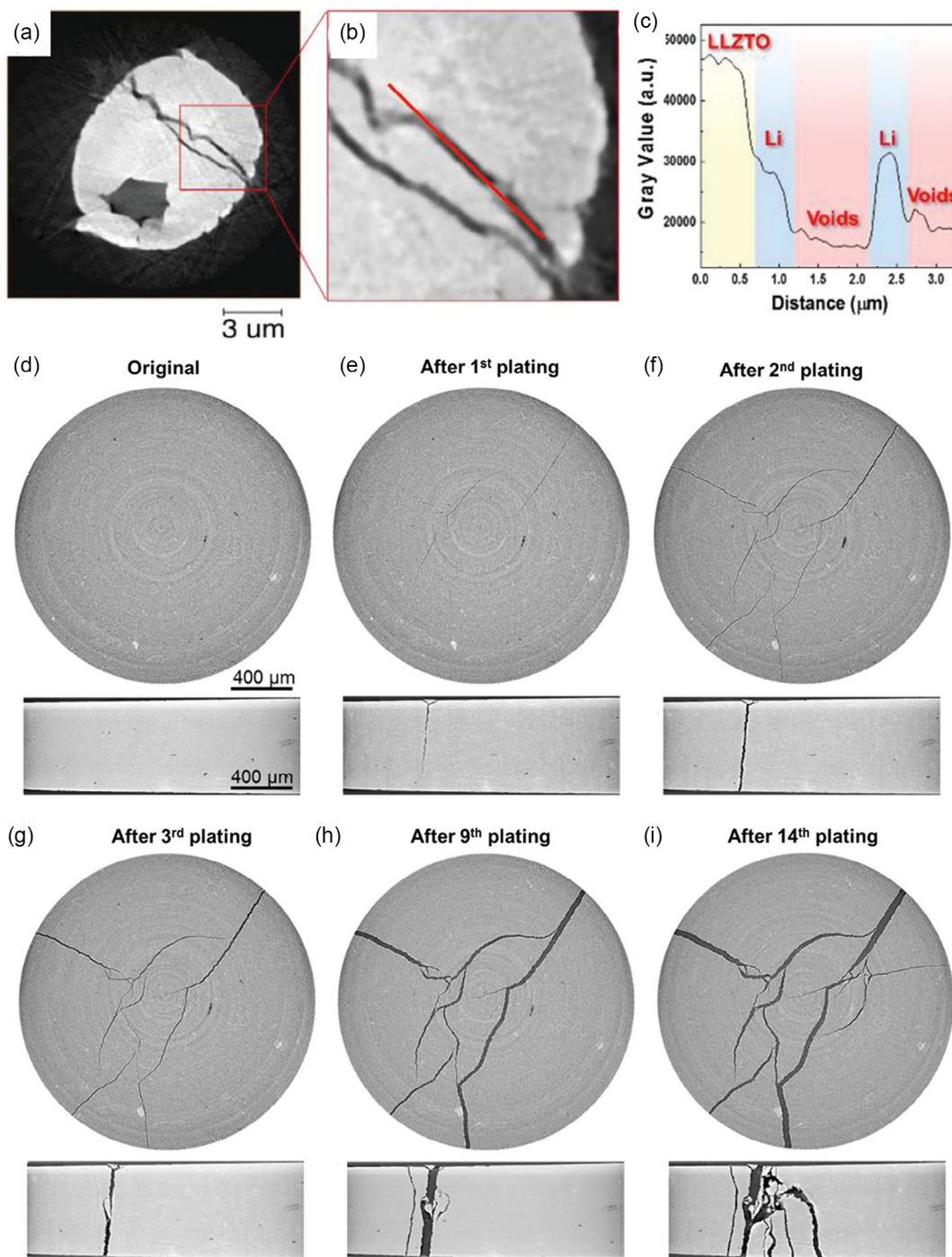


**Figure 16.** a) A grayscale slice was extracted from a plane perpendicular to the sample pillar axis. b) A partial enlargement of the grayscale slice in (a). c) The line profile of the grayscale corresponding to the red line marked in (b). Reproduced with permission.<sup>[120]</sup> Copyright 2020, Wiley-VCH. The selected 2D orthogonal slices extracted from the 3D tomograms of the studied LPS SE pellet subjected to different states: d) original state, e) after the 1st, f) 2nd, g) 3rd, h) 9th, and i) 14th plating. Reproduced with permission.<sup>[121]</sup> Copyright 2021, Elsevier.

segmented. After examining the 3D distribution of the crack, Li dendrites as well as the LLZTO phase, the authors found that although the Li dendrites bifurcate in some places, overall, they form a thin wavy and rippled plane. This rippled plane shape

was largely determined by the geometry of the LLZTO GBs. They concluded that the grain structure largely controlled the crack shape, which, in turn, influenced the Li dendrites distribution. Additionally, they found that long cracks propagated

besides pre-existing pores, rather than through them. This crack propagation path suggests that pre-existing pores in the microstructure, at least in the field of view here, did not significantly influence the growth path of cracks and Li dendrites.

In another study, Shearing's group tracked the Li penetration in LPS SE in 3D using the in situ SXCT.<sup>[121]</sup> The SXCT results recording the crack initiation and Li dendrites growth inside SE are shown in Figure 16d–i. In Figure 16d, the original LPS pellet is shown to be intact without any detectable cracks. After the first plating, some narrow cracks appeared at the Li|LPS interface, but they had not yet penetrated through the LPS (Figure 16e). With two plating steps, the cracks propagated in both lateral and vertical orientations, reaching the edge and cathode side of the pellet (Figure 16f). As more Li was plated in the following steps until short circuit, the cracks widened and grew into new branches, as shown in Figure 16g–i. The 3D structures of the evolved cracks as a function of plating were also examined. The authors found that the volume of cracks was only similar to the volume of deposited Li after the first plating, and in subsequent plating steps, the crack volume increased at a much faster rate than the Li volume. This suggests that cracks were only partially filled with Li and contained a significant amount of empty space inside. Hence, the authors suggest that the reason why the battery did not short-circuit immediately when cracks penetrated through the LPS pellet was due to the partially filled cracks.

These results are consistent with those from Bruce's group.<sup>[122]</sup> They used in situ SXCT and spatially mapped XRD to track the growth of cracks and Li dendrites in Li|LPSCl|Li cells as a function of charge passed. Specifically, they found that on plating, cracking initiated with spallation near the surface at the Li electrode edges where local fields were enhanced. The transverse cracks that were originated from the spallation and extended across the SE advance from the plated electrode to the stripped electrode. The Li ingress propelled the propagation of the spallation and transverse cracks by expanding the crack from the backside, resulting in cracks traversing the entire electrolyte before Li arrived at the other electrode. Very recently, they further showed that initiation and propagation were separated activities using SXCT.<sup>[123]</sup> Initiation was caused by Li deposition into subsurface pores, facilitated by microcracks that connected the pores to the surface. Upon further charging, the pressure in the pores increased due to the slow extrusion of Li back to the surface, causing cracks to form. In contrast, dendrite propagation was caused by the opening of a wedge, with Li driving the dry crack from the back, not the tip. These results indicate that the initiation was influenced by the local fracture strength at the GBs, pore size, pore population density, and current density, whereas propagation was affected by the macroscopic fracture toughness of the ceramic, the length of Li dendrites that partially occupied the dry crack, current density, stack pressure, and the charge capacity accessed during each cycle. Based on these findings, inhibiting dendrite penetration can be achieved by either suppressing initiation or propagation. Suppression of initiation can be accomplished by enhancing local fracture strength, minimizing pore size, and controlling pore proximity. Meanwhile, suppressing propagation can be achieved by maximizing electrolyte fracture toughness and minimizing pressure on the Li anode.

### 3.4. Characterizations Using TEM

Although the nondestructive and 3D SXCT can track the Li dendrites evolution and crack formation in 3D at higher resolutions than the OM, it is not sufficient to resolve the structural changes at GBs and individual grains. Additionally, it is difficult to understand the morphological transformations that occur during electrochemical cycling at nanoscale because there are few non-destructive techniques available for investigating local dynamics at these interfaces. In this retrospect, TEM with a resolution at atomic level, which is much higher than the abovementioned probing techniques, is helpful to clarify the Li penetration phenomena.

Recently, both Wang's group<sup>[124]</sup> and Huang's group<sup>[125]</sup> studied the Li dendrites formation and growth mechanisms using an in situ AFM–environmental transmission electron microscopy system. They both directly captured the Li dendrites growing from the spherical Li nucleation. By taking advantage of the AFM cantilever with an appropriate spring constant, they could not only study the mechanical properties of the grown Li dendrites (e.g., yield strength, Young's modulus) but also investigate the Li dendrites growth behavior under mechanical constraints. Huang's group later reported the in situ observation of Li deposits electrochemically deposited under a CO<sub>2</sub> atmosphere using an environmental TEM, and they discovered that the shape of the Li deposits was significantly affected by the balance between cracking and self-healing of the solid electrolyte interphase (SEI).<sup>[126]</sup> Figure 17a shows that as Li plating proceeded at low applied voltage (−0.3 V, panels 0 and 21 s in Figure 17a), the Li sphere increased in diameter from 200 to 400 nm and the thickness of the SEI shell increased from 5 to 9 nm (the LiCO<sub>3</sub> SEI shell exhibited darker contrast than the Li core). However, under a higher potential (−1.0 V), panels 42 to 367 s in Figure 17a show that the Li sphere started to elongate in the vertical direction (the yellow arrow in panels 192 s in Figure 17a). The upright growth of the Li sphere in Figure 17a resulted in a long and straight Li dendrite with a consistent cross-sectional width. This behavior was attributed to the 3D ring crack in the SEI shell located at the bottom of the Li sphere (yellow arrowheads in Panel 192 s in Figure 17a). This finding shows that when high voltages are applied, Li deposition outpaces the self-healing of SEI cracks, resulting in the directional growth of Li whiskers. Conversely, when low voltages are applied, SEI crack self-healing is fast enough to allow for isotropic growth of Li spheres.

Huang's group also studied the Li deposition-induced fracture of carbon nanotubes<sup>[127]</sup> and damage of LLZTO SE<sup>[128]</sup> during Li plating using TEM. Figure 17b illustrates that the deposition process began at the center of the carbon nanotube (CNT), where a nanoparticle was located. Initially, both Li deposition growth fronts advanced forward during the Li deposition process. The front that was farthest away from the SE (referred to as the far front) stopped growing after a specific amount of Li deposition, while the front that was closest to the SE (the near front) continued growing until it reached the SE at 203 s. Additional Li deposition was limited by the SE, the far front, and the CNT. At 217 s, a bump appeared on the left wall of the CNT, closer to the near front (indicated by a white arrow in panel 217 of Figure 17b). This bump grew until the wall of the CNT

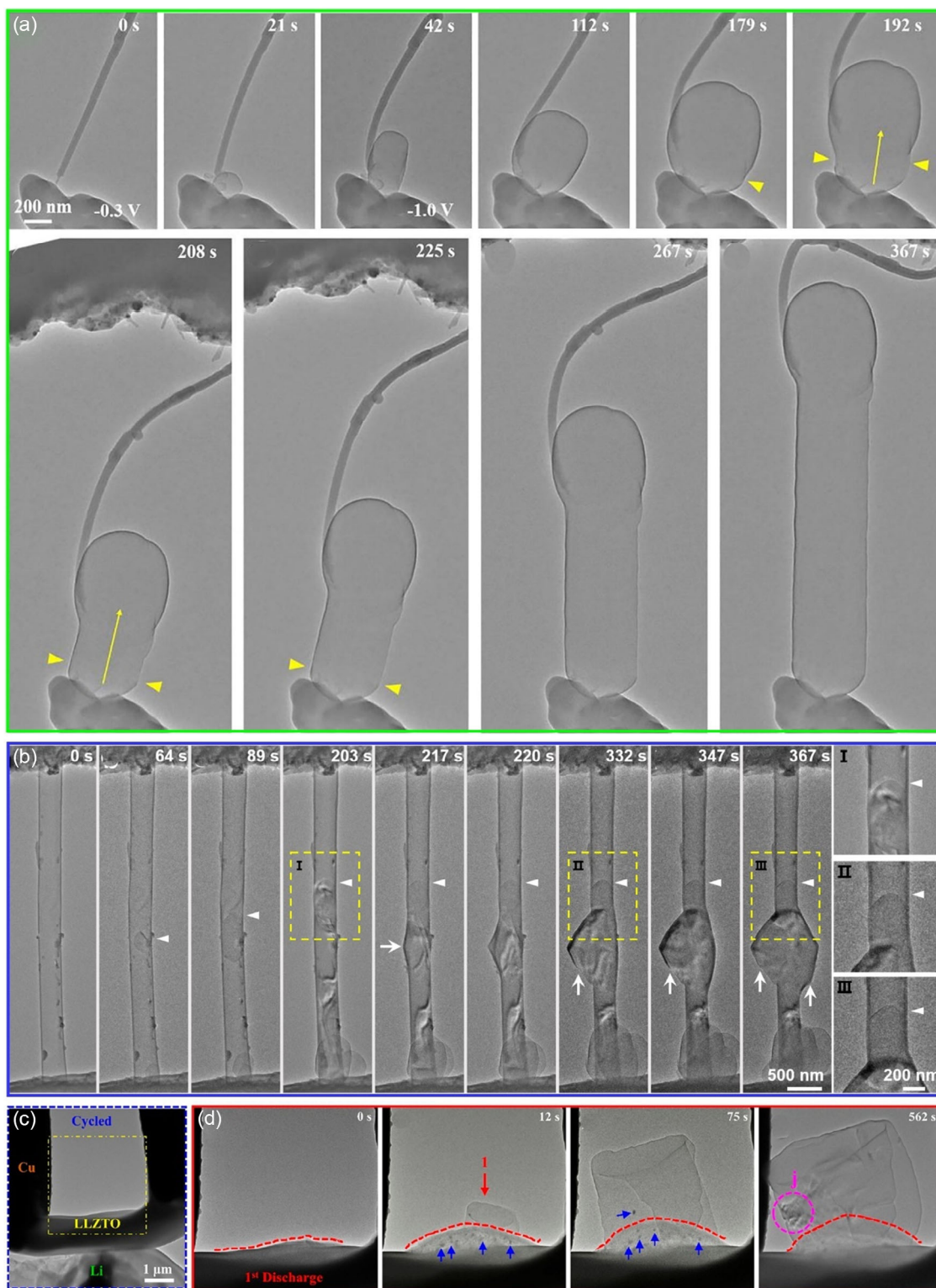


**Figure 17.** a) In situ TEM images showing an electroplated Li dendrite at applied voltage of  $-0.3$  and  $-1.0$  V in a  $\text{CO}_2$  atmosphere. Reproduced with permission.<sup>[126]</sup> Copyright 2021, Elsevier. b) Time-lapse TEM images demonstrating the fracture of CNTs caused by Li deposition in  $\text{CO}_2$  under an applied voltage of  $-0.8$  V. Panels I, II, and III are the enlarged corresponding regions shown in (b). Reproduced with permission.<sup>[127]</sup> Copyright 2021, American Chemical Society. c) Illustration of the experimental setup. d) Time-lapse TEM images showing Li dendrites penetrating through LLZTO during cycling. Reproduced with permission.<sup>[128]</sup> Copyright 2021, American Chemical Society.

fractured on the left side (panels 332 and 347 s of Figure 17b). Based on the fracture strength of the lithiated CNT, which is estimated to be around 1.0 GPa, the authors propose that the stress generated by Li deposition could reach the gigapascal level, leading to the fracture of the CNTs.

In another study<sup>[128]</sup> with the employed setup shown in Figure 17c, the same group discovered that a bulge appeared on the top surface of the LLZTO when a negative potential was applied (depicted in panel 0 s of Figure 17d). This electrochemically deposited bulge grew with the elapse of time (panels 12–562 s in Figure 17d). As the bulge grew, it was observed that small dark particles (indicated by blue arrows in Figure 17d) detached from the LLZTO were transported by continuous Li deposition. At the same time, a cylindrical-shaped Li dendrite formed around the center of the SE (as shown in panel 12 s in Figure 17d), which then grew to 1710 and 2356 nm in diameter after 75 and 562 s. These images demonstrate that LLZTO could be damaged and the chipped off LLZTO debris are wrapped up and carried away by the deposited Li during the Li deposition.

Very recently, Gao et al. conducted an in-depth study of the Li deposition mechanics and related breakdown mechanisms of SE by observing the evolution of the Li|LLZO interface through in situ TEM.<sup>[129]</sup> **Figure 18a** shows the anode-free Li|LLZO|Cu nanobattery setup for in situ TEM probing. They first studied the Li deposition behavior that was constrained by a thick copper (Cu) CC at low rate. In Figure 18b, it is evident that Li crystallization occurred at the Cu|LLZO interface and the deposited Li caused a slight displacement of the Cu probe away from the LLZO, thereby producing a significant uniaxial stress. Consequently, Li began to extend laterally within the gap between the Cu and LLZO interfaces. The lateral growth of Li was attributed to the creep motion of Li metal. Additionally, they discovered that during the lateral expansion of Li, the Li {110} plane was consistently exposed on the upper advancing face, whereas the {112} and {002} planes alternately appeared on the lower advancing face. This is due to the lowest surface energy of the {110} planes of the body-centred cubic (BCC) metal. Then the authors studied the Li deposition behavior using a flexible W tip as CC that offered a variable degree of constraint. Figure 18c shows that Li<sup>+</sup> ions originating from LLZO were electrochemically reduced at the W|LLZO interface, resulting in the formation of a faceted Li particle. With the accumulation of more neutralized Li<sup>0</sup> atoms at the Li|LLZO interface, the Li particle developed into a dendrite, causing the W tip to lift upward, in line with previous research findings.<sup>[124,125]</sup> As the Li dendrite continued to extend, the growth of the root was ultimately impeded by the increasing compression exerted by the W tip. Thereafter, the dendrite began to laterally swell at its shank (Figure 18c, bottom row). Due to the generation of significant compressive stress at the Li|LLZO interface during Li insertion, the accumulated Li<sup>0</sup> atoms were required to diffuse either through the bulk or surface of the dendrite to alleviate the stress, with the potential diffusion path shown in Figure 18d. Given that at room temperature, the diffusivity of Li atoms through the bulk is four orders of magnitude lower than that on the free surface (path 1 vs path 2, 10–15 m<sup>2</sup> s<sup>-1</sup> vs 10–11 m<sup>2</sup> s<sup>-1</sup>), it was proposed that the inserted Li atoms could initially diffuse along the Li|LLZO interface toward the triple-phase boundary, followed by potentially faster transport on the Li surface, as indicated by path 3.

They then studied the LLZO cracking caused by the Li deposition-induced stress under high-voltage bias and constraint condition. In Figure 18e, a thick Cu probe was placed in contact with an individual LLZO particle, and a high voltage of 3 V was applied to stimulate the rapid deposition of Li at the Cu|LLZO interface, which is indicated by the yellow dashed line in panel 1.2 s of Figure 18e. Subjected to significant mechanical constraint from the Cu probe, the rapid Li accumulation resulted in a substantial stress buildup in the contact region. Consequently, a crack containing Li metal suddenly formed on the LLZO surface (as depicted in panel 1.6 s of Figure 18e). Upon further Li deposition, the crack was widely opened (panel 315.6 s in Figure 18e), resulting in the transgranular pulverization of the LLZO particle (the right-most panel in Figure 18e). Therefore, continued Li infiltration into the split particle can lead to the complete penetration of the particle and cause a short circuit in the battery. Apart from particle splitting, LLZO can also experience surface peeling as a form of fracture. As depicted in Figure 18f, the particle surface was peeled off into two fragments due to high-rate Li plating. This type of fracture could result from the lateral propagation of a crack within the LLZO subsurface. This process is schematically explained in the last three panels in Figure 18f. Due to the weaker pressure from the outside compared to the inner stress, pre-existing surface defects or cleavage planes of LLZO that formed a small angle with the particle surface would be more likely to initiate the fracture. As the crack propagated in the subsurface, the unbalanced stress caused the crack to change its direction of advancement toward the particle surface. Eventually, the detached piece was pushed out by the expanding Li, resulting in a dent on the LLZO surface.

It has to be noted that the difference in the geometry of the AFM electrode–electrolyte interface may give rise to different results during in situ TEM studies. Diaz and Kushima also conducted a quantitative analysis of Li dendrite growth using in situ TEM.<sup>[130]</sup> **Figure 19a** displays the process of Li dendrite growth captured by in situ TEM, while Figure 19b illustrates the changes in the Li dendrite geometry throughout the growth process, as well as the resulting force  $F_{Li}$  exerted by the dendrite against the cantilever. At the onset, a slight force was detected, representing the initiation of dendrite nucleation. As the dendrite grew, it exerted a progressively increasing force, causing the cantilever to move away from the surface and attaining a maximum value of 15.8 MPa. Subsequently, the Li dendrite ceased its growth in the vertical direction and began to expand laterally. The stress levels observed in this study differ from those reported in a similar study conducted by Wang's group.<sup>[124]</sup> Diaz and Kushima explained the discrepancy in terms of the distinct electrode–electrolyte geometry involved: a slender cantilever tip made contact with a relatively flat region of the SE, unlike a flat cantilever tip interfacing with a sharp SE. These results suggest that different cell design used in TEM studies may lead to different results.

Besides, some TEM results also support the proposed mechanism that high electronic conductivity properties of SE contribute to the Li dendrites nucleation and growth within SEs. Liu et al. pointed out that the local electronic structure variations at the GBs could lead to Li dendrites nucleation and formation within SEs.<sup>[131]</sup> They conducted the in situ TEM measurement of the selected triple-junction LLZO GB during voltage biasing. Via

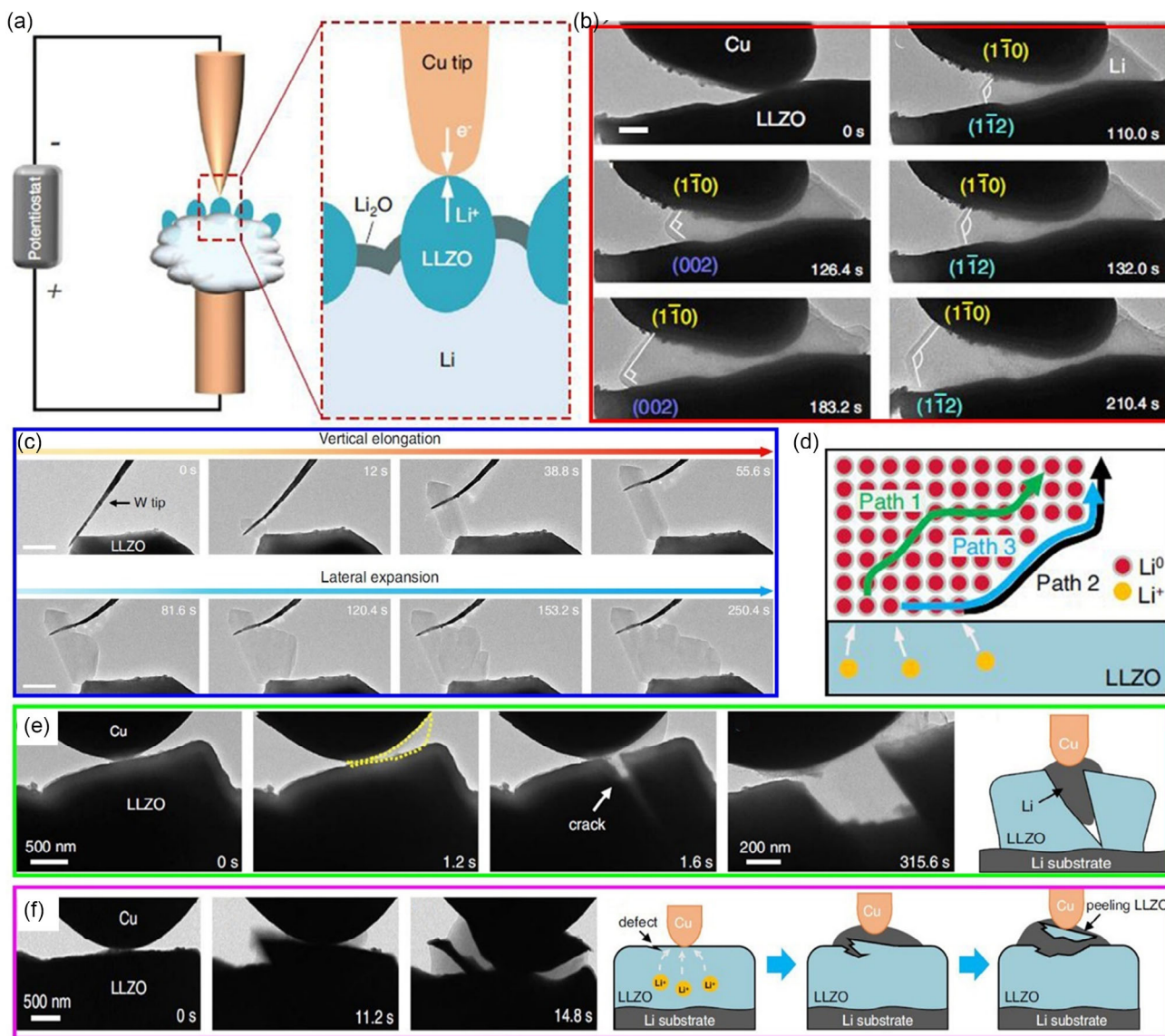


**Figure 18.** a) An illustration of the Cu|LLZO|Li nanobattery setup for in situ TEM probing, where the anode is absent. b) Time-lapsed TEM images showing the creeping growth of Li on the LLZO surface under the constraint of a rigid Cu current collector at a low deposition rate. The scale bar is 200 nm. c) The top row displays the vertical elongation of a Li dendrite due to root growth, leading to an increase in stack pressure from the bent W tip. The bottom row shows the lateral swelling of the Li dendrite under a strong compressive stress and subsequent lateral expansion of Li. d) Three suggested pathways for  $\text{Li}^0$  atoms diffusion during lateral growth are shown in a schematic. e) Time-lapsed TEM images exhibiting Li eruption at the interface, causing a single LLZO particle to crack, along with a schematic illustration of crack opening and Li filling. f) Time-lapsed TEM images depicting the surface peeling of LLZO due to Li eruption, accompanied by corresponding schematics. Reproduced with permission.<sup>[129]</sup> Copyright 2022, Springer Nature.

recording the contrast changes in the triple junction that serves as an indicator of Li nucleation during Li plating, they clearly observed that newly generated phase flowed into the triple-junction void. And this newly emerged phase was confirmed using electron energy loss spectroscopy (EELS) analysis to be Li. Combining further studies, the authors argued that the bandgap of the LLZO GBs is reduced compared with the grains, rendering them potential channels for leakage current. Hence, when the local potential at GBs exceeds the bandgaps, electron flow would occur along the GBs, causing preferential  $\text{Li}^+$  ions reduction at these regions. These results are in good agreement with the report from Kim et al., who extensively examined the

energy band structures of the LLZO grains using reflection EELS, scanning photoelectron microscopy, and nanoscale charge-based deep-level transient spectroscopy.<sup>[132]</sup>

#### 4. Summary of Li Penetration Mechanisms in SEs

The above-shown experimental results suggest that the Li penetration through SEs is a complicated scenario involving multidisciplinary. They also indicate that several mechanisms, instead of one, may govern the Li dendrites growth and penetration. Despite various theories put forward in the literature, there is

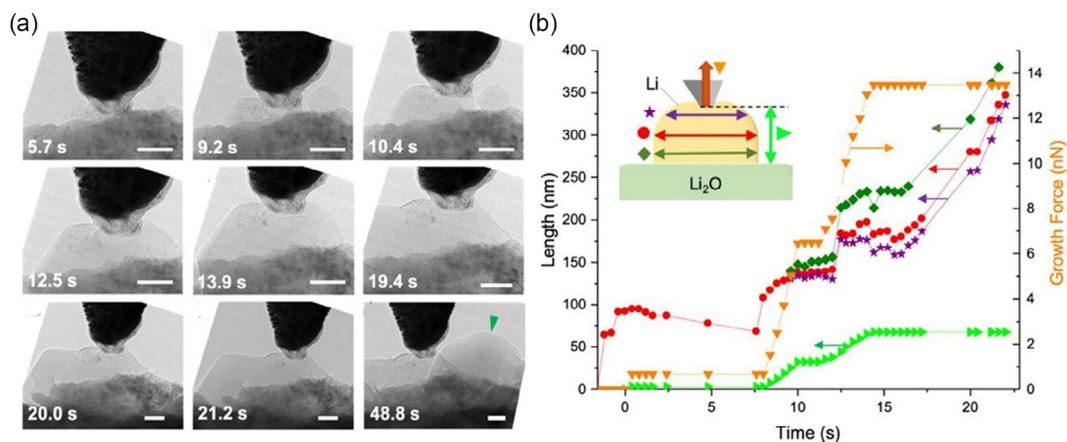


**Figure 19.** a) Time-lapsed TEM images showing Li dendrite growth displacing cantilever. Scale bar is 50 nm. b) A sequence showing the changing dendrite geometry and the corresponding growth force over time. Reproduced with permission.<sup>[130]</sup> Copyright 2021, The Electrochemical Society.

still no widely accepted explanation for how the low yield strength of Li metal can lead to dendrite penetration through ceramics with high fracture toughness. The dominant mechanism for Li penetration through SEs remains unclear and is likely to be more complex than in liquid-state electrolytes due to the presence of GBs, random voids, and cracks in SEs. There have been several proposed explanations for the unexpected behavior of dendrite growth in inorganic SEs. On the basis of the experimental results presented in Section 3 and previous reports,<sup>[11,14,133]</sup> two mainstream mechanisms of Li penetration through SEs are summarized in **Figure 20**: the mechanical fracture-assisted Li propagation (mode 1) and the electronic conductivity-induced Li plating inside SE (mode 2).

Mode 1 involves the formation and propagation of Li dendrites, taking into account the microstructural features of the SE such as pre-existing flaws and defects, GBs, and voids. This failure mode is rooted in Griffith's theory of fracture mechanics. It is suggested that Li electrodeposition commences at surface flaws when the current density exceeds a critical threshold, and upon reaching a point where the electrochemically generated stress surpasses the fracture toughness of the SE, crack propagation ensues. Following the formation of a new crack, Li metal can plate into the void space, leading to additional stress buildup at the crack tip. This stress buildup continues to drive crack growth, reaching a point where it surpasses the fracture toughness of the SE once more.<sup>[12]</sup>

On the one hand, the inorganic SEs are readily cracked/fractured due to their unique mechanical properties. According to the fracture mechanics, the existence of heterogeneous structures of SEs, such as flaws, voids, cracks, and GBs, could significantly decrease the fracture toughness of SE and facilitate crack extension. In accordance with experimental evidence, a pre-existing crack on the SE surface can be effortlessly filled with Li deposition due to the amplification of the electric field. Subsequent insertion of the deposited Li into the crack generates a substantial hydrostatic pressure at the crack tip, thus promoting crack propagation into the bulk of the SEs. Another example is the widely observed web-structure Li plating along the GBs in the SEs. It is suggested that the significant reduction in

the elastic modulus of GBs may contribute to dendrite propagation along these boundaries. In this situation, metallic Li is more prone to forming nuclei in the softer areas in the vicinity of GBs.

On the other hand, the mechanical characteristics of Li dendrites hold significant influence in mode I. Current investigations into the bulk mechanical behavior of Li have revealed the existence of power-law creep behavior in Li, which provides a framework for understanding the changes in mechanical stresses as Li is deposited within SE cracks, defects, and GBs. Furthermore, the discovered work hardening of Li at high strain rates and room temperature highlights the importance of the coupled relationship between current density and strain rates. Moreover, the recently demonstrated size effect of Li, which indicates a substantial increase in yield strength as the length scale decreases, underscores the importance of Li mechanics in influencing Li penetration through SEs.

Mode 2, in contrast, focuses on how the electronic properties of SEs govern Li dendrite growth. The abovementioned experimental results demonstrate the existence of isolated Li deposits within the SE, which was attributed to the high SE electronic conductivity. Moreover, recent theoretical studies propose that electrons trapped at GBs or surface defects can also initiate Li deposition events. Once Li was deposited within the SEs, the electronic conductive Li electrodeposits would trigger further Li electrodeposition because the electric field near the Li electrodeposits is much larger.<sup>[52]</sup> As the Li deposition process continues, the ultimate connection of these Li deposits leads to the short-circuiting of SSLBs.

In general, electronic partial conductivity is viewed as a necessary condition for internal Li nucleation within the SE according to mode 2. While the ideal SEs are anticipated to possess high ionic conductivity and minimal electronic conductivity, there are some SEs where the electronic conductivity is excessively high, allowing for the direct reduction of Li<sup>+</sup> ions within the SE. In addition, experimental studies also confirm that the electronic conductivity of SEs could be improved when the operating temperature is raised. Moreover, the existing pores, voids, and GBs are regions that can trap excess electrons and negative charges, leading to a direct reduction of Li<sup>+</sup> ions. Furthermore, it has to be

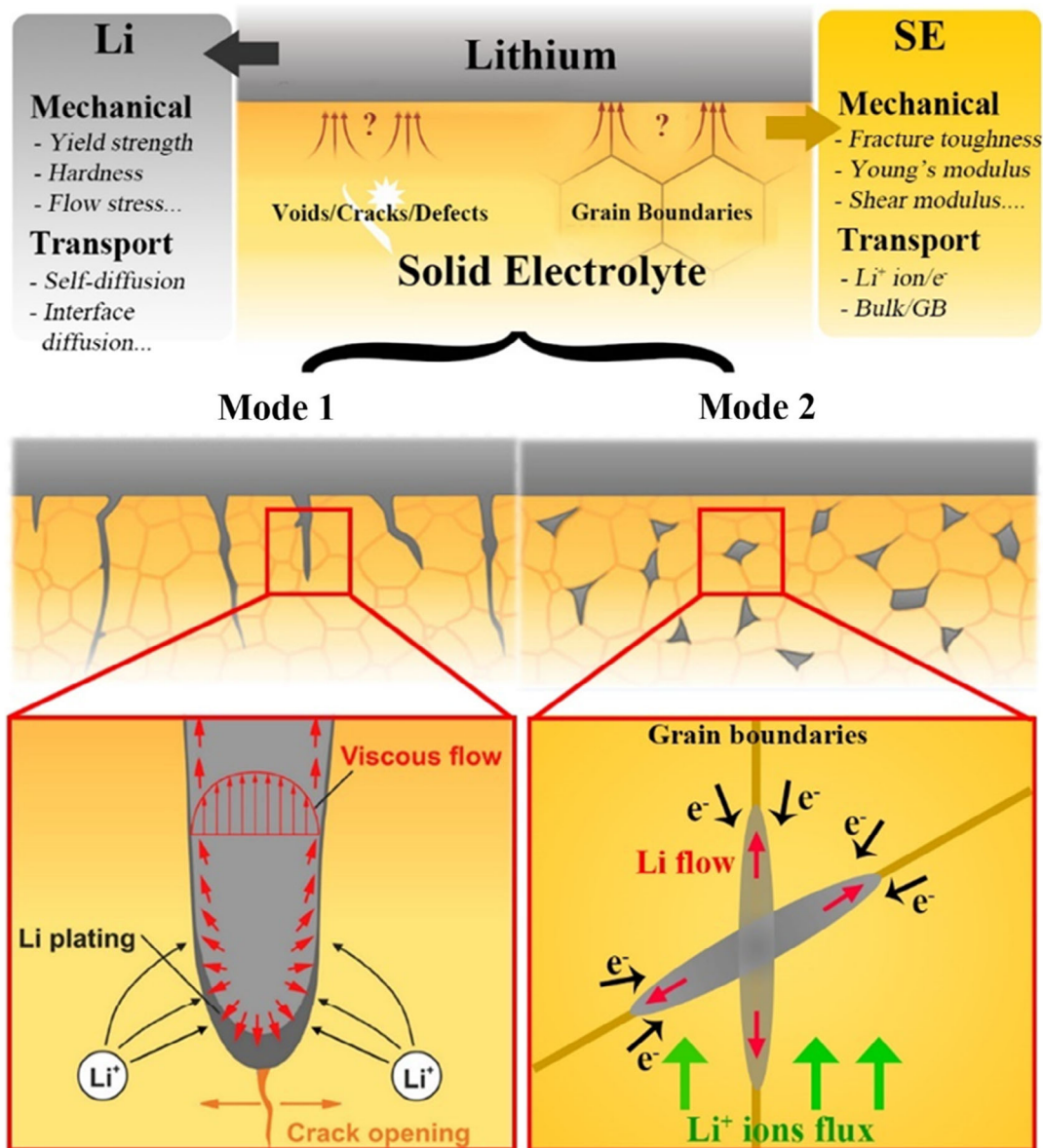


**Figure 20.** Schematics illustrating the two mainstream mechanisms of Li penetration through SE in SSLBs. The mode 1 features SE crack formation followed by Li dendrites propagation. The mode 2 describes how the electronic properties of the SE governs Li dendrites growth. Reproduced with permission.<sup>[11]</sup> Copyright 2020, American Chemical Society.

noted that donor doping, which is often utilized to stabilize SE to achieve better performance, may also introduce excess electrons and affect the Li dendrite growth. Despite this, the exact electronic conductive network within SEs remains unclear, given that Li nucleation within the SE requires both an electronic and an ionic conducting pathway to be present. Further research is needed to fully understand this mechanism.

Note that correctly differentiating these two modes is not always absolute because they do not stand alone. The recently developed electrochemomechanical coupling during Li penetration highlights the complexity and complication among the electrical, (electro)chemical, and mechanical properties of SE and Li. In addition, the recently discovered susceptibility of Li penetration under various experimental conditions also

demonstrates that different Li dendrites growth and penetration mechanisms may occur depending on different operating conditions. To sum up, a deeper investigation and understanding of dendrite growth mechanisms in SEs are necessary before practical and scalable strategies can be developed to expedite the implementation of SSLBs.

## 5. Strategies to Control Li Penetration in SEs via External Physical Fields

Efforts to mitigate, prevent, and inhibit dendrite formation are currently being actively researched, typically informed by the existing knowledge of Li dendrite growth and penetration.

Similar to the Li dendrites issues in liquid-state batteries, investigators have attempted to control and regulate Li dendrites growth and penetration in SSLBs by developing novel SE materials, engineering new Li anode structures, introducing coating layers, etc. as summarized elsewhere.<sup>[20,134]</sup> However, it has to be noted that most of these conventional strategies require involving additional material processing steps, introducing new materials, and adding new layers that eventually increase battery cost and complexity, which may hinder the wide deployment of SSLBs. In contrast, using external fields, such as mechanical force, temperature physical field, electric field, pulse current, and even magnetic field to regulate Li dendrites in SSLBs, seems to be the most cost-effective strategy. Based on the summarized Li dendrites growth and penetration mechanisms in SSLBs, strategies that employ these external fields to tackle the Li dendrite issues are summarized in this section. It is expected that these strategies could provide novel insights toward developing further efficient and cost-effective tactics to facilitate the development of SSLBs.

### 5.1. Mechanical Force

There is widespread recognition that mechanical pressure plays a significant role in the morphology of Li electrodeposits and the overall performance of liquid-state batteries. In addition, the crucial role of stack pressure on improving the overall battery performance in SSLBs has also been recognized. For the studies investigating the correlation between the mechanical stress and the current density using the inorganic SEs in SSLBs, it is referred to previous reports.<sup>[135–140]</sup> For the studies using the mechanical stress to suppress the Li dendrites penetration in polymer electrolytes, the readers can refer to previous reports.<sup>[141–144]</sup> In this section, the role of the stress field in governing/regulating Li dendrites growth and propagation through SEs in SSLBs is concentrated and elaborated.

Qi et al. first proposed using compressive mechanical stress to prevent the Li dendrites penetration through SEs.<sup>[145]</sup> They argued that a sufficient amount of compressive stress can hinder crack formation and cause existing cracks to close, thereby impeding Li dendrites from penetrating. The scientific principle underlying this is similar to stress corrosion cracking, a problem that has been extensively investigated and resolved in the field of corrosion. However, this technique may not be effective if compression of the SE significantly reduces the rate of Li<sup>+</sup> ion transport through it. The molecular dynamics calculations conducted by them showed that even the application of very high residual compressive stresses had only a small impact on the kinetics of Li<sup>+</sup> ion transport, which was experimentally validated by a recent study.<sup>[146]</sup> Ultimately, they recommended that although several commercial methods can be employed to introduce compressive residual stresses, ion implantation appears to be the most suitable approach for achieving this goal, as it may provide a novel path for creating controllable, high-performance, and mechanically stable SEs.

In a recent experiment, Fincher et al. reported controlling Li dendrites propagation in SSLBs using external mechanical stress.<sup>[147]</sup> **Figure 21a** illustrates the experimental setup, which involves mounting a solid-state cell (with a diameter of

approximately 1.27 cm) on a cantilever beam that was positioned to allow for bending of the beam to apply a stress  $\sigma_{\text{applied}}$  perpendicular to the direction of the electric field (as shown in Figure 21b–d). While the experiment was ongoing, operando OM was performed while varying current and mechanical load independently. The authors observed that metal dendrites responded in a correlated manner to the applied mechanical loads. Specifically, they conducted an experiment in which a 90  $\mu\text{m}$  thick LLZTO disk subjected to 70 MPa compression and then unloaded at 0.2 mA cm<sup>-2</sup> plating. Upon loading, they observed that the Li dendrite deflected toward the loading axis, and upon removing the load, it returned to its original propagation direction. Figure 21e shows that the Li dendrites could deflect into the loading axis when the applied loads were high enough. The third panel in Figure 21e further shows that compressive loads of 200 MPa resulted in dendrite growth that was almost aligned with the loading direction, even when the current density was as high as 5 mA cm<sup>-2</sup>. The observed alignment of dendrites with the applied load aligns with the propagation of a pressurized crack. When there is compression, cracks tend to close and stop spreading in a direction perpendicular to the direction of compression. However, when a stress parallel to the plating direction was applied, they found that the load facilitated dendrite cracking. This shows that the direction of Li dendrite propagation can be altered by the presence of a specific stress field.

Based on the findings, a model of dendrites was created in which they were represented as metal-filled flaws with an initial angle  $\beta$  from the horizontal in a homogeneous and isotropic SE, as shown in Figure 21f. This model was created to describe the path of Li dendrites under mechanical loading from a fracture mechanics perspective. The model assumed that the metal plating into the flaw resulted in a uniform pressure of  $P$  perpendicular to the flaw face. The pressure from the plating caused the dendrites to advance in a straight line without bending in the absence of any other stresses in the SE. When a vertical load was added to the SE ( $\sigma_{yy}$ ), the most favorable path for the dendrites to continue growing was at an angle that was bent from its initial orientation, as depicted in Figure 21f. The stress state in the area in front of the crack tip was determined by adding together the pressure caused by the plating and the external load that was applied. The angle of most favorable dendrite propagation ( $\theta$ ) maximizes the local model I stress intensity factor for a tiny extension of the crack tip. This model effectively captures the main features of the observed behavior and provides guidelines for preventing short-circuiting in SSLBs caused by Li dendrite penetration.

The research demonstrates that the ongoing Li plating can lead to a buildup of pressure within the Li dendrites, which exerts a force on the flaw surface ( $P$  in Figure 21b) and promotes propagation. However, external compressive forces (such as  $\sigma_{\text{applied}}$  in Figure 21c) can have the effect of closing cracks and preventing the cracks from propagating perpendicular to the direction of the force. As a result, under increased load, cracks should tend to turn toward the direction of the force, which is in line with the observations in Figure 21e. These results clearly demonstrate that when there is a higher applied load, the dendrites bend and align closely with the direction of the load.



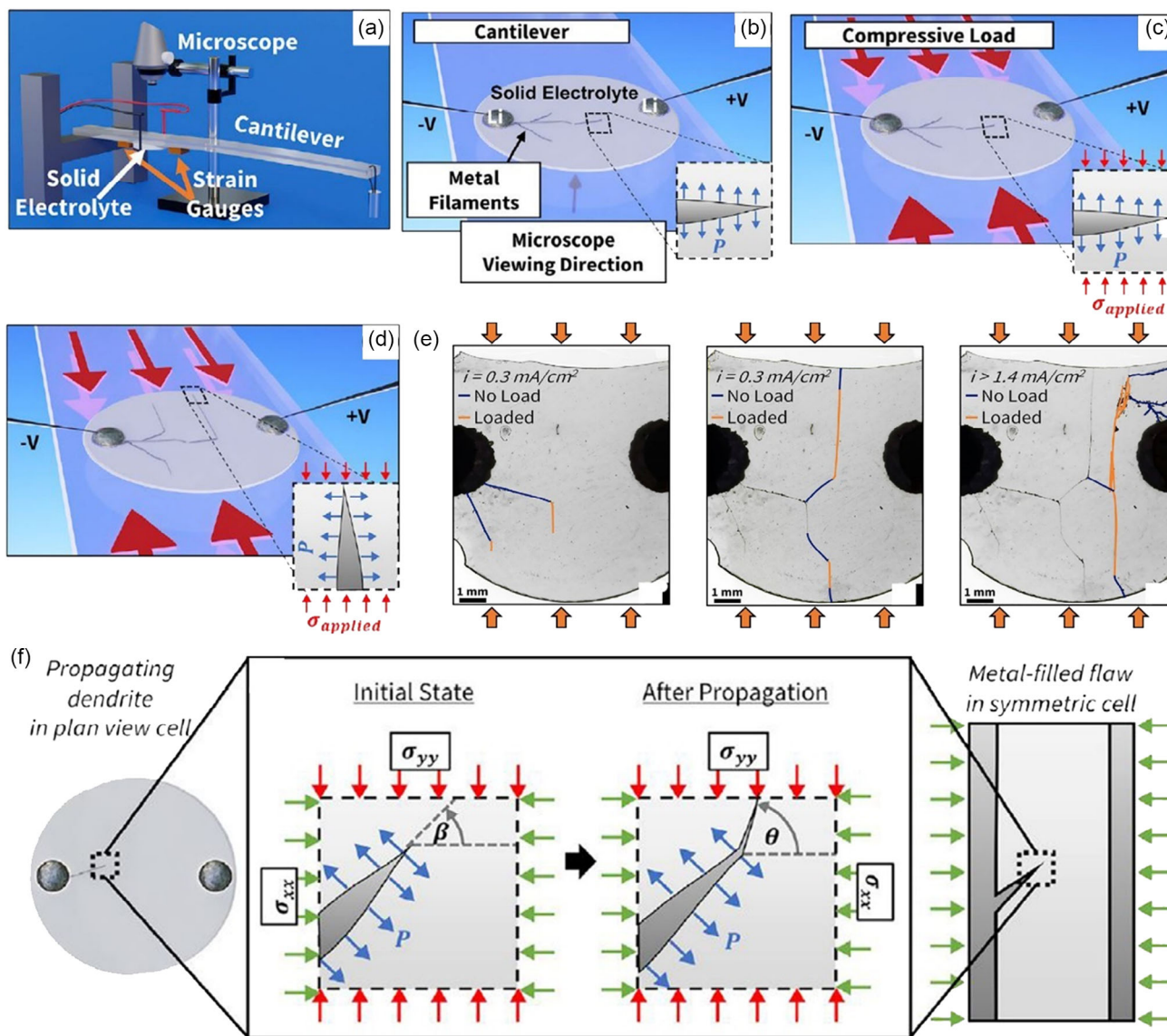


**Figure 21.** a) Schematic of the used setup consisting of Li metal adhered to a thin SE disk. b) The plan-view cell geometry and dendrite orientation in the load-free configuration. c) The cell under load. d) Dendrite deflection when propagating under compressive load. e) In operando microscopy images showing the response of propagating Li dendrites under different conditions. f) Schematic illustration explaining the Li dendrites growth under different conditions. Reproduced with permission.<sup>[147]</sup> Copyright 2022, Elsevier.

The authors created a methodology for conducting experiments and developed a fracture mechanics model that helps to understand the relationship between the electrochemical and mechanical forces that cause metal-dendrite propagation. They observed the development of Li dendrites in the model system,  $\text{Li}_{6,6}\text{La}_3\text{Zr}_{1,6}\text{Ta}_{0,4}\text{O}_{12}$  (LLZTO), when they subjected it to both electrochemical and mechanical stimulation, either one after the other or at the same time. Additionally, the authors used fracture mechanics to determine the level of mechanical stress required to stop or deflect dendrites and compared their predictions with the experimental results. In the last, the authors suggested a design approach to prevent or regulate dendrites by introducing compressive stresses into the SE during the production of SSLBs.

McConohy et al. also studied the Li dendrite growth directions using a LLZO cantilever under different mechanical conditions of strains/forces.<sup>[97]</sup> They found that Li dendrite growth were randomly oriented at 0% strain. At 0.033% compressive strain, the Li dendrite growth started to show some geometrical alignment. Strikingly, the Li dendrites growth exhibited a strong alignment along the cantilever longitudinal direction when the strain was 0.07%. The authors suggested that the dendrites grew in a specific direction due to the uniaxial compression, which helped to close cracks and increase the fracture toughness in the perpendicular direction.

It has to be noted that applying medium stack pressure increases tremendously the overall performance of SSLBs by improving the solid–solid interface stability, yet a large stack

pressure may fracture SEs and induce Li flow to cause unwanted internal short circuits.<sup>[148,149]</sup> In addition, application of stack pressure may increase the risk of mechanical failure of other battery components and is also technologically challenging.<sup>[150]</sup> Hence, determining the most appropriate mechanical pressure that can suppress Li dendrites growth without compromising the overall battery performance deserves more studies.

## 5.2. Temperature Effect

Thermal energy affects the performance of Li in three main ways: 1) it enhances the movement of ions and electrons in SEs, as well as charge transfer across the interface; 2) it modifies the diffusion properties of Li; and 3) it alters the elastic, plastic, and viscous properties of Li.<sup>[11]</sup> In the liquid-state batteries, it has been demonstrated that modulating temperature is a viable strategy for regulating the development of Li dendrite structures because higher temperature leads to lower overpotential and high mobility of Li<sup>+</sup> ions, both of which are favorable for the formation of uniform and compact Li electrodeposit layer.<sup>[151]</sup>

Motoyama et al. recently studied the temperature effects on Li nucleation at Cu|LiPON interfaces.<sup>[152]</sup> Figure 22a shows the SEM images of Li particles (dendrites) grown at different current densities and temperatures. It is evident from Figure 22a that the number of nucleation sites for Li increases with increasing current density and decreasing temperature. By employing the electrochemical impedance spectroscopy (EIS) technique, the researchers discovered that both the nucleation overpotential and nucleation number density decreased with an increase in temperature. The reason behind this is that the diffusivity of Li<sup>+</sup> ions along the Cu|LiPON interface increases with temperature, which leads to a greater number of Li atoms being incorporated into a single Li nucleus. In addition, Jolly et al. also studied the temperature dependence of Li anode voiding in argyrodite SSLBs.<sup>[153]</sup> The authors discovered that voiding at the Li|LPSCl interface decreased with increased temperatures, and the critical current density (CCD) before voiding and cell failure increased with elevated temperatures. This indicates that higher temperatures not only enhance the rate of Li self-diffusion within the Li metal but also cause creep. These results are in good agreement with previous reports using liquid-state batteries.<sup>[154–157]</sup>

Very recently, Parejiya et al. reported using short duration, high-voltage pulses to poorly formed Li|Li<sub>6.25</sub>Al<sub>0.25</sub>La<sub>3</sub>Zr<sub>2</sub>O<sub>12</sub> (LALZO) interface to suppress Li dendrites growth and enable a uniform Li electrodeposition in SSLBs.<sup>[158]</sup> The authors noticed that the high current density that occurs locally around interfacial pores can enhance the contact between Li and LALZO because of the Joule heating effect. Figure 22b–d illustrates that the local current density in the proximity of the pore is expected to be enhanced because there is no electronic path through the voids. This alteration in the current distribution may result in a localized rise in the temperature of the Li metal due to Joule heating when higher current pulses are used. The computational fluid dynamics simulation findings revealed that the current density near the pore increased by a factor of four compared to the applied current density. This high local current density caused Li to deposit preferentially in those regions during the plating process. Additionally, the calculations for the increase in local

temperature assumed that the electrical power associated with the local current density near the pore was completely converted into heat. It was assumed that this heat would be dissipated within the Li metal and the estimated local temperature increase was found to be between 10 and 300 °C, depending on the pore geometry, as depicted in Figure 22c. A higher local temperature of Li indicates a higher homologous temperature, leading to increased creep, which reduces the likelihood of forming Li dendrites.<sup>[159]</sup>

However, it is important to note that localized temperature hotspots can significantly increase the exchange current density of the confined region, which may stimulate the growth of Li dendrites.<sup>[160]</sup> The recent study<sup>[161]</sup> demonstrated that temperature hotspots can cause a tremendous increase in Li dendrite growth compared to the surrounding areas due to the locally enhanced exchange current density. Furthermore, localized high temperatures can be one of the factors that lead to internal shorting in the battery, which, in turn, increases the temperature and accentuates the risk of thermal runaway. Therefore, increasing the cell temperature has the potential to solve the issue of stable Li electrodeposition, but it also presents some drawbacks. On the other hand, it is also noteworthy that achieving dendrite-free in SSLBs operated under low-temperature ranges is also of crucial importance for their practical deployment at temperatures below 0 or even −40 °C.<sup>[162]</sup> Recent studies demonstrate that increasing simultaneously the ion transport dynamics and the interfacial charge transfer at SE|electrode interface can suppress the Li dendrites growth and enable stable battery operation even at −30 °C,<sup>[163,164]</sup> even though studies focusing on eliminating Li dendrites under both high- and low-temperature conditions are still in its infancy and need further clarifications. Further studies decoupling the underlying electrochemical–thermal complexations are highly desirable for enhancing the overall performance and safety of SSLBs.

## 5.3. Electric Field

Previous studies demonstrated that the Li dendrite tip effect can generate a locally enhanced electric field that draws nearby Li<sup>+</sup> ions and results in heterogeneous intensification of dendrite growth in the vertical direction, as schematically shown in Figure 23a.<sup>[165]</sup> Considering that this unevenly distributed electric field near the high-curvature Li tip during Li plating is one of the dominating factors hindering uniform Li deposition, alleviating or eliminating this factor seems to be imperative for obtaining uniform Li deposition. In this context, creating a new electric field that opposes the existing one locally could be a potentially viable approach. From the materials' point of view, ferroelectric materials, which can spontaneously polarize under applied electric fields by relatively displacing their positive and negative charge centers, could generate built-in electric field that has an opposite direction to the applied field.<sup>[166]</sup> Hence, the driving force for the preferential deposition of Li<sup>+</sup> ions at the Li dendrites tip is reduced, as schematically shown in Figure 23b. Based on this principle, both groups of Guo et al. and Wang et al. have demonstrated successfully the regulation of Li-dendrites by using barium titanate (BaTiO<sub>3</sub>, BTO) ferroelectric material in liquid-state batteries.<sup>[165,167]</sup>

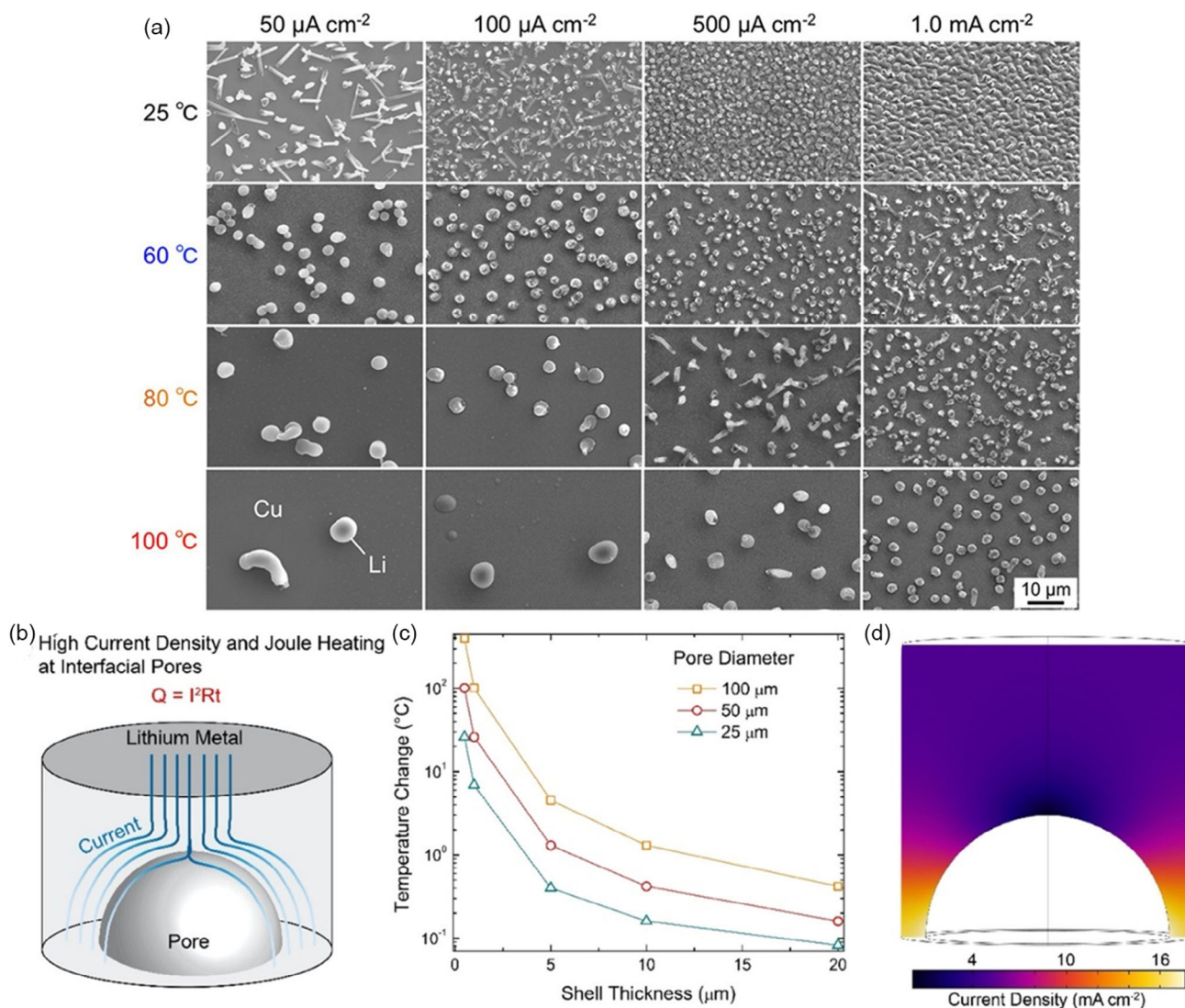


**Figure 22.** a) SEM images of plated Li for 180 mC cm<sup>-2</sup> using Cu current collector films at 50, 100, 150 μA cm<sup>-2</sup>, and 1 mA cm<sup>-2</sup> at each temperature of 25, 60, 80, and 100 °C. Reproduced with permission.<sup>[152]</sup> Copyright 2020, American Chemical Society. b) Schematic diagram showing current flow in the vicinity of a pore at the Li|LALZO interface. c) Temperature change in Li in the vicinity of a pore as a function of the pore size and the shell size considered for Joule heating. d) COMSOL simulation showing current density increase at the vicinity of the pore region. Reproduced under the terms of the CC BY license.<sup>[158]</sup> Copyright 2021, The Authors, Published by American Chemical Society.

Recently, the ferroelectric materials are utilized in solid-state batteries to suppress Li dendrite growth and penetration. Gu et al. engineered BTO-based ferroelectric interlayer between LATP and Li metal for stable SSLBs.<sup>[168]</sup> In their work, a composite interlayer made of ferroelectric BTO and poly(vinylidene fluoride-co-trifluoroethylene-co-chlorotrifluoroethylene (P[VDF-TrFE-CTFE]) (henceforth denoted as B-TERB) was constructed between LATP and Li metal anode, which could not only prevent the growth of Li dendrites but also enhance interfacial stability and maintain intimate contact. The simulation results showed that the B-TERB interlayer created an inverse polarized electric field that resulted in a uniform electric field and ion concentration distribution at the Li|SE interface. This helped to mitigate the tip effect and

promote lateral Li deposition. Shi et al. reported a strategy for creating high Li<sup>+</sup> ion conductive composite SE by coupling BTO and LLTO for high-voltage SSLBs.<sup>[169]</sup> In their work, a highly conductive composite SE was constructed by compositing the poly(vinylidene difluoride) matrix and BTO–LLTO nanowires with a side-by-side heterojunction structure (PVBL). The built-in electric field in BTO could weaken the space charge layers in the composite SE and reduce the Li<sup>+</sup> concentration gradient. Furthermore, the polarized BTO greatly promoted Li<sup>+</sup> ions transportation to coupled LLTO, achieving highly efficient ion transport. Due to the coupling effect, the built LiNi<sub>0.5</sub>Co<sub>0.1</sub>Mo<sub>0.1</sub>O<sub>2</sub>|PVBL|Li SSLB could stably cycle 1500 times at 180 mA g<sup>-1</sup> current density, and the pouch cells also exhibited excellent electrochemical and safety performance.

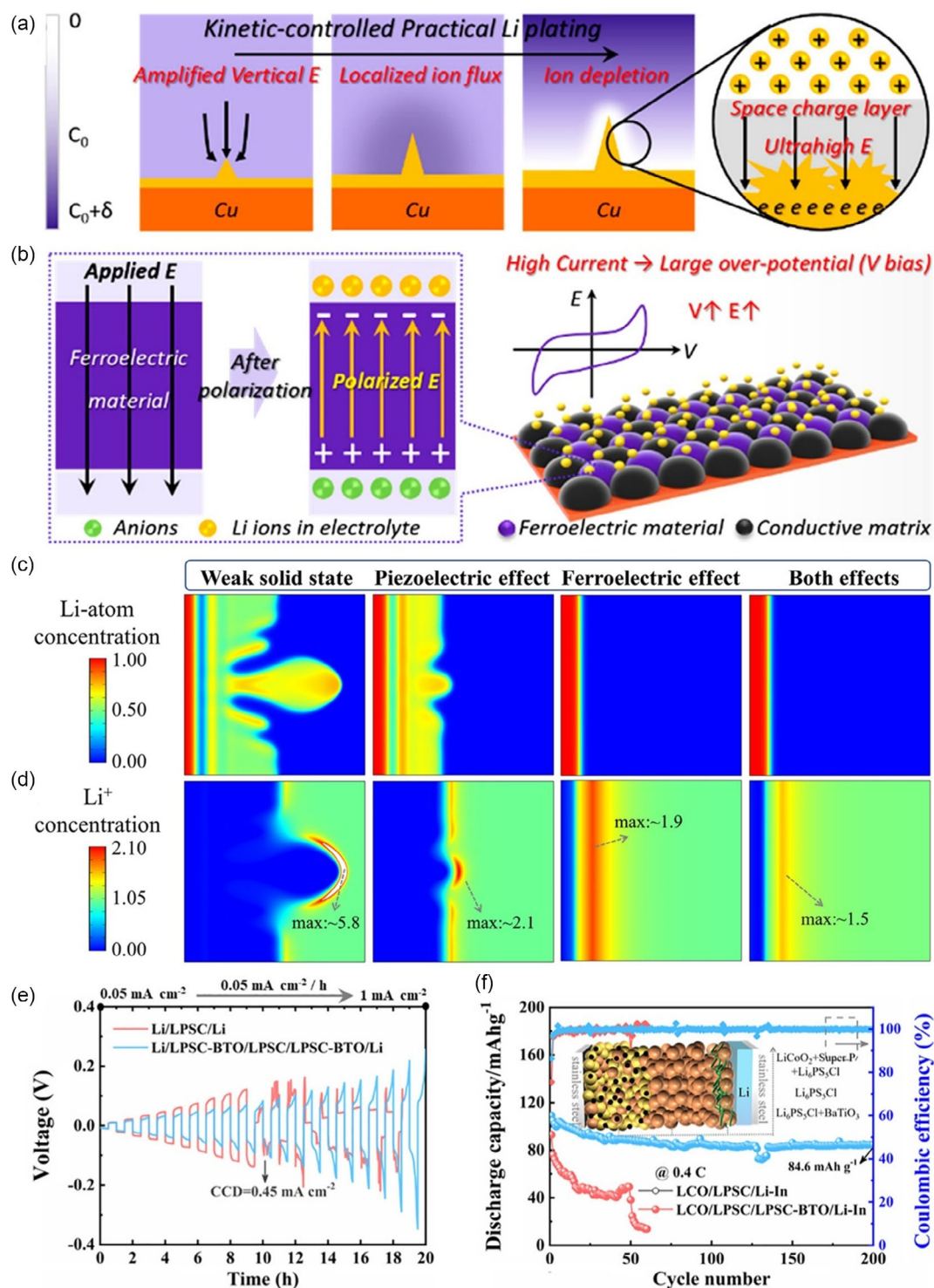


**Figure 23.** a) Illustration of the conventional Li plating behavior under the impact of an electric field and Li<sup>+</sup> ions flux, which generally leads to dendrite growth because of the tip effect. b) The built-in electric field by using ferroelectric materials under externally applied field. Reproduced with permission.<sup>[165]</sup> Copyright 2020, American Chemical Society. c,d) The simulated Li atom dimensionless concentration distribution (c) and Li<sup>+</sup> concentration distribution (d) after 86 s at 1 mA cm<sup>-2</sup> for the battery with weak solid state, piezoelectric effect, ferroelectric effect, and both piezo-/ferroelectric effects respectively. The left boundary of these two figures is Li, and the right is the SE. e) Representative potential response of the Li|LPSC|Li and Li|LPSC-BTO/LPSC/LPSC-BTO|Li cells undergoing cycling at 25 °C. f) Cycling performance at 0.4 C at 25 °C for the LCO|LPSC|Li-In and LCO|LPSC/LPSC-BTO|Li-In cells. Reproduced with permission.<sup>[170]</sup> Copyright 2022, National Academy of Sciences.

Very recently, Tao et al. reported on the incorporation of piezoelectric and ferroelectric BTO to combat Li dendrites in SSLBs.<sup>[170]</sup> The phase-field model was developed in their research to describe the growth of Li deposits under weak solid-state interactions, the presence of piezoelectric or ferroelectric fields, and the coexistence of both piezo- and ferroelectric fields. The model incorporated a phase that is both ionic conducting and piezo-/ferroelectric. Figure 23c–d displays 2D snapshots of the Li atom concentration, Li<sup>+</sup> ions concentration, and driving force after a time period of 86 s. The Li deposits in the weak solid-state interaction changed from a small initial bulge to multiple large and elongated dendrites quickly. Additionally, the Li<sup>+</sup> concentration in the weak-field scenario (Figure 23d) displays an uneven distribution, with a notable concentration gradient at the dendrite tip. This aggravates high-concentration polarization and results in the aggregation of the driving force for dendrite formation. In contrast, simulations of Li dendrite deposition under an electric field generated due to the piezoelectric properties of prestressed BTO showed that a stronger piezoelectric field responds to an electrical field in high curvature areas, which could reduce the growth and spread of dendrites. However, this electric field is not strong enough. This piezoelectric field can also lower the overpotential gradient at the tip, leading to a decrease in Li<sup>+</sup> ions concentration and a resulting smaller local Li<sup>+</sup> ions concentration. On the other hand, the ferroelectric effect was more effective and resulted in a nearly flat Li deposit. However, the Li<sup>+</sup> ions concentration distribution exhibited a wide transition layer and a maximum concentration gradient. The simultaneous use of both piezo- and ferroelectric fields resulted in the most uniform Li deposition during the simulation. They proposed that a counter-directional deflection of the electrical field connected to piezoelectricity and the maintenance of the electrical field connected to ferroelectricity during Li deposition could accelerate the elimination of Li dendrites and ensure long-term cycling performance.

In their experimental studies, they also directly compounded BTO with LPSCl powder to prepare the composite inorganic SE and the corresponding SSLBs, besides preparing the BTO- and polyethylene oxide (PEO)-based composite polymer electrolyte reference samples. Figure 23e shows that the Li|LPSCl–BTO/LBSCl/LPSCl–BTO|Li cell possesses a stable charge–discharge cycling behavior than the Li|LPSCl|Li control cell, indicating that the piezo-/ferroelectric effect of BTO is helpful for the sulfide SE. Additionally, Figure 23f shows that the LCO|LPSCl/LPSCl–BTO|Li–In cell also presents much better electrochemical stability than the control cell, delivering a high discharge capacity of 86.4 mAh g<sup>−1</sup> with a capacity retention ratio of 86.6% at 0.4C over 200 cycles.

#### 5.4. Current Field

Reports using pulsed currents, which are commonly used in electroplating of metals to obtain more uniform deposits, have been previously published in liquid-state batteries. Garcia et al. demonstrated that using repetitive current pulses in a Li|LiFePO<sub>4</sub> cell with conventional nonaqueous liquid electrolyte could suppress Li dendrite growth and increase its cycle life from

700 to over 6500 cycles.<sup>[171]</sup> Chen et al. studied the impact of applying external current fields including an alternative current field perpendicular to the Li anode and a direct current field parallel to the current to inhibit Li dendrites growth in liquid-state batteries.<sup>[172]</sup> The underlying science for suppressing Li dendrites growth using the pulse current is that, during a pulsed current program, where the current profile is interrupted by pauses, Li<sup>+</sup> ions have time to diffuse from areas of high concentration to areas of low concentration (during the pause), resulting in a denser and more uniform Li deposit. Despite its effectiveness in suppressing Li dendrites in conventional liquid-state batteries, the pulse current strategy has received minor attention in SSLBs until now.

Reisecker et al. recently investigated the influence of pulse-current protocol on Li dendrite formation and development in SSLBs using both SC and HP polycrystalline Li<sub>6</sub>La<sub>3</sub>ZrTaO<sub>12</sub> (LLZTO) SE.<sup>[173]</sup> The experimental results demonstrated that MHz pulsed currents could not effectively enhance the CCD of the SCs, but could improve that of the HPs to a sixfold increase. In addition, they found that the rate of Li deposition as a function of CCD increased at a rate 8.4 and 10.5 μm (s(mA cm<sup>−2</sup>))<sup>−1</sup> under direct and pulsed current operations, respectively, when using SC materials, indicating that the Li deposition mechanisms are not significantly affected by pulse currents. However, when the same approach was applied to the HP materials, the authors observed that the use of pulsed currents reduced the rate of Li dendrite growth with increasing CCD, decreasing from 13.7 to 1.1 μm (s(mA cm<sup>−2</sup>))<sup>−1</sup>. These findings indicate that the mechanism of Li growth and propagation differs in polycrystalline SEs when using pulsed currents compared to SC SEs.

Based on these experimental observations, Reisecker et al. proposed a hypothesis that the accumulation of Li<sup>+</sup> ions in the vicinity of a defect tip creates a critical pressure buildup, which ultimately leads to the failure of the SE and the propagation of dendrites. As the buildup of the critical Li<sup>+</sup> ion activity did not happen immediately after the current was turned on, applying current pulses of a short duration could prevent this occurrence. This suggested mechanism is schematically shown in **Figure 24**. The polycrystalline LLZTO SE in its original state (Figure 24a) exhibits surface defects. Upon applying an electrode overpotential (Figure 24b), Li<sup>+</sup> ions and electrons accumulate in close proximity to the defect tip. The ongoing accumulation of Li<sup>+</sup> ions and electrons near the defect tip leads to a local change in stoichiometry, which, in turn, results in a modification of the local lattice parameter under highly reducing conditions. This change only occurs in the vicinity of the defect-tip region and is suppressed by the mechanical constraints of the bulk LLZTO, which remains unaffected by changes in Li activity (Figure 24d). As a result, a significant elastic energy is accumulated until a critical Li activity level is reached, leading to stress relaxation through fracture (Figure 24e), followed by Li dendrite propagation (Figure 24f). In contrast, with pulsed currents, the Li activity can build up for only 1 μs with 1 MHz pulses, which is too brief to reach critical conditions, resulting in only minor lattice distortion (Figure 24g). During the subsequent microsecond, the Li<sup>+</sup> ion activity can relax again during the pause time (Figure 24h). When the current is switched back on, a similar starting condition is established and the cycle repeats itself (Figure 24i). This accounts for the increase in CCD and the decrease in the rate of Li dendrite propagation in HP samples

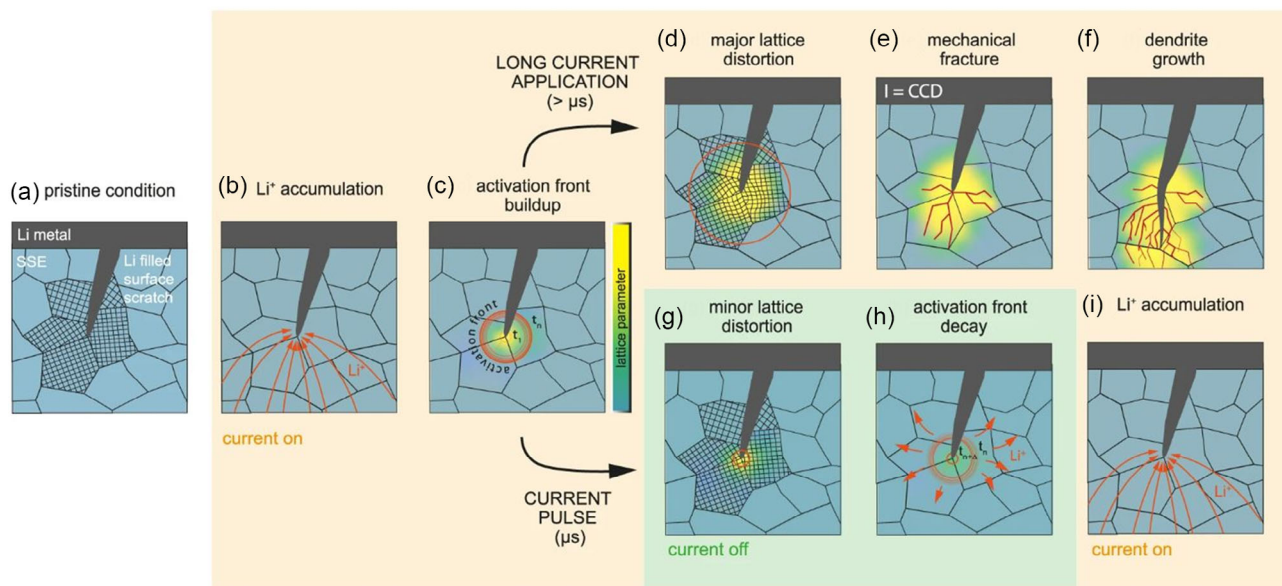


**Figure 24.** The proposed mechanisms in constant current and pulsed current electrochemical experiments using single crystalline (SC) and polycrystalline LLZTO SE. a) Pristine condition of the Li|SE interface exhibiting a surface scratch of the SE filled with Li, along with the lattice orientations of the adjacent grains near the defect tip. b) Once the current is switched on  $\text{Li}^+$  ions start to concentrate near the defect tip and c) cause the buildup of an activation front, LLZTO is thereby locally reduced and the lattice parameter in this region changed. d) In case of direct current pulse application this continuous lattice distortion causes a continuously increasing amount of pressure which, at some point, is released in form of e) mechanical fracture. Consequently, Li is plated along new cracks f) and drives the mechanical fracture even further until a short circuit. g) In case of short current pulses, the time for the activation front buildup is short enough to just cause a minor lattice distortion before the current is switched off again. h) The accumulated  $\text{Li}^+$  ions start to diffuse and distribute into the neighbouring regions, hindering a significant pressure to arise. i) Afterwards, the current is switched on again and the process repeats itself. Reprinted according to the terms of the CC-BY license.<sup>[173]</sup> Copyright The Authors 2023, published by Springer Nature.

when pulsed currents are applied, and why SC samples, which have no GBs, remain unaffected under the same conditions.

### 5.5. Magnetic Field

It is well known that the magnetic field could interact with the electric field and the interaction principle is based on magneto-hydrodynamics (MHD) effect,<sup>[174]</sup> as schematically shown in **Figure 25**. When the electric field ( $E$ ) was coupled with magnetic field ( $B$ ), the charged particles with the motion of cutting magnetic lines can be affected by the Lorentz force:

$$F = qvB \quad (7)$$

in which  $F$  is the Lorentz force,  $q$  is the quantity of electric charge,  $v$  is the velocity of the charged particles, and  $B$  is the magnetic flux intensity.<sup>[175]</sup> The Lorentz force can induce a solution vortex, i.e., the MHD effect. During the  $\text{Li}^+$  electrodeposition process, the bump on the current collector can cause the electric field lines to deviate, resulting in an intersection with the magnetic field lines. The  $\text{Li}^+$  ions that are accumulated near the protuberances due to the uneven electric field distribution can be influenced by the Lorentz force and dispersed by MHD, which stirs the electrolyte and enhances mass transport near the electrode surface. The locations and spots for  $\text{Li}^+$  ions to deposit are expanded, resulting in a more uniform electrodeposition on the current collector. Hence, Li dendrites can be eliminated.

Several groups conducted experiments using the external magnetic fields to suppress Li dendrites growth in liquid-state batteries.<sup>[176,177]</sup> In addition, several reviews summarizing the influence of the magnetic fields on the conventional liquid-state batteries are already reported.<sup>[178,179]</sup> Moreover, Han et al. recently reported using magnetic field aligned arrangement of functionalized sepiolite nanowires to prepare a PEO-based solid polymer electrolyte for SSLBs.<sup>[180]</sup> Unfortunately, studies adopting magnetic fields to suppress Li dendrites growth and propagation in SSLBs have not been reported yet to the best of the authors' knowledge.

## 6. Conclusion and Perspective

The uncontrolled Li dendrites growth and penetration issues in solid-state electrolytes have challenged the development of high-safety, energy-dense solid-state Li batteries. Although strategies that aim to suppress and block dendrites formation have been proposed, yet most of these conventional strategies require involving additional material processing steps, introducing new materials, and adding new layers that eventually increase battery cost and complexity, which may hinder the practical adoption of SSLBs. In contrast, using external fields, such as mechanical force, temperature physical field, electric field, pulse current, and even magnetic field to suppress Li dendrites penetration through SEs in SSLMBs, seems to be the most cost-effective strategy.

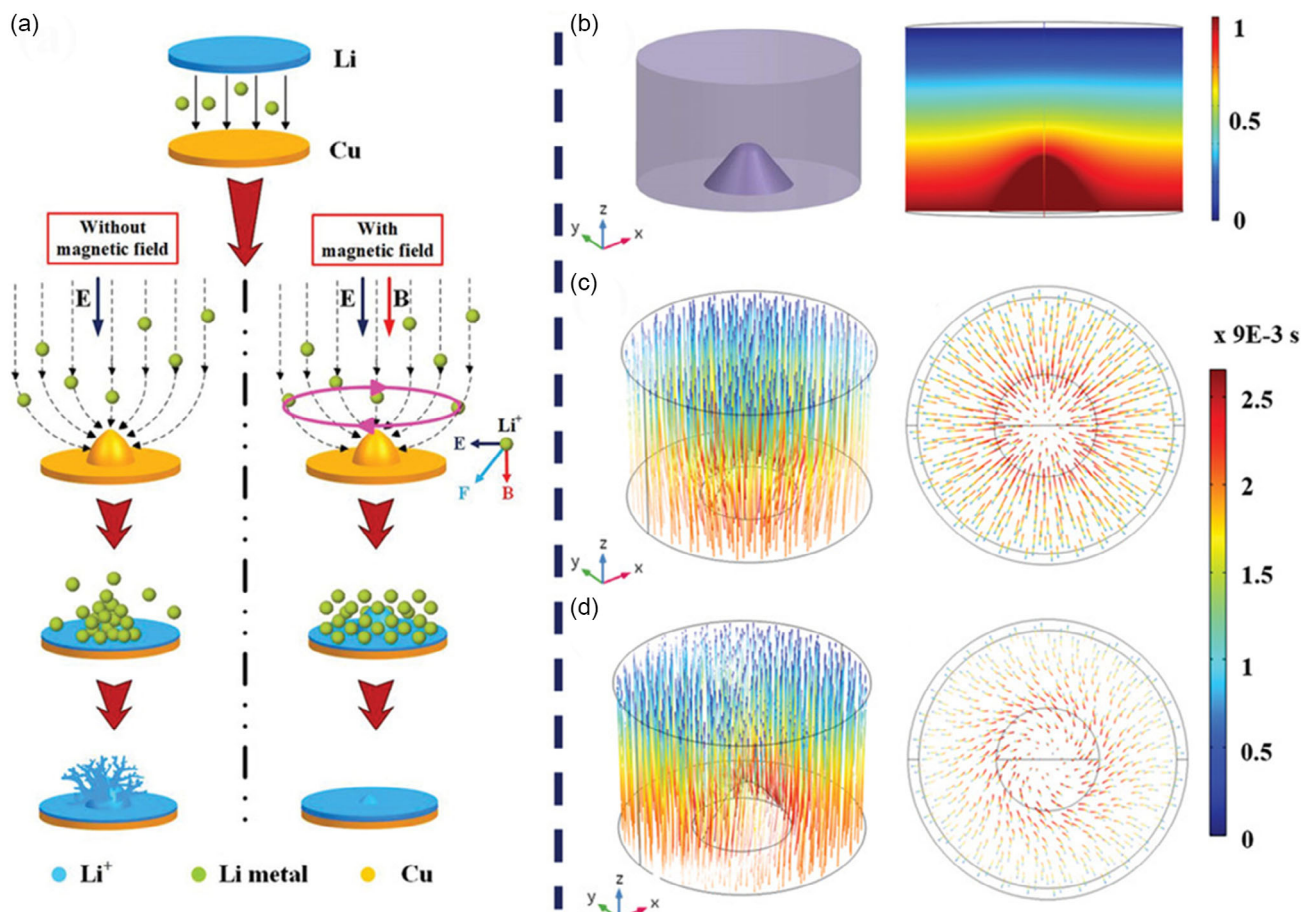


**Figure 25.** a) A diagram showing the effect of magnetic field on Li<sup>+</sup> deposition. b) A diagram showing the skeleton of a small bump on the Li surface (left) and its distribution in the surrounding area (right). c,d) Simulation results of the different paths of Li<sup>+</sup> ions during deposition process with (d) or without (c) magnetic field. The right scale represents the timeline. Reproduced with permission.<sup>[174]</sup> Copyright 2019, Wiley-VCH.

The current review focuses on summarizing the current research progress of utilizing external physical fields in regulating Li dendrites growth and penetration through inorganic SEs in SSLBs. We have first summarized the mechanical properties of Li metal and SEs, which are conducive for understanding the experimentally characterized Li dendrites penetration phenomena. In the following section, the experimental results obtained from various imaging techniques, which can provide direct and straightforward information of the Li dendrites nucleation and growth processes, are reviewed. Then, the two mainstream Li penetration mechanisms that are derived from the experimental results and gained most attentions from the researchers are summarized and discussed, i.e., the fracture mechanics and the electronic conductivity aspect. Afterward, strategies exploiting external physical fields in regulating Li dendrites growth in SEs are summarized in detail on the basis of the experimental results and the derived mechanisms. Although much progress has already been made in the characterization and understanding Li dendrites growth and penetration through SEs in SSLBs, significant challenges remain. In the following, some suggestions for future studies of Li metal when matching with SEs are provided and discussed.

Advanced and multiscale characterization tools for further clarifying the Li penetration mechanisms through SEs are desired. Experimental studies demonstrate that the Li penetration phenomenon transcends several length scales, from nanoscale Li nucleation and growth reactions to microscale Li dendrites propagation and macroscale SE crack failure.<sup>[181]</sup> Furthermore, these related processes evolve dynamically with time and electrochemical cycling, rendering them extremely challenging to characterize. Thus, an in-depth and comprehensive understanding of how Li dendrites penetrate SEs is extremely difficult to obtain. To enable controlling and regulating Li dendrites growth and propagation in SEs, dedicated further research is required to link the dynamically evolving Li dendrites to the electrochemical process. In this regard, the advanced in situ and even in operando measurements, which allow directly probing the dynamic structural evolution of Li dendrites in a realistic battery cell, could provide insightful mechanics into understanding the complex reactions and evolution of Li dendrites penetration phenomenon in SSLBs. In particular, 3D techniques that offer both high spatial and temporal resolution would be beneficial in further characterizing the location and morphological evolution of individual Li dendrites in 3D, providing unexpected insights into the Li penetration mechanisms in SSLBs.

The nature of the charge transportation in SE requires more detailed investigations. Visually tracking the  $\text{Li}^+$  ions transportation pathway is of great significance for understanding the Li dendrites growth and propagation. Although the  $\text{Li}^+$  ions transportation through the lithiophilic lithium alloys, which have been frequently used as metallic interlayers between Li and SE to regulate Li electrodeposition,<sup>[182]</sup> has been clarified to some extent,<sup>[183,184]</sup> a precise knowledge of and an in-depth understanding of the  $\text{Li}^+$  ion transportation in SEs during Li plating remain elusive. In addition, SEs can conduct both cations and electrons to varying degrees in practice. The unwanted electronic conductivity, or the electrons leakage through the SE, would undoubtedly facilitate the Li nucleation and growth within the SE. Nevertheless, considering that the electronic conductivities of the most SEs are several orders of magnitude lower than the ionic ones, it is interesting to understand how the percolating electronic pathways across the SEs are formed due to this negligible electronic conductivity. Bearing in mind that Li nucleation within the SE occurs when an electronic and an ionic conducting pathway intersect, fundamentally resolving the ionic and electronic conduction pathway within SEs during battery cycling is essential and imperative for a mechanistic understanding of the Li dendrites penetration phenomena.

A shift in focus toward electrochemomechanical coupling during Li penetration is also urgently needed. Recent studies demonstrate a strong coupling between mechanical loading and associated electrochemical process. And the close relationship between chemomechanical effects and battery performance is also being acknowledged. Particularly, the interplays of the mechanics and electrochemistry of both Li and SE are documented recently and these complicated electrochemomechanical couplings have crucial significance in dictating the Li dendrite formation and propagation in SEs. On one hand, electrochemical reactions such as Li deposition can lead to mechanical deformation and stress at the Li|SE interfaces, causing the deformation or even fracturing of the SE. On the other hand, the accumulated mechanical stress and the deformed/fractured SE would, in turn, strongly influence the following Li electrodeposition process. These issues are interconnected and stem from the intrinsic mechanical, chemical, and electrochemical properties of Li and SE. As such, it is necessary to conduct future research to gain a comprehensive electro-chemo-mechanical understanding of Li penetration.

Clarifying the underlying interdependence between the external fields and Li dendrites growth is highly desirable for proposing nondestructive strategies to control the Li dendrites penetration. On the basis of the knowledge obtained from the Li dendrites growth and penetration experiments, it is shown that by tuning the mechanical force, temperature, electric field, current field, and even magnetic field, the Li dendrites nucleation and growth behavior can be regulated. However, most of the hitherto reported studies focus on using individual external fields to control the Li dendrites in SE; the combined effects of them on Li plating mechanisms are largely unknown. For instance, only a few studies investigating how the mechanical force and temperature affect each other during Li plating/stripping are available and it is not determined yet if they can aid synergistically in controlling Li dendrites growth in the presence of electric or current fields. Understanding the intricate interplay between these

external fields as they evolve over time and with changes in the rate of charge/discharge current is another challenge that has not yet been thoroughly examined. In summary, this field is still in its early stages of development and requires more focused research.

## Acknowledgements

J.Y. and G.Z. contributed equally to this work. This work was sponsored by the National Natural Science Foundation of China (grant nos. 52101276, 22139001, and U22A20440), the Strategic Priority Research Program of Chinese Academy of Sciences (program no. XDA22010603), the Taishan Scholars of Shandong Province (grant no. ts201511063), and the Qingdao New Energy Shandong Laboratory.

## Conflict of Interest

The authors declare no conflict of interest.

## Keywords

Li dendrites, Li dendrites penetration mechanisms, solid electrolytes, solid-state batteries

Received: August 10, 2023

Revised: October 7, 2023

Published online:

- [1] S. Ohno, W. G. Zeier, *Nat. Energy* **2022**, *7*, 686.
- [2] J. Zhang, H. Wu, X. Du, H. Zhang, L. Huang, F. Sun, T. Liu, S. Tian, L. Zhou, S. Hu, Z. Yuan, B. Zhang, J. Zhang, G. Cui, *Adv. Energy Mater.* **2023**, *13*, 2202529.
- [3] J. Guo, D. Dong, J. Wang, D. Liu, X. Yu, Y. Zheng, Z. Wen, W. Lei, Y. Deng, J. Wang, G. Hong, H. Shao, *Adv. Funct. Mater.* **2021**, *31*, 2102546.
- [4] T. Risthaus, L. Chen, J. Wang, J. Li, D. Zhou, L. Zhang, D. Ning, X. Cao, X. Zhang, G. Schumacher, M. Winter, E. Paillard, J. Li, *Chem. Mater.* **2019**, *31*, 5376.
- [5] P. Bron, S. Johansson, K. Zick, J. Schmedt auf der Günne, S. Dehnen, B. Roling, *J. Am. Chem. Soc.* **2013**, *135*, 15694.
- [6] Y. Li, S. Song, H. Kim, K. Nomoto, H. Kim, X. Sun, S. Hori, K. Suzuki, N. Matsui, M. Hirayama, T. Mizoguchi, T. Saito, T. Kamiyama, R. Kanno, *Science* **2023**, *381*, 50.
- [7] P. Wang, W. Qu, W.-L. Song, H. Chen, R. Chen, D. Fang, *Adv. Funct. Mater.* **2019**, *29*, 1900950.
- [8] X. Nie, J. Hu, C. Li, *Interdiscip. Mater.* **2023**, *2*, 365.
- [9] F. Mo, J. Ruan, S. Sun, Z. Lian, S. Yang, X. Yue, Y. Song, Y.-N. Zhou, F. Fang, G. Sun, S. Peng, D. Sun, *Adv. Energy Mater.* **2019**, *9*, 1902123.
- [10] M. Du, K. Liao, Q. Lu, Z. Shao, *Energy Environ. Sci.* **2019**, *12*, 1780.
- [11] T. Krauskopf, F. H. Richter, W. G. Zeier, J. Janek, *Chem. Rev.* **2020**, *120*, 7745.
- [12] J. A. Lewis, J. Tippens, F. J. Q. Cortes, M. T. McDowell, *Trends Chem.* **2019**, *1*, 845.
- [13] M. Pasta, D. Armstrong, Z. L. Brown, J. Bu, M. R. Castell, P. Chen, A. Cocks, S. A. Corr, E. J. Cussen, E. Darnbrough, V. Deshpande, C. Doerr, M. S. Dyer, H. El-Shinawi, N. Fleck, P. Grant, G. L. Gregory, C. Grovenor, L. J. Hardwick, J. T. S. Irvine, H. J. Lee, G. Li, E. Liberti, I. McClelland, C. Monroe, P. D. Nellist,

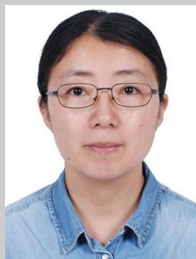


- P. R. Shearing, E. Shoko, W. Song, D. S. Jolly, et al., *J. Phys. Energy* **2020**, *2*, 032008.
- [14] J. Liu, H. Yuan, H. Liu, C.-Z. Zhao, Y. Lu, X.-B. Cheng, J.-Q. Huang, Q. Zhang, *Adv. Energy Mater.* **2022**, *12*, 2100748.
- [15] Y. Bae Song, H. Kwak, W. Cho, K. S. Kim, Y. Seok Jung, K.-H. Park, *Curr. Opin. Solid State Mater. Sci.* **2022**, *26*, 100977.
- [16] J. Gu, Z. Liang, J. Shi, Y. Yang, *Adv. Energy Mater.* **2023**, *13*, 2203153.
- [17] Z. Ahmad, V. Venturi, S. Sripad, V. Viswanathan, *Curr. Opin. Solid State Mater. Sci.* **2022**, *26*, 101002.
- [18] G. Deysher, P. Ridley, S.-Y. Ham, J.-M. Doux, Y.-T. Chen, E. A. Wu, D. H. S. Tan, A. Cronk, J. Jang, Y. S. Meng, *Mater. Today Phys.* **2022**, *24*, 100679.
- [19] L. S. de Vasconcelos, R. Xu, Z. Xu, J. Zhang, N. Sharma, S. R. Shah, J. Han, X. He, X. Wu, H. Sun, S. Hu, M. Perrin, X. Wang, Y. Liu, F. Lin, Y. Cui, K. Zhao, *Chem. Rev.* **2022**, *122*, 13043.
- [20] D. Cao, X. Sun, Q. Li, A. Natan, P. Xiang, H. Zhu, *Matter* **2020**, *3*, 57.
- [21] J. Ma, Y. Jiang, W. Chen, C. Luo, L. Zhang, H. Xu, J. Chang, W. Huang, C. Wang, S.-S. Chi, J. Wang, Y. Deng, *Appl. Phys. Lett.* **2022**, *121*, 193901.
- [22] R. Pacios, A. Villaverde, M. Martínez-Ibañez, M. Casas-Cabanas, F. Aguesse, A. Kvasha, *Adv. Energy Mater.* **2023**, *13*, 2301018.
- [23] J. Ma, S. Zhang, Y. Zheng, T. Huang, F. Sun, S. Dong, G. Cui, *Adv. Mater.* **2023**, *35*, 2301892.
- [24] C. Monroe, J. Newman, *J. Electrochem. Soc.* **2005**, *152*, A396.
- [25] T. M. Arruda, A. Kumar, S. V. Kalinin, S. Jesse, *Nano Lett.* **2011**, *11*, 4161.
- [26] E. J. Cheng, A. Sharafi, J. Sakamoto, *Electrochim. Acta* **2017**, *223*, 85.
- [27] F. Shen, M. B. Dixit, X. Xiao, K. B. Hatzell, *ACS Energy Lett.* **2018**, *3*, 1056.
- [28] E. Kazyak, R. Garcia-Mendez, W. S. LePage, A. Sharafi, A. L. Davis, A. J. Sanchez, K.-H. Chen, C. Haslam, J. Sakamoto, N. P. Dasgupta, *Matter* **2020**, *2*, 1025.
- [29] L. Porz, T. Swamy, B. W. Sheldon, D. Rettenwander, T. Frömling, H. L. Thaman, S. Berendts, R. Uecker, W. C. Carter, Y.-M. Chiang, *Adv. Energy Mater.* **2017**, *7*, 1701003.
- [30] B. Wu, S. Wang, J. Lochala, D. Desrochers, B. Liu, W. Zhang, J. Yang, J. Xiao, *Energy Environ. Sci.* **2018**, *11*, 1803.
- [31] A. Brazier, L. Dupont, L. Dantras-Laffont, N. Kuwata, J. Kawamura, J. M. Tarascon, *Chem. Mater.* **2008**, *20*, 2352.
- [32] F. Sun, L. Duchêne, M. Osenberg, S. Risse, C. Yang, L. Chen, N. Chen, Y. Huang, A. Hilger, K. Dong, T. Arlt, C. Battaglia, A. Remhof, I. Manke, R. Chen, *Nano Energy* **2021**, *82*, 105762.
- [33] F. Sun, K. Dong, M. Osenberg, A. Hilger, S. Risse, Y. Lu, P. H. Kamm, M. Klaus, H. Markötter, F. García-Moreno, T. Arlt, I. Manke, *J. Mater. Chem. A* **2018**, *6*, 22489.
- [34] S. Wenzel, S. J. Sedlmaier, C. Dietrich, W. G. Zeier, J. Janek, *Solid State Ion.* **2018**, *318*, 102.
- [35] S. H. Kim, K. Kim, H. Choi, D. Im, S. Heo, H. S. Choi, *J. Mater. Chem. A* **2019**, *7*, 13650.
- [36] K. N. Wood, K. X. Steirer, S. E. Hafner, C. Ban, S. Santhanagopalan, S.-H. Lee, G. Teeter, *Nat. Commun.* **2018**, *9*, 2490.
- [37] S. Wang, H. Xu, W. Li, A. Dolocan, A. Manthiram, *J. Am. Chem. Soc.* **2018**, *140*, 250.
- [38] L. E. Marbella, S. Zekoll, J. Kasemchainan, S. P. Emge, P. G. Bruce, C. P. Grey, *Chem. Mater.* **2019**, *31*, 2762.
- [39] C. Wang, Y. Gong, J. Dai, L. Zhang, H. Xie, G. Pastel, B. Liu, E. Wachsman, H. Wang, L. Hu, *J. Am. Chem. Soc.* **2017**, *139*, 14257.
- [40] F. Han, A. S. Westover, J. Yue, X. Fan, F. Wang, M. Chi, D. N. Leonard, N. J. Dudney, H. Wang, C. Wang, *Nat. Energy* **2019**, *4*, 187.
- [41] C. Xu, Z. Ahmad, A. Aryanfar, V. Viswanathan, J. R. Greer, *Proc. Natl. Acad. Sci.* **2017**, *114*, 57.
- [42] E. G. Herbert, S. A. Hackney, N. J. Dudney, P. S. Phani, *J. Mater. Res.* **2018**, *33*, 1335.
- [43] A. Masias, N. Felten, J. Sakamoto, *J. Mater. Res.* **2021**, *36*, 729.
- [44] E. G. Herbert, S. A. Hackney, V. Thole, N. J. Dudney, P. S. Phani, *J. Mater. Res.* **2018**, *33*, 1347.
- [45] C. Campbell, Y. M. Lee, K. Y. Cho, Y.-G. Lee, B. Lee, C. Phatak, S. Hong, *Sci. Rep.* **2018**, *8*, 2514.
- [46] Y. Song, L. Yang, W. Zhao, Z. Wang, Y. Zhao, Z. Wang, Q. Zhao, H. Liu, F. Pan, *Adv. Energy Mater.* **2019**, *9*, 1900671.
- [47] R. Koerver, W. Zhang, L. de Biasi, S. Schweidler, A. O. Kondrakov, S. Kolling, T. Brezesinski, P. Hartmann, W. G. Zeier, J. Janek, *Energy Environ. Sci.* **2018**, *11*, 2142.
- [48] F. Sun, C. Wang, M. Osenberg, K. Dong, S. Zhang, C. Yang, Y. Wang, A. Hilger, J. Zhang, S. Dong, H. Markötter, I. Manke, G. Cui, *Adv. Energy Mater.* **2022**, *12*, 2103714.
- [49] J. H. Cho, K. Kim, S. Chakravarthy, X. Xiao, J. L. M. Rupp, B. W. Sheldon, *Adv. Energy Mater.* **2022**, *12*, 2200369.
- [50] J. Janek, W. G. Zeier, *Nat. Energy* **2023**, *8*, 230.
- [51] T. Foroozan, S. Sharifi-Asl, R. Shahbazian-Yassar, *J. Power Sources* **2020**, *461*, 228135.
- [52] Y. Chen, Y. Jiang, S.-S. Chi, H. J. Woo, K. Yu, J. Ma, J. Wang, C. Wang, Y. Deng, *J. Power Sources* **2022**, *521*, 230921.
- [53] L. Qian, T. Or, Y. Zheng, M. Li, D. Karim, A. Cui, M. Ahmed, W. Park Hey, Z. Zhang, Y. Deng, A. Yu, Z. Chen, K. Amine, *Renewables* **2023**, *1*, 114.
- [54] F. Zhang, Q.-A. Huang, Z. Tang, A. Li, Q. Shao, L. Zhang, X. Li, J. Zhang, *Nano Energy* **2020**, *70*, 104545.
- [55] C. Wang, K. Fu, S. P. Kammampata, D. W. McOwen, A. J. Samson, L. Zhang, G. T. Hitz, A. M. Nolan, E. D. Wachsman, Y. Mo, V. Thangadurai, L. Hu, *Chem. Rev.* **2020**, *120*, 4257.
- [56] C. Wu, J. Lou, J. Zhang, Z. Chen, A. Kakar, B. Emlay, Q. Ai, H. Guo, Y. Liang, J. Lou, Y. Yao, Z. Fan, *Nano Energy* **2021**, *87*, 106081.
- [57] Y. Tang, L. Zhang, J. Chen, H. Sun, T. Yang, Q. Liu, Q. Huang, T. Zhu, J. Huang, *Energy Environ. Sci.* **2021**, *14*, 602.
- [58] A. Masias, N. Felten, R. Garcia-Mendez, J. Wolfenstine, J. Sakamoto, *J. Mater. Sci.* **2019**, *54*, 2585.
- [59] W. S. LePage, Y. Chen, E. Kazyak, K.-H. Chen, A. J. Sanchez, A. Poli, E. M. Arruda, M. D. Thouless, N. P. Dasgupta, *J. Electrochem. Soc.* **2019**, *166*, A89.
- [60] Y. Wang, Y.-T. Cheng, *Scr. Mater.* **2017**, *130*, 191.
- [61] P. Christiansen, P. A. F. Martins, N. Bay, *Exp. Mech.* **2016**, *56*, 1271.
- [62] S. Ding, L. Fairgrieve-Park, O. Sendetskiy, M. D. Fleischauer, *J. Power Sources* **2021**, *488*, 229404.
- [63] C. G. Haslam, J. B. Wolfenstine, J. Sakamoto, *J. Power Sources* **2022**, *520*, 230831.
- [64] J. E. Ni, E. D. Case, J. S. Sakamoto, E. Rangasamy, J. B. Wolfenstine, *J. Mater. Sci.* **2012**, *47*, 7978.
- [65] J. E. Ni, F. Ren, E. D. Case, E. J. Timm, *Mater. Chem. Phys.* **2009**, *118*, 459.
- [66] S. Yu, R. D. Schmidt, R. Garcia-Mendez, E. Herbert, N. J. Dudney, J. B. Wolfenstine, J. Sakamoto, D. J. Siegel, *Chem. Mater.* **2016**, *28*, 197.
- [67] S. D. Jackman, R. A. Cutler, *J. Power Sources* **2012**, *218*, 65.
- [68] Y.-H. Cho, J. Wolfenstine, E. Rangasamy, H. Kim, H. Choe, J. Sakamoto, *J. Mater. Sci.* **2012**, *47*, 5970.
- [69] E. G. Herbert, W. E. Tenhaeff, N. J. Dudney, G. M. Pharr, *Thin Solid Films* **2011**, *520*, 413.
- [70] E. A. Zimmermann, M. E. Launey, H. D. Barth, R. O. Ritchie, *Biomaterials* **2009**, *30*, 5877.
- [71] J. Wolfenstine, H. Jo, Y.-H. Cho, I. N. David, P. Askeland, E. D. Case, H. Kim, H. Choe, J. Sakamoto, *Mater. Lett.* **2013**, *96*, 117.
- [72] A. Sakuda, A. Hayashi, Y. Takigawa, K. Higashi, M. Tatsumisago, *J. Ceram. Soc. Jpn.* **2013**, *121*, 946.

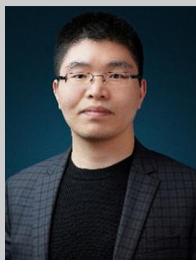
- [73] L. L. Baranowski, C. M. Heveran, V. L. Ferguson, C. R. Stoldt, *ACS Appl. Mater. Interfaces* **2016**, *8*, 29573.
- [74] F. P. McGrogan, T. Swamy, S. R. Bishop, E. Eggleton, L. Porz, X. Chen, Y.-M. Chiang, K. J. Van Vliet, *Adv. Energy Mater.* **2017**, *7*, 1602011.
- [75] K. Hikima, M. Totani, S. Obokata, H. Muto, A. Matsuda, *ACS Appl. Energy Mater.* **2022**, *5*, 2349.
- [76] F. Sun, H. Markötter, D. Zhou, S. S. S. Alrwashdeh, A. Hilger, N. Kardjilov, I. Manke, J. Banhart, *ChemSusChem* **2016**, *9*, 946.
- [77] F. Sun, H. Markötter, K. Dong, I. Manke, A. Hilger, N. Kardjilov, J. Banhart, *J. Power Sources* **2016**, *321*, 174.
- [78] F. Sun, C. Yang, I. Manke, L. Chen, S. Dong, *Mater. Today* **2020**, *38*, 7.
- [79] F. Sun, D. Zhou, X. Wang, I. Manke, L. Chen, *J. Energy Chem.* **2021**, *56*, 34.
- [80] F. Sun, D. Zhou, X. He, M. Osenberg, K. Dong, L. Chen, S. Mei, A. Hilger, H. Markötter, Y. Lu, S. Dong, S. Marathe, C. Rau, X. Hou, J. Li, M. C. Stan, M. Winter, R. Dominko, I. Manke, *ACS Energy Lett.* **2020**, *5*, 152.
- [81] C. E. Athanasiou, X. Liu, M. Y. Jin, E. Nimon, S. Visco, C. Lee, M. Park, J. Yun, N. P. Padture, H. Gao, B. W. Sheldon, *Cell Rep. Phys. Sci.* **2022**, *3*, 100845.
- [82] M. Papakyriakou, M. Lu, Y. Liu, Z. Liu, H. Chen, M. T. McDowell, S. Xia, *J. Power Sources* **2021**, *516*, 230672.
- [83] J. Zhao, C. Zhao, J. Zhu, X. Liu, J. Yao, B. Wang, Q. Dai, Z. Wang, J. Chen, P. Jia, Y. Li, S. J. Harris, Y. Yang, Y. Tang, L. Zhang, F. Ding, J. Huang, *Nano Lett.* **2022**, *22*, 411.
- [84] J. H. Um, S.-H. Yu, *Adv. Energy Mater.* **2021**, *11*, 2003004.
- [85] T. Swamy, R. Park, B. W. Sheldon, D. Rettenwander, L. Porz, S. Berendts, R. Uecker, W. C. Carter, Y.-M. Chiang, *J. Electrochem. Soc.* **2018**, *165*, A3648.
- [86] Q. Dai, J. Yao, C. Du, H. Ye, Z. Gao, J. Zhao, J. Chen, Y. Su, H. Li, X. Fu, J. Yan, D. Zhu, X. Zhang, M. Li, Z. Luo, H. Qiu, Q. Huang, L. Zhang, Y. Tang, J. Huang, *Adv. Funct. Mater.* **2022**, *32*, 2208682.
- [87] W. Guo, F. Shen, J. Liu, Q. Zhang, H. Guo, Y. Yin, J. Gao, Z. Sun, X. Han, Y. Hu, *Energy Storage Mater.* **2021**, *41*, 791.
- [88] M. Sun, T. Liu, Y. Yuan, M. Ling, N. Xu, Y. Liu, L. Yan, H. Li, C. Liu, Y. Lu, Y. Shi, Y. He, Y. Guo, X. Tao, C. Liang, J. Lu, *ACS Energy Lett.* **2021**, *6*, 451.
- [89] A. S. Westover, N. J. Dudney, R. L. Sacchi, S. Kalnaus, *ACS Energy Lett.* **2019**, *4*, 651.
- [90] J. Li, C. Ma, M. Chi, C. Liang, N. J. Dudney, *Adv. Energy Mater.* **2015**, *5*, 1401408.
- [91] J. Sastre, M. H. Futscher, L. Pompizi, A. Aribia, A. Priebe, J. Overbeck, M. Stiefel, A. N. Tiwari, Y. E. Romanyuk, *Commun. Mater.* **2021**, *2*, 76.
- [92] A. Sharafi, H. M. Meyer, J. Nanda, J. Wolfenstine, J. Sakamoto, *J. Power Sources* **2016**, *302*, 135.
- [93] Y. Ren, Y. Shen, Y. Lin, C.-W. Nan, *Electrochem. Commun.* **2015**, *57*, 27.
- [94] S. Heo, D. Lee, K. Kim, Y. Kim, D.-J. Yun, S. Park, J. Lee, S. Kim, J.-S. Kim, S. Park, *J. Power Sources* **2021**, *510*, 230389.
- [95] L. C. Zhang, J. F. Yang, C. L. Li, Y. X. Gao, X. P. Wang, Q. F. Fang, *J. Power Sources* **2020**, *449*, 227610.
- [96] J. Zhao, Y. Tang, Q. Dai, C. Du, Y. Zhang, D. Xue, T. Chen, J. Chen, B. Wang, J. Yao, N. Zhao, Y. Li, S. Xia, X. Guo, S. J. Harris, L. Zhang, S. Zhang, T. Zhu, J. Huang, *Energy Environ. Mater.* **2022**, *5*, 524.
- [97] G. McConohy, X. Xu, T. Cui, E. Barks, S. Wang, E. Kaeli, C. Melamed, X. W. Gu, W. C. Chueh, *Nat. Energy* **2023**, *8*, 241.
- [98] T. Krauskopf, R. Dippel, H. Hartmann, K. Peppeler, B. Mogwitz, F. H. Richter, W. G. Zeier, J. Janek, *Joule* **2019**, *3*, 2030.
- [99] T. Krauskopf, B. Mogwitz, H. Hartmann, D. K. Singh, W. G. Zeier, J. Janek, *Adv. Energy Mater.* **2020**, *10*, 2000945.
- [100] M. Golozar, A. Paoella, H. Demers, S. Savoie, G. Girard, N. Delaporte, R. Gauvin, A. Guerfi, H. Lormann, K. Zaghbi, *Sci. Rep.* **2020**, *10*, 18410.
- [101] B. Kinzer, A. L. Davis, T. Krauskopf, H. Hartmann, W. S. LePage, E. Kazyak, J. Janek, N. P. Dasgupta, J. Sakamoto, *Matter* **2021**, *4*, 1947.
- [102] C. Zhu, T. Fuchs, S. A. L. Weber, F. H. Richter, G. Glasser, F. Weber, H.-J. Butt, J. Janek, R. Berger, *Nat. Commun.* **2023**, *14*, 1300.
- [103] M. Nagao, A. Hayashi, M. Tatsumisago, T. Kanetsuku, T. Tsuda, S. Kuwabata, *Phys. Chem. Chem. Phys.* **2013**, *15*, 18600.
- [104] F. Sun, L. Zielke, H. Markötter, A. Hilger, D. Zhou, R. Moroni, R. Zengerle, S. Thiele, J. Banhart, I. Manke, *ACS Nano* **2016**, *10*, 7990.
- [105] F. Sun, R. Moroni, K. Dong, H. Markötter, D. Zhou, A. Hilger, L. Zielke, R. Zengerle, S. Thiele, J. Banhart, I. Manke, *ACS Energy Lett.* **2017**, *2*, 94.
- [106] F. Sun, M. Osenberg, K. Dong, D. Zhou, A. Hilger, C. J. Jafta, S. Risse, Y. Lu, H. Markötter, I. Manke, *ACS Energy Lett.* **2018**, *3*, 356.
- [107] F. Sun, X. He, X. Jiang, M. Osenberg, J. Li, D. Zhou, K. Dong, A. Hilger, X. Zhu, R. Gao, X. Liu, K. Huang, D. Ning, H. Markötter, L. Zhang, F. Wilde, Y. Cao, M. Winter, I. Manke, *Mater. Today* **2019**, *27*, 21.
- [108] F. Sun, R. Gao, D. Zhou, M. Osenberg, K. Dong, N. Kardjilov, A. Hilger, H. Markötter, P. M. Bieker, X. Liu, I. Manke, *ACS Energy Lett.* **2019**, *4*, 306.
- [109] N. Ishiguro, T. Totsuka, H. Uematsu, O. Sekizawa, K. Yamamoto, Y. Iriyama, Y. Takahashi, *ACS Appl. Energy Mater.* **2023**, *6*, 8306.
- [110] N. Seitzman, H. Guthrey, D. B. Sulas, H. A. S. Platt, M. Al-Jassim, S. Pylypenko, *J. Electrochem. Soc.* **2018**, *165*, A3732.
- [111] J.-M. Doux, H. Nguyen, D. H. S. Tan, A. Banerjee, X. Wang, E. A. Wu, C. Jo, H. Yang, Y. S. Meng, *Adv. Energy Mater.* **2020**, *10*, 1903253.
- [112] J. Tippens, J. C. Miers, A. Afshar, J. A. Lewis, F. J. Q. Cortes, H. Qiao, T. S. Marchese, C. V. Di Leo, C. Saldana, M. T. McDowell, *ACS Energy Lett.* **2019**, *4*, 1475.
- [113] J. A. Lewis, F. J. Q. Cortes, Y. Liu, J. C. Miers, A. Verma, B. S. Vishnugopi, J. Tippens, D. Prakash, T. S. Marchese, S. Y. Han, C. Lee, P. P. Shetty, H.-W. Lee, P. Shevchenko, F. De Carlo, C. Saldana, P. P. Mukherjee, M. T. McDowell, *Nat. Mater.* **2021**, *20*, 503.
- [114] M. Otoyama, M. Suyama, C. Hotehama, H. Kowada, Y. Takeda, K. Ito, A. Sakuda, M. Tatsumisago, A. Hayashi, *ACS Appl. Mater. Interfaces* **2021**, *13*, 5000.
- [115] M. B. Dixit, M. Regala, F. Shen, X. Xiao, K. B. Hatzell, *ACS Appl. Mater. Interfaces* **2019**, *11*, 2022.
- [116] H.-K. Tian, B. Xu, Y. Qi, *J. Power Sources* **2018**, *392*, 79.
- [117] N. Seitzman, O. F. Bird, R. Andrykowski, S. Robbins, M. M. Al-Jassim, S. Pylypenko, *ACS Appl. Energy Mater.* **2021**, *4*, 1346.
- [118] Y. Zheng, S. Zhang, J. Ma, F. Sun, M. Osenberg, A. Hilger, H. Markötter, F. Wilde, I. Manke, Z. Hu, G. Cui, *Sci. Bull.* **2023**, *68*, 813.
- [119] M. B. Dixit, N. Singh, J. P. Horwath, P. D. Shevchenko, M. Jones, E. A. Stach, T. S. Arthur, K. B. Hatzell, *Matter* **2020**, *3*, 2138.
- [120] S. Hao, J. J. Bailey, F. Iacoviello, J. Bu, P. S. Grant, D. J. L. Brett, P. R. Shearing, *Adv. Funct. Mater.* **2021**, *31*, 2007564.
- [121] S. Hao, S. R. Daemi, T. M. M. Heenan, W. Du, C. Tan, M. Storm, C. Rau, D. J. L. Brett, P. R. Shearing, *Nano Energy* **2021**, *82*, 105744.
- [122] Z. Ning, D. S. Jolly, G. Li, R. De Meyere, S. D. Pu, Y. Chen, J. Kasemchainan, J. Ihli, C. Gong, B. Liu, D. L. R. Melvin, A. Bonnin, O. Magdysyuk, P. Adamson, G. O. Hartley, C. W. Monroe, T. J. Marrow, P. G. Bruce, *Nat. Mater.* **2021**, *20*, 1121.
- [123] Z. Ning, G. Li, D. L. R. Melvin, Y. Chen, J. Bu, D. Spencer-Jolly, J. Liu, B. Hu, X. Gao, J. Perera, C. Gong, S. D. Pu, S. Zhang, B. Liu, G. O. Hartley, A. J. Bodey, R. I. Todd, P. S. Grant,

- D. E. J. Armstrong, T. J. Marrow, C. W. Monroe, P. G. Bruce, *Nature* **2023**, 618, 287.
- [124] Y. He, X. Ren, Y. Xu, M. H. Engelhard, X. Li, J. Xiao, J. Liu, J.-G. Zhang, W. Xu, C. Wang, *Nat. Nanotechnol.* **2019**, 14, 1042.
- [125] L. Zhang, T. Yang, C. Du, Q. Liu, Y. Tang, J. Zhao, B. Wang, T. Chen, Y. Sun, P. Jia, H. Li, L. Geng, J. Chen, H. Ye, Z. Wang, Y. Li, H. Sun, X. Li, Q. Dai, Y. Tang, Q. Peng, T. Shen, S. Zhang, T. Zhu, J. Huang, *Nat. Nanotechnol.* **2020**, 15, 94.
- [126] T. Yang, H. Li, Y. Tang, J. Chen, H. Ye, B. Wang, Y. Zhang, C. Du, J. Yao, B. Guo, T. Shen, L. Zhang, T. Zhu, J. Huang, *Sci. Bull.* **2021**, 66, 1754.
- [127] J. Chen, C. Zhao, D. Xue, L. Zhang, T. Yang, C. Du, X. Zhang, R. Fang, B. Guo, H. Ye, H. Li, Q. Dai, J. Zhao, Y. Li, S. J. Harris, Y. Tang, F. Ding, S. Zhang, J. Huang, *Nano Lett.* **2021**, 21, 6859.
- [128] H. Sun, Q. Liu, J. Chen, Y. Li, H. Ye, J. Zhao, L. Geng, Q. Dai, T. Yang, H. Li, Z. Wang, L. Zhang, Y. Tang, J. Huang, *ACS Nano* **2021**, 15, 19070.
- [129] H. Gao, X. Ai, H. Wang, W. Li, P. Wei, Y. Cheng, S. Gui, H. Yang, Y. Yang, M.-S. Wang, *Nat. Commun.* **2022**, 13, 5050.
- [130] M. Diaz, A. Kushima, *J. Electrochem. Soc.* **2021**, 168, 020535.
- [131] X. Liu, R. Garcia-Mendez, A. R. Lupini, Y. Cheng, Z. D. Hood, F. Han, A. Sharafi, J. C. Idrobo, N. J. Dudney, C. Wang, C. Ma, J. Sakamoto, M. Chi, *Nat. Mater.* **2021**, 20, 1485.
- [132] J.-S. Kim, H. Kim, M. Badding, Z. Song, K. Kim, Y. Kim, D.-J. Yun, D. Lee, J. Chang, S. Kim, D. Im, S. Park, S. H. Kim, S. Heo, *J. Mater. Chem. A* **2020**, 8, 16892.
- [133] M.-C. Pang, K. Yang, R. Brugge, T. Zhang, X. Liu, F. Pan, S. Yang, A. Aguadero, B. Wu, M. Marinescu, H. Wang, G. J. Offer, *Mater. Today* **2021**, 49, 145.
- [134] S. Jeong, Y. Li, W. H. Sim, J. Mun, J. K. Kim, H. M. Jeong, *EcoMat* **2023**, 5, e12338.
- [135] M. J. Wang, R. Choudhury, J. Sakamoto, *Joule* **2019**, 3, 2165.
- [136] J. Kasemchainan, S. Zekoll, D. Spencer Jolly, Z. Ning, G. O. Hartley, J. Marrow, P. G. Bruce, *Nat. Mater.* **2019**, 18, 1105.
- [137] Q. Tu, L. Barroso-Luque, T. Shi, G. Ceder, *Cell Rep. Phys. Sci.* **2020**, 1, 100106.
- [138] E. Kazyak, M. J. Wang, K. Lee, S. Yadavalli, A. J. Sanchez, M. D. Thouless, J. Sakamoto, N. P. Dasgupta, *Matter* **2022**, 5, 3912.
- [139] M. Dixit, C. Beamer, R. Amin, J. Shipley, R. Eklund, N. Muralidharan, L. Lindqvist, A. Fritz, R. Essehli, M. Balasubramanian, I. Belharouak, *ACS Energy Lett.* **2022**, 7, 3936.
- [140] H.-F. Huang, Y.-N. Gui, F. Sun, Z.-J. Liu, H.-L. Ning, C. Wu, L.-B. Chen, *Rare Met.* **2021**, 40, 3494.
- [141] P. Barai, K. Higa, V. Srinivasan, *Phys. Chem. Chem. Phys.* **2017**, 19, 20493.
- [142] X. Zhang, Q. J. Wang, K. L. Harrison, K. Jungjohann, B. L. Boyce, S. A. Roberts, P. M. Attia, S. J. Harris, *J. Electrochem. Soc.* **2019**, 166, A3639.
- [143] S. Zhang, F. Sun, X. Du, X. Zhang, L. Huang, J. Ma, S. Dong, A. Hilger, I. Manke, L. Li, B. Xie, J. Li, Z. Hu, A. C. Komarek, H.-J. Lin, C.-Y. Kuo, C.-T. Chen, P. Han, G. Xu, Z. Cui, G. Cui, *Energy Environ. Sci.* **2023**, 16, 2591.
- [144] J. Pan, Y. Zhang, F. Sun, M. Osenberg, A. Hilger, I. Manke, R. Cao, S. X. Dou, H. J. Fan, *Angew. Chem., Int. Ed.* **2023**, 62, e202219000.
- [145] Y. Qi, C. Ban, S. J. Harris, *Joule* **2020**, 4, 2599.
- [146] E. A. Carmona, M. J. Wang, Y. Song, J. Sakamoto, P. Albertus, *Adv. Energy Mater.* **2021**, 11, 2101355.
- [147] C. D. Fincher, C. E. Athanasiou, C. Gilgenbach, M. Wang, B. W. Sheldon, W. C. Carter, Y.-M. Chiang, *Joule* **2022**, 6, 2794.
- [148] F. Zhang, Y. Guo, L. Zhang, P. Jia, X. Liu, P. Qiu, H. Zhang, J. Huang, *eTransportation* **2023**, 15, 100220.
- [149] Q.-Y. Yang, Z. Yu, Y. Li, W. Zhang, H.-W. Yuan, H.-J. Li, W. Ma, S.-M. Zhu, S. Li, *Rare Met.* **2022**, 41, 2800.
- [150] Z.-C. Li, T.-Y. Li, Y.-R. Deng, W.-H. Tang, X.-D. Wang, J.-L. Yang, Q. Liu, L. Zhang, Q. Wang, R.-P. Liu, *Rare Met.* **2022**, 41, 2834.
- [151] M. K. Aslam, Y. Niu, T. Hussain, H. Tabassum, W. Tang, M. Xu, R. Ahuja, *Nano Energy* **2021**, 86, 106142.
- [152] M. Motoyama, M. Hirota, T. Yamamoto, Y. Iriyama, *ACS Appl. Mater. Interfaces* **2020**, 12, 38045.
- [153] D. Spencer Jolly, Z. Ning, G. O. Hartley, B. Liu, D. L. R. Melvin, P. Adamson, J. Marrow, P. G. Bruce, *ACS Appl. Mater. Interfaces* **2021**, 13, 22708.
- [154] P. Hundekar, S. Basu, J. Pan, S. F. Bartolucci, S. Narayanan, Z. Yang, N. Koratkar, *Energy Storage Mater.* **2019**, 20, 291.
- [155] P. Hundekar, R. Jain, A. S. Lakhnot, N. Koratkar, *J. Appl. Phys.* **2020**, 128, 010903.
- [156] C. Wu, H. Huang, W. Lu, Z. Wei, X. Ni, F. Sun, P. Qing, Z. Liu, J. Ma, W. Wei, L. Chen, C. Yan, L. Mai, *Adv. Sci.* **2020**, 7, 1902643.
- [157] K. Dong, Y. Xu, J. Tan, M. Osenberg, F. Sun, Z. Kochovski, D. T. Pham, S. Mei, A. Hilger, E. Ryan, Y. Lu, J. Banhart, I. Manke, *ACS Energy Lett.* **2021**, 6, 1719.
- [158] A. Parejiya, R. Amin, M. B. Dixit, R. Essehli, C. J. Jafta, D. L. Wood III, I. Belharouak, *ACS Energy Lett.* **2021**, 6, 3669.
- [159] P. Hundekar, S. Basu, X. Fan, L. Li, A. Yoshimura, T. Gupta, V. Sarbada, A. Lakhnot, R. Jain, S. Narayanan, Y. Shi, C. Wang, N. Koratkar, *Proc. Natl. Acad. Sci.* **2020**, 117, 5588.
- [160] B. S. Vishnugopi, F. Hao, A. Verma, P. P. Mukherjee, *ACS Appl. Mater. Interfaces* **2020**, 12, 23931.
- [161] Y. Zhu, J. Xie, A. Pei, B. Liu, Y. Wu, D. Lin, J. Li, H. Wang, H. Chen, J. Xu, A. Yang, C.-L. Wu, H. Wang, W. Chen, Y. Cui, *Nat. Commun.* **2019**, 10, 2067.
- [162] Z. Zhou, G. Li, J. Zhang, Y. Zhao, *Adv. Funct. Mater.* **2021**, 31, 2107136.
- [163] Z. Li, R. Yu, S. Weng, Q. Zhang, X. Wang, X. Guo, *Nat. Commun.* **2023**, 14, 482.
- [164] Y. Huang, R. Li, S. Weng, H. Zhang, C. Zhu, D. Lu, C. Sun, X. Huang, T. Deng, L. Fan, L. Chen, X. Wang, X. Fan, *Energy Environ. Sci.* **2022**, 15, 4349.
- [165] Y. Guo, R. Wang, C. Cui, R. Xiong, Y. Wei, T. Zhai, H. Li, *Nano Lett.* **2020**, 20, 7680.
- [166] W. Li, S. Zhang, W. Zheng, J. Ma, L. Li, Y. Zheng, D. Sun, Z. Wen, Z. Liu, Y. Wang, G. Zhang, G. Cui, *Adv. Funct. Mater.* **2023**, 33, 2300791.
- [167] C. Wang, M. Liu, M. Thijs, F. G. B. Ooms, S. Ganapathy, M. Wagemaker, *Nat. Commun.* **2021**, 12, 6536.
- [168] T. Gu, L. Chen, Y. Huang, J. Ma, P. Shi, J. Biao, M. Liu, W. Lv, Y. He, *Energy Environ. Mater.* **2022**, <https://doi.org/10.1002/eeem2.12531>.
- [169] P. Shi, J. Ma, M. Liu, S. Guo, Y. Huang, S. Wang, L. Zhang, L. Chen, K. Yang, X. Liu, Y. Li, X. An, D. Zhang, X. Cheng, Q. Li, W. Lv, G. Zhong, Y.-B. He, F. Kang, *Nat. Nanotechnol.* **2023**, 18, 602.
- [170] J. Tao, Y. Chen, A. Bhardwaj, L. Wen, J. Li, O. V. Kolosov, Y. Lin, Z. Hong, Z. Huang, S. Mathur, *Proc. Natl. Acad. Sci.* **2022**, 119, e2211059119.
- [171] G. García, S. Dieckhöfer, W. Schuhmann, E. Ventosa, *J. Mater. Chem. A* **2018**, 6, 4746.
- [172] Y. Chen, X. Dou, K. Wang, Y. Han, *Adv. Energy Mater.* **2019**, 9, 1900019.
- [173] V. Reisecker, F. Flatscher, L. Porz, C. Fincher, J. Todt, I. Hanghofer, V. Hennige, M. Linares-Moreau, P. Falcaro, S. Ganschow, S. Wenner, Y. M. Chiang, J. Keckes, J. Fleig, D. Rettenwander, *Nat. Commun.* **2023**, 14, 2432.
- [174] K. Shen, Z. Wang, X. Bi, Y. Ying, D. Zhang, C. Jin, G. Hou, H. Cao, L. Wu, G. Zheng, Y. Tang, X. Tao, J. Lu, *Adv. Energy Mater.* **2019**, 9, 1900260.

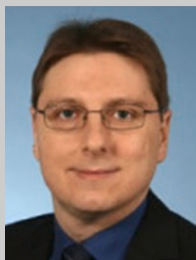
- [175] A. Wang, Q. Deng, L. Deng, X. Guan, J. Luo, *Adv. Funct. Mater.* **2019**, 29, 1902630.
- [176] Y. Huang, X. Wu, L. Nie, S. Chen, Z. Sun, Y. He, W. Liu, *Solid State Ion.* **2020**, 345, 115171.
- [177] Y. Chen, X. Dou, K. Wang, Y. Han, *Green Energy Environ.* **2022**, 7, 965.
- [178] C. M. Costa, K. J. Merazzo, R. Gonçalves, C. Amos, S. Lanceros-Méndez, *iScience* **2021**, 24, 102691.
- [179] K. Shen, X. Xu, Y. Tang, *Nano Energy* **2022**, 92, 106703.
- [180] L. Han, J. Wang, X. Mu, T. Wu, C. Liao, N. Wu, W. Xing, L. Song, Y. Kan, Y. Hu, *J. Colloid Interface Sci.* **2021**, 585, 596.
- [181] X.-L. Gao, X.-H. Liu, W.-L. Xie, L.-S. Zhang, S.-C. Yang, *Rare Met.* **2021**, 40, 3038.
- [182] V. Raj, V. Venturi, V. R. Kankanallu, B. Kuri, V. Viswanathan, N. P. B. Aetukuri, *Nat. Mater.* **2022**, 21, 1050.
- [183] S. Zhang, G. Yang, Z. Liu, S. Weng, X. Li, X. Wang, Y. Gao, Z. Wang, L. Chen, *ACS Energy Lett.* **2021**, 6, 4118.
- [184] A. C. Thenuwara, E. L. Thompson, T. F. Malkowski, K. D. Parrotte, K. E. Lostracco, S. Narayan, R. T. Rooney, L. A. Seeley, M. R. Borges, B. D. Conway, Z. Song, M. E. Badding, K. G. Gallagher, *ACS Energy Lett.* **2023**, 10, 4016.



**Jianhua Yao** received her M.E. degree from Ocean University of China in 2020. Afterward, she has been working in the production of the state-of-the-art lithium-ion batteries for 8 years before joining Qingdao Institute of Bioenergy and Bioprocess Technology (QIBEBT), Chinese Academy of Sciences (CAS) in 2010. She is now a senior engineer for investigating a variety of advanced energy storage batteries in QIBEBT, CAS.



**Fu Sun** received his Ph.D. degree from Technical University of Berlin in 2017. Afterward, he has been working as a postdoctoral fellow at Helmholtz Zentrum Berlin für Materialien und Energie for the following 2 years. He is now a senior research fellow at QIBEBT, CAS. His research is focused on investigating working mechanisms and/or failure modes of various types of rechargeable batteries using mostly nondestructive synchrotron X-ray imaging techniques.



**Ingo Manke** is head of the “Imaging Group” at the Helmholtz-Zentrum Berlin für Materialien und Energie and reader at the Technical University Berlin (TUB). He studied physics at the Freie Universität Berlin and received a Ph.D. in solid state physics from TUB in 2002. His research area focuses on the development of imaging techniques based on X-rays, neutrons, and electrons and on their application on energy-related materials.



**Guanglei Cui** received his Ph.D. degree from the Institute of Chemistry, CAS in 2005. He then did postdoctoral research at Max-Planck-Institute for Polymer Research and Max-Planck-Institute for Solid State Research before joining QIBEBT, CAS in 2009. He is currently a professor and the leader of Solid Energy System Technology Center and the director of Division of Advanced Energy Storage Technology. His research topics include sustainable and highly efficient energy-storage materials, all-solid-state batteries, and novel energy devices.